Dynamical tuning of phonon transport for information and energy control

by

Sophia Robin Sklan

Bachelor of Science, Cornell University (2010)

Submitted to the Department of Physics
in partial fulfillment of the requirements for the degree of

Doctor of Philosophy

at the

MASSACHUSETTS INSTITUTE OF TECHNOLOGY

February 2016

Author ... Signature redacted .....
Department of Physics
December 7, 2015

Certified by..... Signature redacted .....
Jeffrey C. Grossman
Department of Materials Science and Engineering
Thesis Supervisor

Certified by..... Signature redacted .....
Liang Fu
Department of Physics
Thesis Supervisor

Accepted by..... Signature redacted .....
Nergis Mavalvala
Associate Department Head for Education

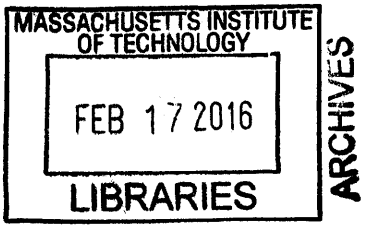

Dynamical tuning of phonon transport for information and energy control

by

Sophia Robin Sklan

Submitted to the Department of Physics

on January 8, 2016 in Partial Fulfillment of the

Requirements for the Degree of Doctor of Philosophy in

Physics

Abstract

Controlled transport of energy and information is of paramount importance. It remains challenging, however, partially from the difficulty in controlling their physical carriers. Steering electrons and photons is now routine, yet atomic vibrations (quantized as phonons) are hard to control. This is partly due to the centrality of phonons in the disordered transport of energy as heat, but even in ordered sound waves problems persist. Phonons can readily couple to each other or to other degrees of freedom, degrading their energy or information content. Reversing these couplings, thereby regulating atomic motion, only recently became plausible. This increased control would reduce parasitic losses and turn phonons into information carriers. Dynamical effects are a crucial and under-examined aspect of this control as static devices are insufficient for changing external conditions. Dynamical control adds flexibility and versatility to phononic systems. Essentially, dynamical control requires tunable materials, materials whose physical properties depend on an external signal. Dynamical tuning is sensitive to the relative frequencies of the tuning signal and the controlled phonons. We develop an intuitive framework of the temporal modulation regimes.

In low frequency tuning, phonons can adapt adiabatically to the material's changes. A variety of signals can be temporally and spatially modulated to tune phonon transport in this regime. We apply this adiabatic perspective to analyze dynamical effects in thermal cloaks. Tuning signals near the frequency of some phonon mode can produce resonant couplings. This hybridization can produce large changes in phonon properties. We apply this hybridization to develop a rigorously nonreciprocal phononic computer using magneto-acoustic materials that can outperform conventional computers in some tasks. At high frequencies, phonons can only respond perturbatively to the tuning signal's changes. This regime is generally limited to optical control but it opens up new avenues for control. Employing an alternative approach to optical coupling, we develop a model of inverse acousto-optics (tuning the speed of sound with optical intensity) and dynamical phonon localization.

Thesis Supervisor: Jeffrey C. Grossman

Title: Professor of Materials Science and Engineering

Chapter 1

Introduction

Although they are immaterial (i.e. they do not possess mass), energy and information are integral to every physical process. The controlled transport and storage of energy has been a paramount concern of the last two hundred years, while the processing and memory of information rose to similar prominence in the last century. These efforts, broadly speaking, face two challenges: change and degradation. Change because most devices exist in a world of changing conditions, and degradation because not all energy or information is of equivalent quality.

To adapt to changing conditions requires devices that can, in some sense, measure external conditions and change their internal state accordingly. This adaptation is often thought of in terms of feedback, active systems, smart materials, and control theory. However, these forms of controlled adaptation are the more complex manifestations of a much more basic phenomenon. A material will often change under changing external conditions. It can be as simple and mundane as mercury rising in a thermometer along with the temperature, the buckling of a beam under pressure, or the alignment of spins in a magnetic field. When a material property is responsive to external conditions, it is tunable. This tunability can provide a measure of stability against changing conditions, a la Le Châtelier's principle and homeostasis. It can also provide information processing, assuming that the condition it is responding to carries information (e.g. a tree's shadow can indicate time). Tunability even allows us an avenue for controlling a material's properties, and therefore the response

of a device. After all, changing conditions do not only come from effects outside of our control. It is possible to actively tune a material's response or use the information from a transmitted signal to adaptively tune a material through feedback. Thus, developing tools to tune material parameters is an important step to controlling the transport of energy and information.

Not all information or energy is of the same quality, however. For both energy and information, the quality is measured by entropy – specifically the entropy contained by the system transporting the signal. For example, the energy transported by laser light is lower entropy than that of an incandescent light bulb. As the system acquires configurational variety [1], the entropy increases. Such a process happens naturally, as the second law of thermodynamics implies that entropy cannot be reduced except at the cost of an even greater increase in entropy elsewhere. The highest entropy form of energy is heat, which is noisy (i.e. low information) and disordered (in a physical but not necessarily anthropic sense). It can take many forms, but is typically transported by light (quantized as photons), electricity (quantized as electrons), and sound (quantized as phonons). A variety of tools and techniques have been developed over the years for controlling the movement of photons and electrons, but controlling sound remains a challenge. This is particularly true in solids, where the phonons take the form of a vibrating atomic lattice. The development of controlled phonon transport in solids, called phononics, is still in its early stages [1, 2]. As it advances, though, it will allow greater control of energy transport, particularly at the higher entropy range where phonons tend to dominate. It even raises the possibility of creating lower entropy phonon signals (i.e. well-defined sound waves), much like the introduction of the laser revolutionized the utilization of light [3, 4]. To do this, though, it is important to expand the tools available for controlling phonons. Tunable phononic devices and materials, in particular, are essential for this task. Understanding these systems within a unified framework and designing their applications will be the focus of this work.

[1] Configurational variety is often manifested in physical systems as disorder, however the anthropic assessment of order is distinct from the physical order measured by Boltzmann entropy. Boltzmann entropy implies that aligned planes of smetic or chiral liquid crystals, chemical waves in the Belousov-Zhabotinsky reaction, and other forms of pattern formation are more disordered than the intuitively disordered states are. Similarly, a random message is more disordered in the sense of Chaitin-Kolmogorov complexity but the detailed account of the random process that created it is information, just not information that is anthropically meaningful. A network can have high Shannon entropy an transmit messages with optimal encoding but the message may seem like noise to the recipient. Intuitive assessments of disorder and entropy do not necessarily coincide with the manifestations of entropy in nature.

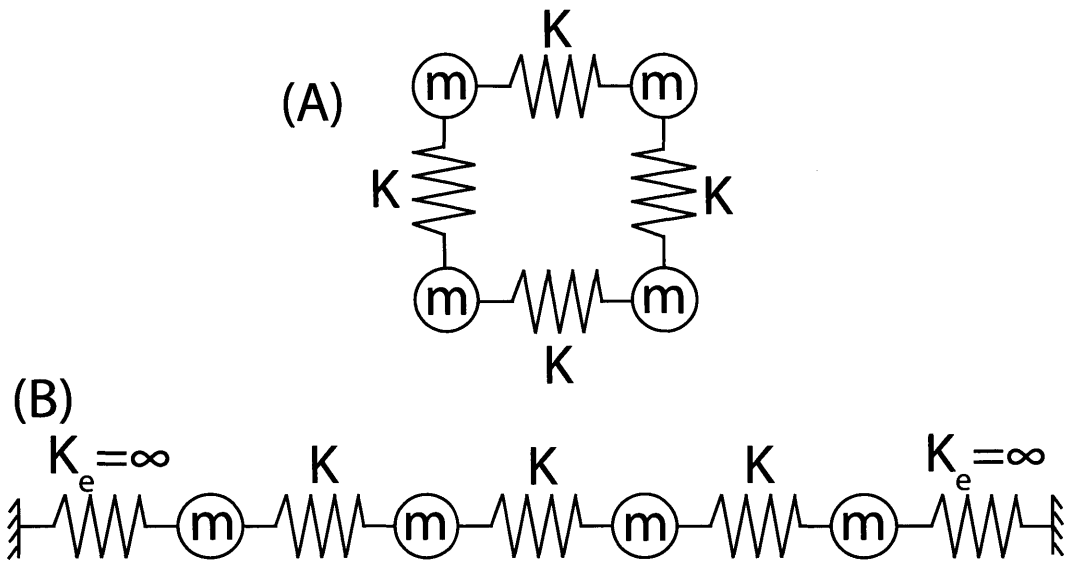

Figure 1-1: Classical model of a mechanical vibration normal modes problem. The circles denote mass of value m joined by springs (denoted by the linked diagonal lines) of value K. In (a) the masses are joined in periodic boundary conditions, which are frequently assumed in the calculation of phonon modes. In (b) the masses are held in place through clamped boundary conditions (i.e. attached to a wall, denoted by dashed lines, by perfectly stiff springs, denoted by $K_e = \infty$), which are often more relevant for classical standing waves.

To begin, though, it is helpful to start with some basic aspects of phonons as they will guide our later considerations. Classically, the governing equation for a one-dimensional chain of masses linked by harmonic oscillators (see Fig. 1-1) is

$$m\ddot{u}_i = -K(u_i - u_{i+1}) - K(u_i - u_{i-1}) \tag{1.1}$$

where m is the mass, u is the atomic displacement from equilibrium, K is the spring constant, and i is the site index. This equation can be solved by Fourier transform to give solutions of the form

$$U_k = A_k e^{ika} \tag{1.2}$$

where

$$\omega_k = \sqrt{\frac{2K}{m}} \left| \sin \frac{ka}{2} \right| \tag{1.3}$$

is the eigenfrequency, a is the separation between equilibrium sites, and k is the wave vector. Since the chain is made up of discrete masses, the wave vector is itself limited to discrete

wavelengths and takes the form

$$k = \frac{2\pi p}{Na} \tag{1.4}$$

where N is the number of sites in the chain and p is an integer between $-N/2$ and $N/2$. In the limit of $N \to \infty$, $a \to 0$ the discrete wavelengths become continuous and so the allowed frequencies become a continuous function (i.e. an energy band). In this case, the equation of motion (eq. 1.1) becomes redefined as

$$\rho \frac{\partial^2}{\partial t^2} \epsilon_{ij} = c_{ijkl} \epsilon^{kl} \tag{1.5}$$

where ρ is the density (transformed mass), $\epsilon_{ij} = (\partial u_i/\partial x_j + \partial u_j/\partial x_i)/2$ is the strain (transformed displacement), c_{ijkl} is the stiffness (transformed spring constant), and Einstein summation conventions have been used (repeated indices are summed over). Additionally, the behavior of this chain is not greatly changed in moving from classical to quantum mechanics, except that in the quantum limit the amplitude of the displacements becomes quantized to discrete values and so the energy of the system is $E_n k = \hbar\omega_k(n_k + 1/2)$. Allowing the displacement to occur along an arbitrary direction means that there are now multiple eigenfrequencies for each wave vector. These eigenmodes can be distinguished as longitudinal modes (whose displacement is along the direction of propagation, i.e. $\hat{n} \| \hat{k}$ where $\hat{n}$ is the polarization vector) and transverse modes (displacement orthogonal to propagation, $\hat{n} \perp \hat{k}$). In three dimensions there will be two transverse modes and one longitudinal mode for each wave vector. These eigenmodes constitute additional energy bands in the phonon spectrum. Allowing the mass or spring constants to vary with some periodicity will also introduce additional bands. Unlike the previously discussed longitudinal and transverse modes, whose frequencies fall to 0 as $k \to 0$, these new modes retain non-zero frequency in the limit of infinite wavelength. This means that these modes can interact with light, and so the previous set of bands are called acoustic bands while these new bands are called optical bands. In general, for a lattice of N atoms there will be three acoustic bands and $3(N-1)$ optical bands. These results are summarized in Fig. 1-2, which illustrates the phonon band structure.

Because phonons are composed of arrays of coupled harmonic oscillators, we can therefore get some intuition towards how phonons will react to a changing environment by studying the

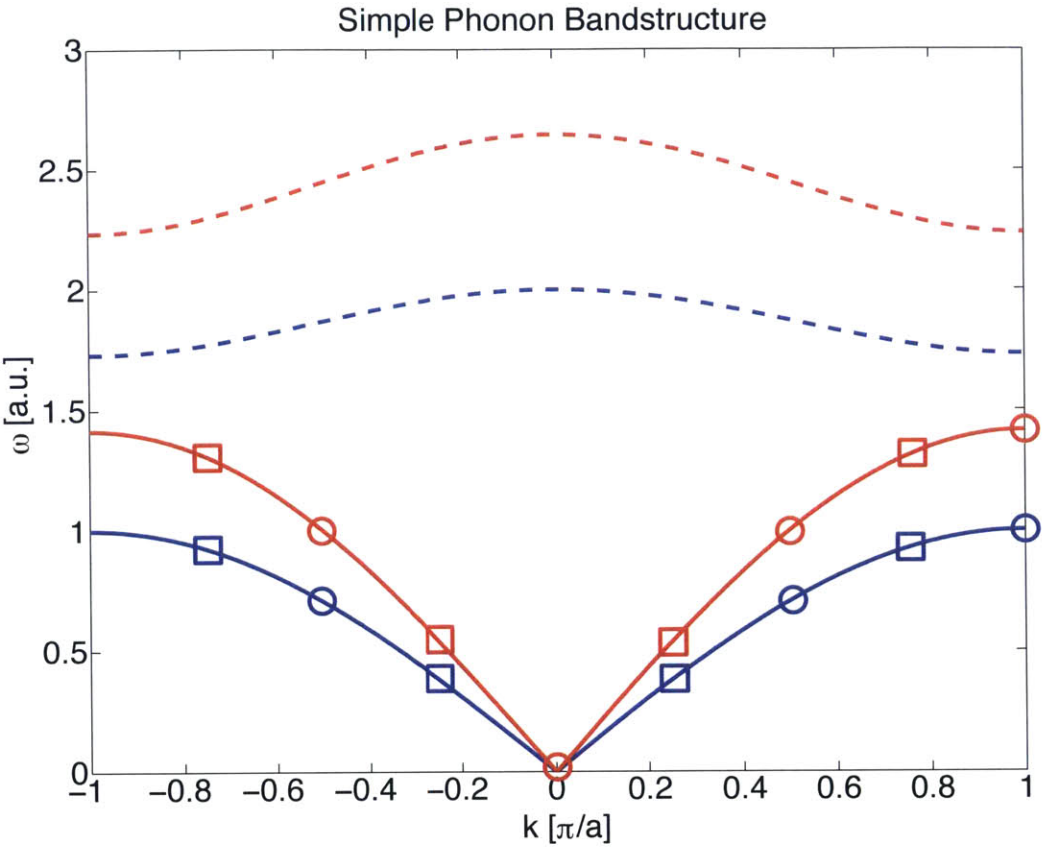

Figure 1-2: An illustration of a typical phonon band structure. The red solid line is the longitudinal acoustic mode, the blue solid line is the pair of degenerate transverse acoustic modes, the red dashed line is the longitudinal optical mode, and the blue dashed line is the degenerate transverse optical mode. The modes of Fig. 1-1 would be at four discrete points along the acoustic branches. For Fig. 1-1a (i.e. the periodic boundary conditions employed in developing this phonon band structure) these discrete points would be equally spaced along the interval $ka/\pi \in [-1, 1]$ and include $k = 0$ (Note that $k = \pi/a$ is equivalent to $k = -\pi/a$). We denote these points with open circles. On the other hand, for Fig. 1-1b these points would be equally spaced along the same interval and not include the origin. We denote these points with squares.

behavior of a simple harmonic oscillator under changing conditions. Consider the equation of motion for a harmonically forced, undamped harmonic oscillator

$$m\ddot{u} + m\omega_0^2 u = F\sin(\omega_d t) \tag{1.6}$$

where $\omega_0^2 = K/m$. The response will be

$$u = \frac{F}{m}\frac{1}{\omega_0^2 - \omega_d^2}\sin(\omega_d t). \tag{1.7}$$

Note that, for a driving frequency ω_d below the natural resonance frequency ω_0, the response function will be in phase with the driving force. On the other hand, when the driving frequency is greater than the resonance frequency, the response function changes sign and is π radians out of phase. Driving at the resonance frequency, the response function's phase is not well defined as it blows up to $\pm\infty$. These three frequency regimes for the driving function suggest a general framework for considering the response of a phononic system to a changing environment [2]. If the changes occur at some time scale τ, we can divide up the response into three regimes depending upon the dimensionless variable $\omega\tau$. If $\omega\tau > 1$ then just as the harmonic oscillator is able to keep up with the driving, so a generic solid material will be able to respond effectively instantaneously. So far as the phonons are concerned, in this regime the tuned parameters are either constant or adiabatically varying. If $\omega\tau \approx 1$ then there is a resonance and strong coupling between the driving signal the response dynamics. The phonons will be particularly sensitive to perturbations at this frequency and the band structure may change dramatically. Finally, if $\omega\tau < 1$ then the harmonic oscillator is unable to keep up with the driving and the material will not be able to adapt smoothly. In this regime, the parameters become functions of time that can vary faster than the phonon frequency and so act as perturbations to the phonon Hamiltonian. These regimes, summarized in table 1.1 will guide the organization of this paper. Each chapter will consider some aspect of tuning phononic response in a regime of $\omega\tau$.

[2] In moving to this more general framework we drop the subscript 0, which referred to the specific harmonic oscillator modeled in eq. 1.6

Regime	SHO	Tuning
$\omega\tau > 1$	$\theta = 0$	Adiabatic
$\omega\tau \approx 1$	$u \to \pm\infty$	Resonant
$\omega\tau < 1$	$\theta = \pi$	Perturbation

Table 1.1: Different regimes of the response function, organized by the product of the system's natural frequency (ω) and the time-scale of the driving signal (τ). Responses are given for the classical simple harmonic oscillator (SHO) and tuned material response. θ refers to the phase difference between the driving signal's oscillating amplitude and the phonon amplitude (u).

Chapter 2

Slow Tuning Limit

As explained in Ch. 1, when the tuning of material properties is significantly slower than the phonon frequency, the phonons will experience an effectively static medium. This means that the tuning of parameters will not noticeably perturb the phonon dynamics and hence that adiabatic tuning can be understood by considering a succession of static cases. We therefore begin this chapter with an overview of various techniques for adiabatically tuning phonon band structure, starting with a sampling of the static case. These techniques are versatile, spanning a broad range of tuning signals and with applications including noise isolation, thermal insulation, acoustic waveguide design, frequency filtering phonons, steerable acoustic antennae, and acoustic measurement of tuning signals. Following this, we will consider the problem of relating linear, anisotropic, inhomogeneous, symmetric transport parameters to actual transport dynamics. This will focus particularly on the use of the transformation media technique. Finally, we will use this technique to illustrate cases where tuning is unnecessary for adaptive materials and where a lack of tuning and adaption results in system failure. In particular, we will consider the performance of thermal cloaking devices, as their incoherent, diffusive phonon transport arises from the frequent scattering of extremely high frequency phonons (e.g. THz).

2.1 Quasistatic Phonon Tuning

2.1.1 Static Tuning

The case of stationary modifications to a material structure to induce some specific change in the acoustic properties of a material was first investigated by Rytov in the 1950s [5, 6]. There, he analyzed the behavior of phonons in "artificial thin laminates" and found the folding of band structures now commonly associated with superlattices [7]. Essentially, as the periodicity of the system is extended, the maximum reduced. In reciprocal space, this is equivalent to zone folding. This effect was experimentally confirmed in Colvard et al. [8]. Contemporary interest in the problem was sparked by improvements in nanofabrication, allowing nanostructured materials that greatly modify the phonon band structure. Balandin and Wang, for example, studied the effects of phonon confinement on the density of states and group velocity [9]. Zou and Balandin then demonstrated that these effects change the phonon relaxation dynamics and therefore the thermal conductivity [10]. Pokatilov et al. [11] demonstrate that in sufficiently thin heterostructures, the hybridization of phonons across the interface can lose out to the localization of different phonon branches to different heterostructure layers. For example, in Fig. 2-1 there is a GaN layer sandwiched between two AlN layers. At different wave vectors, individual shear modes become localized to either the central or edge regions, giving them group velocities characteristic of the respective bulk material. Other polarizations exhibit similar effects [13]. Localization is studied for a variety of structures in Balandin et al. [13], which reviews work on this problem and on engineering electron-phonon couplings. On the thermal (i.e. disordered phonons) side, transport engineering has been reviewed by Norris et al. [14]. They pay particular attention to the role of interfacial scattering and how it can be used to engineer thermal boundary resistance. A particularly popular tuning technique not mentioned there is the use of phononic crystals (artificial lattices whose properties arise from the arrangement of the elements not their properties) which can be rotated [15, 16, 17] to change their effective spring constants and therefore band structure. Goffaux and Vigneron [15] developed this technique for a square lattice of rectangular rods arranged to be face to face or corner to corner. They find that an acoustic band gap (frequency range in which phonons cannot propagate) forms as a function

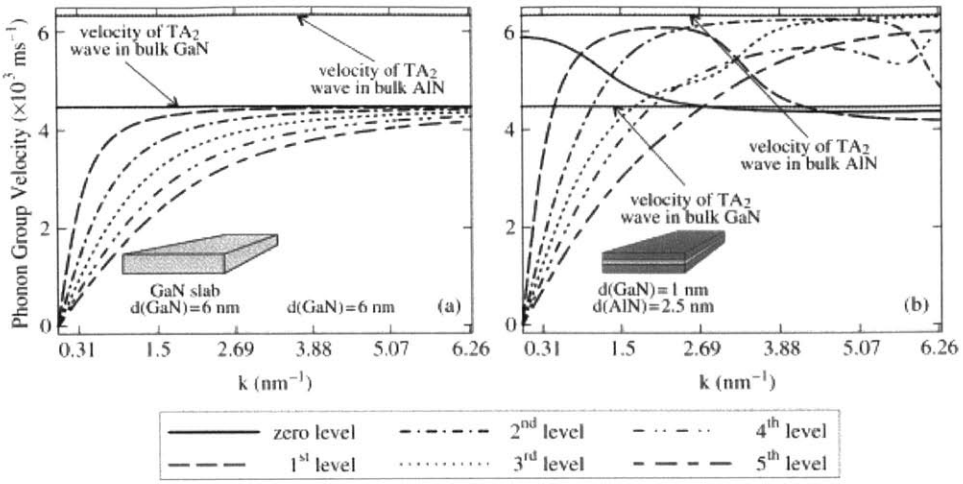

Figure 2-1: Phonon localization. Phonon group velocities of shear polarized phonon modes versus wave vector. (a) A 6 nm width semiconductor GaN slab, for reference. (b) A AlN/GaN/AlN three-layered heterostructure with dimensions 2.5/1/2.5 nm. When the group velocity of a given mode approaches the asymptotes of the bulk material, phonons become localized. Reprinted from E. P. Pokatilov et al., *Superlatt. Microstruct.* **33**, 155 (2003). Copyright 2003, Elsevier [12].

of the rods' orientation angle. Kuang et al. [16] extend this technique to a wider array of lattice symmetries and constituent elements. Lin and Huang [17] further extend it to the case of anisotropic constituents. Hou et al. [18] and Yao et al. [19] consider a fixed phononic crystal with mobile inclusions. Another approach to engineering thermal transport by tuning phonon band structure, which shall come back in later chapters (notably Ch. 3.2), was reviewed by Roberts and Walker [20] and by Li et al. [1]. There, they are concerned with the amplification of thermal rectification (the preferential flow of heat along one direction rather than the reverse), which can be tuned by the preferential placement and structuring of defects [1, 20].

2.1.2 Mechanical Tuning

Moving from static tuning to nonstationary effects, the first technique that was considered was the use of external forces. This can take the form of stress or strain as the controlled variable, the effect is generally similar. Hsieh et al. [21], for example, use pressure to increase the bond strength at interfaces, and thereby tune the elasticity and thermal conductivity. Bertoldi and Boyce [22] introduced this technique to phononic crystals, using an array of

holes in an elastic matrix. Applying strain changed the arrangement and shape of the holes, which gave a functional means of introducing directional and complete band gaps through applied strains of various strength and orientation. The theory in this case was somewhat complicated, as the transformations relied upon mechanical instabilities that greatly change the equation of motion. The theory of such transformations was sketched out in Bertoldi and Boyce [23]. Rather than applying stress as a boundary condition, Jang et al. [24] replace the air in the pores with a solvent. Various extensions of this technique have been developed to cover different instability mechanisms (uniaxial compression [25], elongation [26], buckling [27], folding [28], and wrinkling [29]), three-dimensional phononic crystals [30, 31], nonlinear materials (in addition to the geometric nonlinearity than induces the mechanical instability) [32], and more complex patterns [33]. A typical example of this effect is shown in Fig. 2-2. In many of these cases, the mechanical instability implies that the stable configuration suddenly switches (i.e. the stability bifurcates), and so varying the applied stress has a highly nonlinear effect on the phononic band structure. On the other hand, systems lacking these mechanical instabilities have continuous response functions to applied stresses. A particularly well-studied case is the class of materials known as granular phononic crystals, which are constructed of beads placed in Hertzian contact (i.e. their forces go as $(\Delta u)^{3/2}$ where u is displacement from equilibrium). This nonlinearity can be exploited by the application of uniform stress fields that compresses the beads, changing the effective spring constant. Various configurations of granular phononic crystal lattices have been shown to have tunable band gaps through this effect, particularly one-dimensional chains of various periodicity [34, 35, 36] (similar effects have been observed for other related systems, such as Refs. [37, 38]). This analysis has also gone beyond the simple harmonic picture, such as the tuning of solitons (highly nonlinear, particle-like wave packets). Daraio et al. [39] find that the soliton envelope and speed are significantly modified with the modulation of the granular phononic crystal's compression. Spadoni and Daraio [40] as well as Donahue et al. [41] experimentally demonstrated that these lattices constitute an acoustic lens of tunable focal length. Spadoni and Daraio [40] focused on soliton packets in arrays of granular chains, while Donahue et al. [41] focused on soliton packets in two dimensional granular phononic crystals. Boechler et al. [42] also demonstrate that granular chains can serve as an acoustic switch.

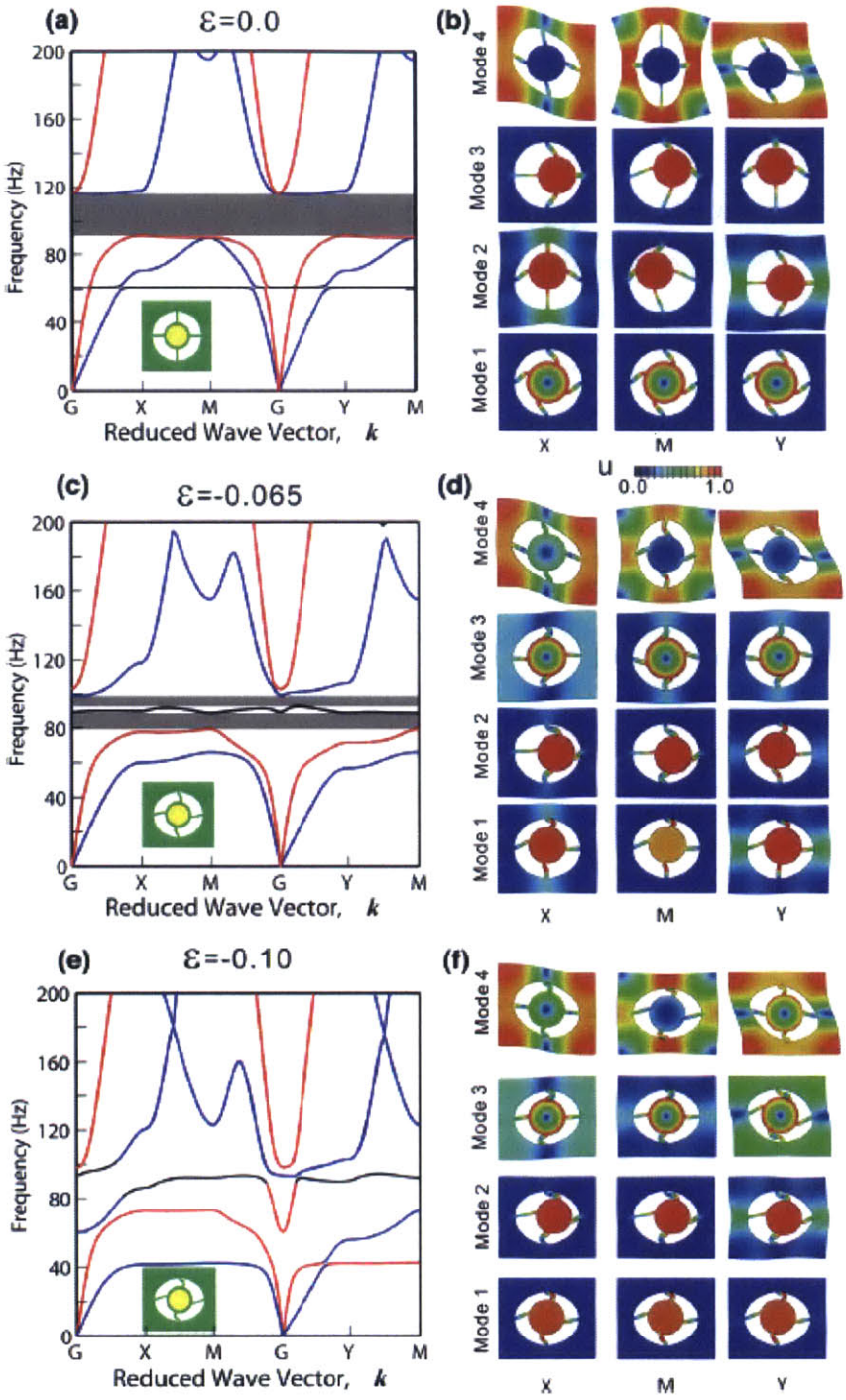

Figure 2-2: Effect of deformation on a mechanically unstable structure. (a), (c), and (e) are the dispersion relations for unstrained, $\epsilon = -0.065$, and $\epsilon = -0.10$, respectively. Shear modes are blue, longitudinal are red, rotational are black, and band gaps are grey. Deformations induced by the lowest four modes at high symmetry points in the Brillouin zone are shown in (b), (d), and (f) for $\epsilon = 0$, $\epsilon = -0.065$, and $\epsilon = -0.10$, respectively. Color indicates magnitude of displacement. Reprinted figure with permission from P. Wang, F. Casadei, S. Shan, J. C. Weaver, and K. Bertoldi, *Phys. Rev. Lett.* **113**, 014301 (2014). Copyright 2014 by the American Physical Society [27].

2.1.3 Thermal Tuning

Thermal effects on phonon band structure are generally weak, but there have been some efforts to find systems where temperature can strongly tune phononic properties. Huang and Wu [43] studied the temperature dependence of density, elasticity, and thermal expansion of a phononic crystal array in air. The combination of solid and gas allows for a greater change of material parameters (notably thermal expansion) than would occur for a purely solid state device. They similarly show that this effect can tune the size and location of the band gaps, although they found that some gaps widened and others narrowed as a function of temperature. Using a similar system, Wu et al. [44] studied the effects of changing air density and speed of sound on diffraction. To amplify the effects of temperature, other researchers have focused on the role of phase transitions. Jim et al. [45] and Xu et al. [46] study the onset of a ferroelectric phase transition for $Ba_{0.7}Sr_{0.3}TiO_3$ for bulk and surface waves, respectively. They find a significant shift in the band gaps of the bulk modes and a shift in the location of the Lamb wave surface modes. Similar work for the shift in gaps between Lamb modes was done by Cheng et al. [47] for one-dimensional structures and Yao et al. [48] for two-dimensional structures. Yao et al. [48] and Bian et al. [49] present analytic descriptions of this effect. Sato et al. [50] extend this to liquid-solid phase transitions, while Zheng et al. [51] apply the liquid-solid transition to the tuning of thermal conductivity. Wang et al. [52] investigated the role of liquid-solid phase transitions at high temperatures as an avenue to thermal energy storage. For solid-solid phase transitions, the most popular material is VO_2, which undergoes a transition between tetragonal and monoclinic structures that can be induced by a wide variety of forces (thermal, mechanical, electrical, optical) [53, 54, 55, 56, 57, 58]. Sepúlveda et al. [59], for example, studied the shift of Young's modulus near the transition temperature. Chen [60] studied the formation of band gaps and omnidirectional reflection in one-dimensional nitrinol and epoxy phononic crystals as nitrinol undergoes a structural phase transition from martensite to austenite. Walker et al. [61] considered a phononic crystal of metal rods in a polymer matrix. Using infrared radiation, they heated the polymer, causing it to undergo a structural phase transition that markedly changed its volume. Ruzzene and Baz [62, 63] added shape memory materials (whose structure undergoes controlled transformations as a function of temperature) to control the elastic constants of the phononic crystal and

subsequently tune their band structures.

2.1.4 Electrical Tuning

The tuning parameter does not have to be thermal or mechanical. While there are fairly general mechanisms to couple mechanical or thermal forces to acoustic and elastic properties, there also exist classes of materials with strong couplings to electric and magnetic fields. For electric field induced tuning of phonon band structure, multiple approaches exist. By far the most popular has been the use of piezoelectric inclusions in a phononic crystal, first studied by Hou et al. [64]. This effect is somewhat limited by the need to make a large fraction of the phononic crystal a piezoelectric, as demonstrated by Wang et al. [65], but Zou et al. [66] has demonstrated that it can still successfully open band gaps. Interestingly, since the properties of the system are sensitive to the magnitude and polarization of electric field, Rupp et al. [67] show that spatial variations of the electric field can be used to create patterned phononic crystals. In particular, they consider a system composed of elements where an electric field can be applied or withheld, and use the patterned application of the field to design filters, waveguides, actuators, and energy harvesting. Oh et al. [68] use this approach to construct a waveguide of arbitrary geometry. Celli and Gonella [69, 70], use a two-dimensional hexagonal lattice linked by piezoelectric elements. By asymmetrically tuning impedances applied to the linkages, they can reduce the overall symmetry of the lattice and thereby modulate the band structure. They exploit this induced anisotropy to control the angle of transmitted phonons at a given frequency, as illustrated in Fig. 2-3, and reduce the diffraction of phonons traversing the phononic crystal. Kusenko et al. [71] consider a one-dimensional piezoelectric phononic crystal, which they show can be described by effective elasticity and density functions. These effective parameters depend upon the strength of the electric field and are in general complex scalars. Hsu [72], Chen et al. [73], and Degraeve et al. [74] also consider piezoelectric systems of various geometries (two-dimensional phononic crystal, beam with piezoelectric patches, and uniform piezoelectric rods, respectively). However, rather than tuning the applied field, they change the impedance applied to each piezoelectric. As we will see in chapter 3.1.2, this approach can lead to resonant mode mixing, however in these works they are more concerned with the periodicity-induced Bragg scattering, which opens up phononic band gaps. An alternative approach to coupling

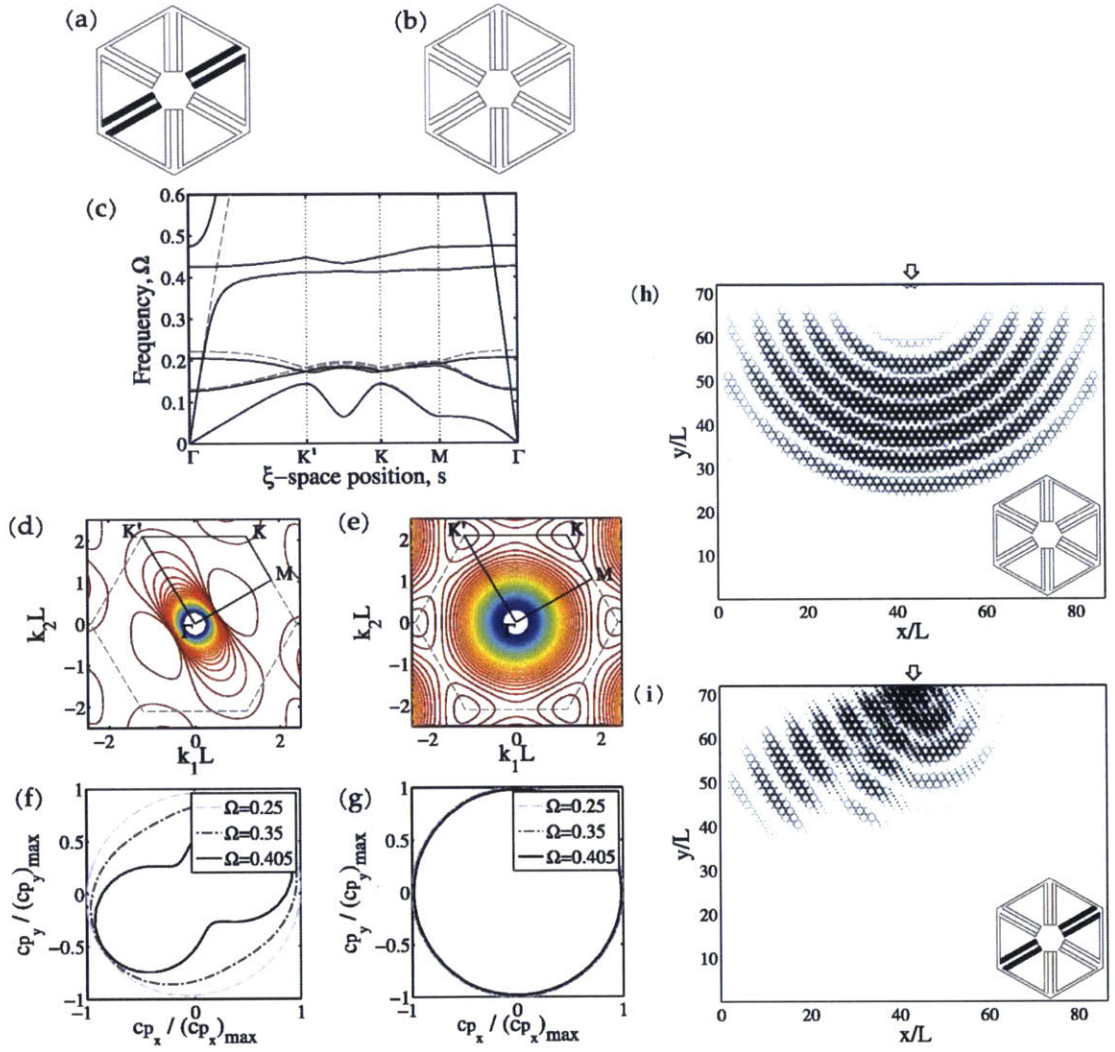

Figure 2-3: Piezoelectric tuning of phonon transport. Lattice is piezoelectric cells shown in (a) and (b). (a) Piezoelectric cell in the 30° configuration, where the dark lines indicate the component piezoelectrics that have been connected to a capacitor (i.e. shunted). (b) Open circuit configuration, no element of the piezoelectric cell is shunted. (c) Band diagram: continuous and dashed lines denote 30° and open cases. (d) and (e) Isofrequency contours of the fourth dispersion surface for the 30° and open cases. The deviation from circular contours is indicative of anisotropic transport, with the 30° case in (d) displaying markedly less angular symmetry than the open circuit case in (e). (f) and (g) Phase velocity of the fourth branch their respective configurations at various frequencies Ω. As frequency increases in (f) the contours move from circles (isotropic transport) to lobes (anisotropic transport). (h) and (i) potential energy fields of the open circuit (h) and 30° (g) configurations with a point source driving. Reprinted with permission from P. Celli and S. Gonella, *Appl. Phys. Lett.* **106**, 091905 (2015). Copyright 2015, AIP Publishing LLC [70].

with electric fields is to exploit the volume change induced by an applied field on a dielectric. This approach was taken in Yang and Chen [75] and Yang et al. [76] for spherical and cylindrical dielectric elements, while Wu et al. [77] used a single layer in a one-dimensional phononic crystal to create a band-pass filter. In a third approach, Ihlefeld et al. [78] use a ferroelastic material to change the distance between grain boundaries in a superlattice, thereby tuning the thermal conductivity. The final approach to electric field couplings is the use of electrorheological fluids, which change their viscosity under applied field. Since this effect only changes the shear modulus, only transverse phonons can be tuned through this method. Using thin layers of electrorheological fluid sandwiched between solid cells alone [79, 80] or as the basic unit of a phononic crystal lattice [81], the transmission, directivity, and band gaps can all be controlled by an applied electric field.

2.1.5 Magnetic Tuning

On the magnetic side, the use of magneto-acoustic materials (variously referred to as magnetoelastic and magnetostrictive materials) has been the most common technique. These are materials where an applied magnetic field can strongly couple to the (generally neutral or weakly charged) atomic lattice. This effect will be explained in detail in the following chapter (Ch. 3.3), as it can be used to generate phonon resonances. For much of the work in the field of phonon band structure engineering, however, these resonance effects have been neglected, instead focusing on the role of magnetostriciton (the modulation of volume by an applied magnetic field) or magnetoelasticity (the modulation of elasticity constants by an applied field). Robillard et al. [82] began this field by considering piezomagnetic effects (stresses induced by applied fields and magnetic fields induced by applied strains) in arrays of Terfenol-D rods (a giant magnetostrictive material). They found that the band gaps could be controlled by the strength of an applied field, including the closing of the band gap. Because of the nature of the coupling that they considered, they also found that only some of the phonon modes would couple to the magnetic field (in particular the shear modes, i.e. transverse phonons, could couple). Bou Matar et al. [83] extended this model to include the effect of spin reorientation under an applied field. This allows them to consider the effect of changing the field direction, in addition to changing the field strength. In addition to finding a tunable band structure, they derive expressions for effective material

parameters as a function of applied field. Unlike the previous work, they demonstrate that all the modes can be tuned by the applied field, including longitudinal phonons. Vasseur et al. [84] consider the same system, where they exploit the tunability to design switchable frequency filters, reconfigurable waveguides, and frequency multiplexers/demultiplexers (the combination/separation of signals at multiple frequencies), as shown in Fig. 2-4. This last effect works because the location of the band gap can undergo large shifts for small changes in field strength, so using local variations in field allows for the distinction of various modes. The downside to this approach is that it generally requires relatively large magnetic fields (at least 1 kOe). To get similar effective band structure control with weaker fields, Yang et al. [85] use the bending of magnetostrictive rods in air. Later, Yang et al. [86] use the bending of a beam with magnetostrictive plates to similar purpose. Schaeffer and Ruzzene [87] consider a magnetoelastic lattice composed of magnetic dipoles, with particular attention to how an applied magnetic field can induce structural instabilities that change the lattice to a new structure of different symmetry (much like the work on mechanical instabilities under applied stress). An alternative approach to magnetic tuning was developed by Baumgartl et al. [88] for a colloidal crystal with paramagnetic inclusions. For that matter, the use of magnetorheological fluids (the magnetic equivalent of electrorheological fluids) for controlling phonon band structure, was developed by Wu et al. [89]. Hasheminejad and Shabanimotlagh [90] use a magnetorheological elastomer for similar effect but with the advantage of behaving as a solid under ambient conditions. Xu et al. [91] extend this to a two-dimensional phononic crystal embedded within a magnetorheological elastomer matrix.

2.1.6 Mixed Tuning

Obviously, there is no *a priori* reason to prefer one tuning parameter over another. In fact, there has been further work on the use of multiple parameters to tune phonon band structure. Wang et al. [92] use a combination of electric and magnetic fields on a piezoelectric/piezomagnetic phononic crystal. Huang et al. [93] use a combination of strain and electric field on a piezoelectric phononic crystal, while Kambali et al. [94] use laser heating and electric fields to tune the eigenfrequency modes of a mechanical resonator. Jang et al. [95] use a combination of thermal transitions in a shape memory polymer and mechanical

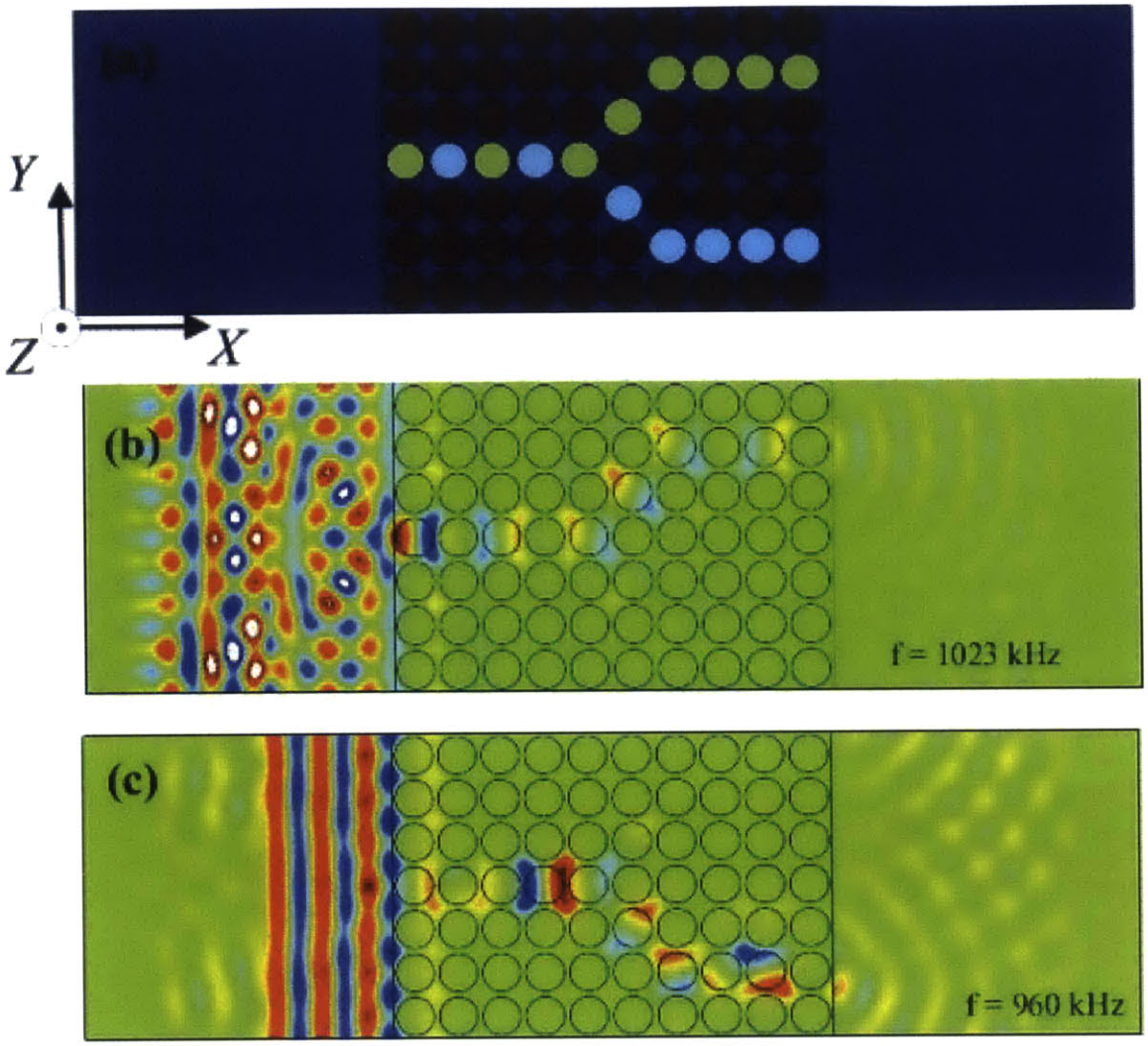

Figure 2-4: Demultiplexer (a) Waveguide schematic. Cylinders indicate Terfenol-D with different magnetic fields applied along the z direction: 1 kOe (blue rods), 2 kOe (green rods), and 20 kOe (red rods). Phonon displacement at (b) 1023 kHz, and (c) 960 kHz. From J. O. Vasseur, O. Bou Matar, J. F. Robillard, A.-C. Hladky-Hennion, and P. A. Deymier, "Band structures tunability of bulk 2D phononic crystals made of magneto-elastic materials." *AIP Advances* **1**, 041904 (2011). Available under a Creative Commons Attribution 4.0 license [84].

instability under applied strain. Zhang et al. [96] use a combination of thermal and magnetic effects in a Terfenol-D/epoxy phononic crystal, including the effects of temperature on both the total magnetization and the elastic modulus. The most widely studied combination is the use of simultaneous mechanical and magnetic control. Ding et al. [97] considered a one-dimensional phononic crystal with a new model of magnetostrictive constitutive relation that incorporated both applied stress and magnetic field. Their focus was particularly on the tuning of band gaps for logitudinal modes. Bayat and Gordaninejad [98] extend this method to materials with mechanical instabilities. While that work was for magnetoelastic materials, Bayat and Gordaninejad [99] performed similar analysis for magnetorheological materials.

2.2 Methods: Transformation Materials

As we have seen, there are a great many ways of controlling the phonon band structure and tuning it to take certain values at certain frequencies. Much of the existing literature has focused on tuning band gaps and controlling which frequencies can propagate and which are damped, but there have also been efforts to define effective material parameters as a function of tuning signal, control the speed of sound, or control the angle of diffraction. To move towards more complex devices, however, it is useful to have a sense of how material parameters affect phonon dynamics – particularly in the case of effective material parameters. The intuition that is built up from conventional materials does not necessarily apply here, as the material can possess such features as strong anisotropy (angular dependence) and inhomogeneity (spatial variation) and more exotic effects like complex-valued properties, singularities, negative phase velocities, or negative mass (or mass density matrices). A certain degree of useful intuition can be gained from a technique known as transformation materials. In addition to giving intuition, it is also a fruitful technique for determining what material parameters are necessary for generating an arbitrary effect.

2.2.1 Transformation Acoustics

To understand the operation of transformation materials, let's begin by considering the propagation of sound waves (the technique was originally developed for light waves [100, 101, 102]). Expressing equation 1.5 in terms of pressure rather than strain gives

$$\frac{1}{\lambda}\frac{\partial^2}{\partial t^2}p = \nabla \cdot \left(\rho^{-1}\nabla p\right) \tag{2.1}$$

where λ is the bulk modulus tensor ($c_{ijk}{}^{k} = 3\lambda\delta_{ij}$, δ_{ij} is the Kronecker delta), p is the pressure (scalar), and ρ is the mass density tensor. If we transform to a new coordinate system using the Jacobian transformation matrix $J_{ij}(x \rightarrow x') = \partial x_i'/\partial x_j$ this becomes

$$\frac{1}{\lambda}\frac{\partial^2}{\partial t^2}p = \nabla \cdot \left(\frac{J\rho^{-1}J^T}{\det J}\nabla p\right)\frac{1}{\det J} \tag{2.2}$$

which is equivalent to the original equation if we make the substitutions $(\rho^{-1})' = J\rho^{-1}J^T/\det J$ and $\lambda' = \lambda \det J$. Crucially, $p' = p$ so this transformation leaves the pressure field unchanged even as the material is modified [103, 104]. This means that the material parameters effectively define a geometric transformation. Note that this relationship between materials and geometry can be expressed in other terms, as in Leonhardt [101]. A particularly fruitful one [1] is to relate the equation for an inhomogeneous, anisotropic material in Euclidean space

$$\frac{1}{\bar{\lambda}}\partial_{tt}p = \partial_i\left((\bar{\rho}^{-1})^{ij}\partial_j p\right) \tag{2.3}$$

to that of a homogeneous, isotropic medium (denoted by subscript 0) in curvilinear space

$$\frac{\sqrt{g}}{\lambda_0}\partial_{tt}p = \partial_i\left(\rho_0^{-1}\sqrt{g}g^{ij}\partial_j p\right) \tag{2.4}$$

we get the transformation $\bar{\lambda} = \lambda/\sqrt{g}$ and $(\bar{\rho}^{-1})^{ij} = \rho^{-1}\sqrt{g}g^{ij}$. Thus an arbitrary anisotropic, inhomogeneous medium can be mapped to a purely geometric effect, as illustrated in Fig. 2-5. In this picture, to understand how waves propagate in some complicated medium it is not necessary to worry about any details beyond the geometry. This can reduce the problem of understanding wave transport considerably.

2.2.2 Cloaking Transform

Conversely, we can take a geometry that has interesting or unique effects on wave propagation and translate that into a material prescription. This gives an easy way of ascertaining the needed materials for complex or novel devices. By far the most common transformation considered [100, 101, 102, 103, 104, 105] is the expansion of a point to a finite volume

$$r' = a + (b-a) * r/b \tag{2.5}$$

where r is the radial component, a is the radius of the new volume (inner radius of the transformed geometry), and b is the outer radius of the transformed geometry (for $r > b$, the system returns to Euclidean coordinates). Thinking of this transformation in the reverse $(r = b * (r' - a)/(b - a))$, anything within the finite region $r < a$ gets mapped to the point

[1] An approach taken from Leonhardt and Philbin [102] and adapted to acoustics in Sklan [105]. See also Chen and Chan [104] for a more general overview and Greenleaf et al. [106] for a more technical derivation.

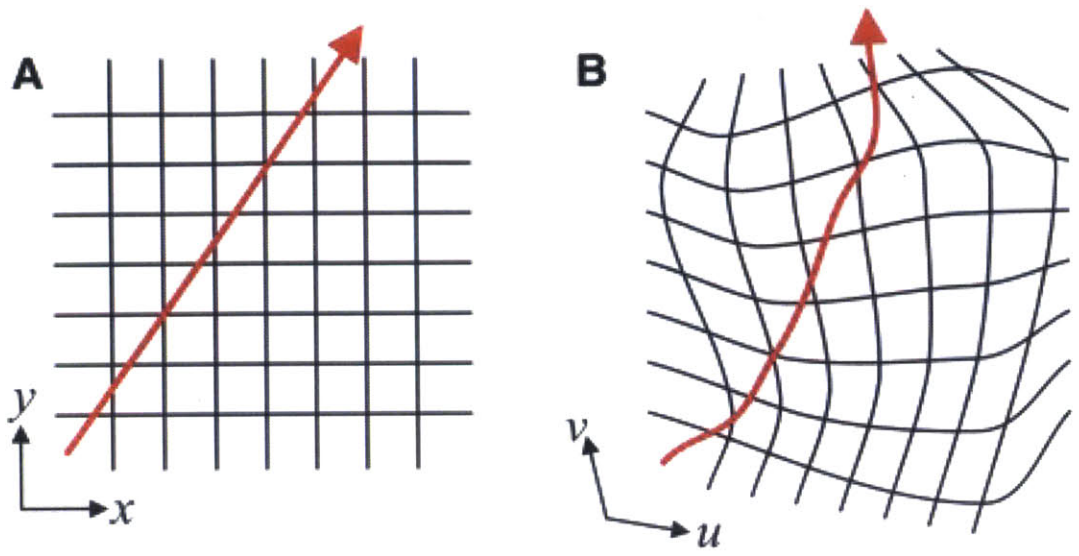

Figure 2-5: Illustration of transformation materials concept. In both (a) and (b) a wave travels in a straight line, but in (b) the geometry is transformed to give a new geodesic. From J. B. Pendry, D. Schurig, and D. R. Smith, *Science* **312**, 5781, 1780-1782 (2006). Reprinted with permission from AAAS [100].

$r = 0$. This has the effect of rendering that entire region invisible, as illustrated in Fig. 2-6. Because the transformation matches the external geometry for $r \geq b$ and is purely geometric for $a < r < b$, waves within the transformed region are radially compressed while waves outside the transformed region are left undeformed. In particular, there is no scattering off of any boundaries – the geometries are matched at $r = b$ and smoothly transform inside the compressed region. This transformation therefore renders a finite region invisible while hiding the evidence of this effect from an external observer. It is therefore referred to as cloaking or a cloak of invisibility.

We now consider the translation of this transformation into a material. For curvilinear coordinates such as are used in the radial transformation, J becomes

$$J = \begin{bmatrix} \frac{g_{u'u'}}{g_{uu}}\frac{\partial u'}{\partial u} & \frac{g_{u'u'}}{g_{vv}}\frac{\partial u'}{\partial v} & \frac{g_{u'u'}}{g_{ww}}\frac{\partial u'}{\partial w} \\ \frac{g_{v'v'}}{g_{uu}}\frac{\partial v'}{\partial u} & \frac{g_{v'v'}}{g_{vv}}\frac{\partial v'}{\partial v} & \frac{g_{v'v'}}{g_{ww}}\frac{\partial v'}{\partial w} \\ \frac{g_{w'w'}}{g_{uu}}\frac{\partial w'}{\partial u} & \frac{g_{w'w'}}{g_{vv}}\frac{\partial w'}{\partial v} & \frac{g_{w'w'}}{g_{ww}}\frac{\partial w'}{\partial w} \end{bmatrix} \tag{2.6}$$

where g is the metric tensor for each coordinate system (primed and unprimed), expressed in terms of a Euclidian reference frame. In the special case of the coordinate systems merely

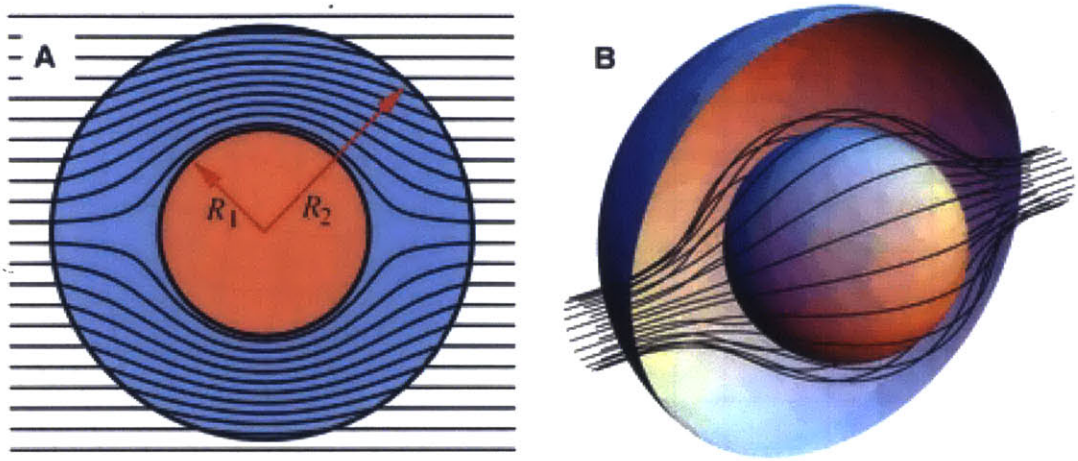

Figure 2-6: Illustration of the cloaking transformation. (a) Cross-section view of the transformed geodesics. (b) Three-dimensional simulation of the geodesics. From J. B. Pendry, D. Schurig, and D. R. Smith, *Science* **312**, 5781, 1780-1782 (2006). Reprinted with permission from AAAS [100].

being a rescaling, as we consider here,

$$J = \text{diag}\left\{\frac{g_{u'u'}}{g_{uu}}\frac{\partial u'}{\partial u}, \frac{g_{v'v'}}{g_{vv}}\frac{\partial v'}{\partial v}, \frac{g_{w'w'}}{g_{ww}}\frac{\partial w'}{\partial w}\right\} \tag{2.7}$$

which allows us to express the metric tensor in terms of these coordinate transformations

$$g = J^{-2} \tag{2.8}$$

For a cylindrical transformation, $g_{rr} = 1 = g_{zz}, g_{\theta\theta} = r$ while $g_{r'r'} = 1 = g_{z'z'}, g_{\theta'\theta'} = r'$, $\partial z/\partial z' = 1 = \partial\theta/\partial\theta'$ and $\partial r/\partial r' = b/(b-a)$ or

$$J = \text{diag}\left\{\frac{b}{b-a}, \frac{b}{r'}\frac{r'-a}{b-a}, 1\right\} \tag{2.9}$$

Plugging everything in gives

$$\bar{\rho}_r = \rho_0\frac{r'}{r'-a} \tag{2.10a}$$

$$\bar{\rho}_\theta = \rho_0\frac{r'-a}{r'} \tag{2.10b}$$

$$\bar{\rho}_z = \rho_0\left(\frac{b-a}{b}\right)^2\frac{r'}{r'-a} \tag{2.10c}$$

$$\bar{\lambda} = \lambda_0\left(\frac{b-a}{b}\right)^2\frac{r'}{r'-a} \tag{2.10d}$$

where, again, r' refers to the radial component between a and b in the cloaked frame. Note that in the special case of a two-dimensional transformation, ρ_z is neglected as there is no spatial variation of the waves along this axis. On the other hand, for a spherical transformation

$$\bar{\rho}_r = \rho_0 \frac{b-a}{b}\left(\frac{r'}{r'-a}\right) \tag{2.11a}$$

$$\bar{\rho}_\theta = \rho_0 \frac{b-a}{b} \tag{2.11b}$$

$$\bar{\rho}_\phi = \rho_0 \frac{b-a}{b} \tag{2.11c}$$

$$\bar{\lambda} = \lambda_0 \left(\frac{b-a}{b}\right)^3 \left(\frac{r'}{r'-a}\right)^2. \tag{2.11d}$$

In practice, these equations are sufficiently similar that most theoretical work is done for the two-dimensional cloak, while most experimental work is done for the spherical cloak (although there are other approaches, such as the carpet cloak first proposed by Li and Pendry [107, 108, 109] or the use of complementary media and external cloaks developed by Lai et al. [110, 111, 112]).

2.2.3 Realistic Cloaks

There are several important features to these transformation equations. They require an anisotropic mass density matrix, something that often requires artificially structured (meta-materials) materials to achieve. They also necessitate continuous functions to go from their background values at $r = b$ to singular values at $r = a$. The requirement of a singularity at the boundary, however, is particularly difficult to achieve. In optics, this sort of singularity impossible for more than individual frequencies, as it implies a velocity in excess of the speed of light (since light must travel a longer distance around the cloaked region and still be faster than passing through the cloaked region). While acoustics is not so stringent, in practice this singularity is often relaxed. This can induce errors in the transformation equation, such as the lack of phase matching in Leonhardt and Tyc's non-Euclidean cloak [113]. It has been shown in multiple ways [114, 115] that a perfect cloak is truly perfect, and will block any component aside from a constant corresponding to the mean value of its

surrounding field (e.g. electric potential, pressure)[2] [116, 117, 105]. To help characterize the effect of errors in a perfect cloak, Ruan et al. [118] considered the effect of removing a thin layer of thickness δ from the inner lining of the cloak and then using scattering theory to determine how the magnitude of the scattering depends upon δ. They found that the scattering field converges to 0, but does so extremely slowly – less than $o(\delta)$. Isić et al. [119] perform a similar analysis and show that it decays like $1/\ln\delta$. We will illustrate their methods more explicitly in Ch. 2.3.5, where there will be a concrete example to consider. Zhang et al. [120] studies the creation of surface modes on the inner boundary of the cloak and the development of zero power transmitting penetrating modes.

2.2.4 Thermal Cloaks

Concurrent with these efforts to understand the behavior of electromagnetic and acoustic cloaks, other people were seeking to extend these techniques. Devices like a concentrator (which does the opposite of a cloak and pulls waves towards the center [121, 122]), rotators [123, 124, 125], illusion techniques (making an object appear like another, or like multiple copies of itself [126, 127, 128, 129, 130, 131, 132]), and space-time cloaks (extending the formalism to allow for temporal transformations from moving media, thereby cloaking events rather than objects [133]) were developed using other coordinate transformations. Additionally, the transformation materials was applied to other classes of wave phenomena [134, 135, 136, 137, 138, 139, 140, 141, 142] and to diffusion effects [143, 144, 145]. In particular, it was shown that both the ballistic transport of phonons illustrated in the acoustics examples above, but also the diffusive transport of phonons by the heat equation met the transformation materials requirements [146, 147, 148, 149, 150, 151, 152, 153]. Guenneau et al. [147] first proposed the transformation, Schittny et al. [148] and Ma et al. [150] developed designs for the cloak. Narayana et al. [149] developed a design for quasistatic heat flux rather than temperature Narayana and Sato [151] experimentally tested this design. Li et al. [153] developed a simultaneous cloak for light and temperature. Guenneau and Amra [154] designed a thermal rotator (also tested in Naranaya and Sato TC6). He and Wu [155]

[2]This can be seen by noting that the steady state mean value takes the form $\nabla^2 f = 0$, or Laplace's equation. This eigenvalue equation obeys the property $f(r_0) = \iint_{S(a)} f dA / \iint_{S(r_0)} dA$ for any sphere centered at r_0 (i.e. $S(r_0)$. In other words, the value at the center of a sphere is necessarily equal to the mean value over the sphere's surface.

designed a thermal illusion device.

To demonstrate the transformation materials prescription for diffusive phonon transport, we begin with the heat equation

$$\rho c_p \partial_t T = \partial_i \left(\kappa^{ij} \partial_j T \right) \tag{2.12}$$

where ρ is the density, c_p the specific heat capacity, T temperature, and κ the thermal conductivity. Following the standard method, we change coordinates

$$\sqrt{g} \rho' c_p' \partial_t T = \partial_i \left(\kappa \sqrt{g} g^{ij} \partial_j T \right). \tag{2.13}$$

So

$$\bar{\kappa}^{ij} = \kappa_0 \sqrt{g} g^i j \tag{2.14a}$$

$$\bar{\rho}\bar{c}_p = \rho_0 c_{p0} \sqrt{g} g^{ij} \tag{2.14b}$$

Taking the two-dimensional circular cloak for concreteness gives

$$\bar{\kappa}_r = \kappa_0 \frac{r' - a}{r'} \tag{2.15a}$$

$$\bar{\kappa}_\theta = \kappa_0 \frac{r'}{r' - a} \tag{2.15b}$$

$$\bar{\rho}\bar{c}_p = \rho_0 c_{p0} \left(\frac{b}{b-a} \right)^2 \frac{r' - a}{r'}. \tag{2.15c}$$

Note that these have different forms than the material parameters of equation 2.10a-c, but there are clear similarities due to their shared geometric origin. In particular, these similarities allow theoretical work on cylindrical cloaks to be applied to experimentally realized spherical cloaks with only minor modification.

2.3 Testing the Accuracy of Diffusive Cloaks

While the transformations involved in the construction of a thermal cloak bear some resemblance to those used in other cloaking devices, it is important to remember that they are not the same. Not only are the materials different, but the equations are fundamentally different. Prior to the treatment of the heat equation, all transformation media techniques had been applied solely to the wave equation (a hyperbolic partial differential equation) or Laplace's equation (an elliptic partial differential equation). The heat equation is a diffusion equation, and therefore a parabolic partial differential equation. What this means is that signals propagate differently for the thermal cloak than for the previously analyzed cloaks. The standard picture of far-field scattering does not necessarily apply. This difference is exacerbated by the material differences between the acoustic or optical wave equations and the heat equation. The range of available materials and the need to achieve something approaching a singularity at the inner boundary necessarily limits the performance of any cloak.

To make a realizable cloak, previous researchers [148, 150, 151] have focused particularly on the engineering of the thermal conductivity κ. While it was clearly understood that the necessity of using real materials kept them from reaching the perfect inner boundary, improved fabrication techniques allowed them to push the limits of what had been achieved [3]. The need to engineer the volumetric heat capacity ρc_p, on the other hand, was assumed to be negligible. In part, this was due to the choice of experimental tests applied to the thermal cloak, namely the application of fixed temperatures at opposite sides of a domain surrounding the cloak (see Fig. 2-7). Since ρc_p only appears in conjunction with time derivatives of the temperature, the onset of a stationary steady state solution eliminates the heat capacity. It has no effect on the steady state temperature distribution, just the transient component. On the other hand, the utility of a cloak that only works in an unchanging environment is fairly limited. At most, it can regulate temperature distributions; say by acting as a thermal insulator.

[3] In particular the ability to fabricate micron and nanoscale resonators led to the development of metamaterials (materials whose properties are determined by their structure not their chemical composition). Metamaterials were essential in providing the material properties required for the earliest cloaks [100]. Similarly, greater resolution in nanofabrication allows for greater flexibility in engineering the thermal conductivity.

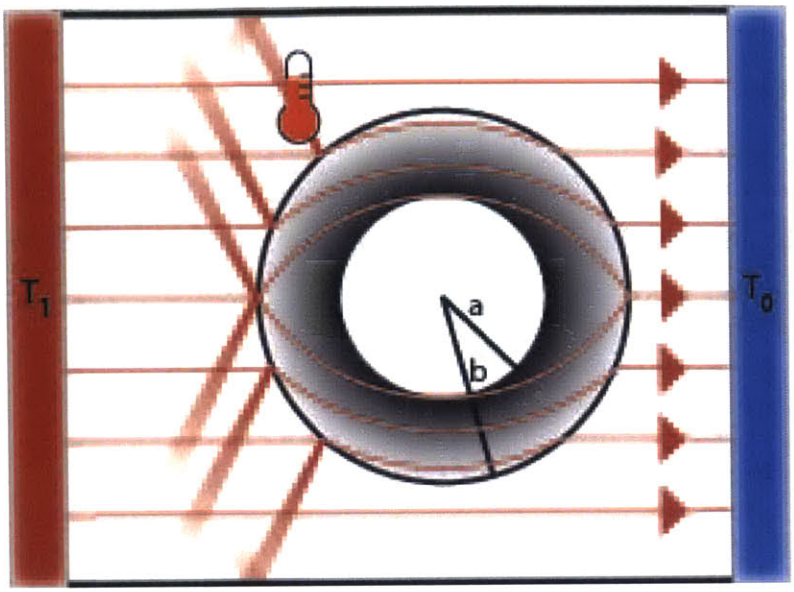

Figure 2-7: Model for finding the location of a thermal cloak of radius b with cloaked domain of radius a. Two heat baths (red and blue rectangles) are placed at opposite sides of the cloak, which is confined to a thermally isolated domain. Heat flows between the baths (red lines), passing through a perfect cloak without distortion. For an imperfect cloak, however, heat is also scattered from the boundaries of the cloak. Although the scattered heat diffuses, a thermometer near the cloakâĂŹs surface can detect it. From Sklan et al. [156].

In recognition of this fact, many researchers have focused on the transient effects [147, 148, 150]. There too, the testing of the cloak's performance has been largely qualitative. Moreover, they have assumed that the replacement of an inhomogeneous heat capacity with a constant one is negligible even in this regime. Schittny et al. [148], for example, employ an approximate cloak design developed in Guenneau et al. [147] (where constant ρc_p was explicitly assumed) while still claiming to achieve transient thermal cloaking. Indeed, they even observed in their experiments that the specific heat was not constant in their device, but they sought to correct for this deviation from their homogeneous ρc_p model. Additionally, Ma et al. [150], simplify their transient cloak design by assuming that ρc_p commutes with spatial derivatives to good approximation, which immediately implies that ρc_p is approximately homogeneous. Due to this confusion, other researchers have sought to extend thermal cloaking to other diffusive transport problems, particularly chemical diffusion. Chemical diffusion obeys the equation $\partial_t n = \nabla \cdot (D_n \nabla n)$ for chemical concentration n and diffusion constant D_n. Researchers [143, 144] have again assumed that, because ρc_p was negligible for $\omega \equiv 0$ steady state thermal cloaks, the steady state thermal cloak designs

translate directly into time-dependent chemical diffusion cloaks (despite the fact that such an analogy maps ρc_p to unity everywhere).

In this section, we therefore analyze the performance of this class of thermal cloaking (i.e. cloaks which rely upon engineering κ but neglect ρc_p), which we term the steady state cloak.

2.3.1 Scattering Solutions to the Cloaked Heat Equation

Understanding the perfect cloak's connection to the background medium is foundational to understanding the steady state cloak Starting from equation 2.12, we can take the Fourier transform in time and use a separable solution (in polar coordinates) $T(r,\theta,t) = R(r)\Theta(\theta)\tilde{T}(t)$ to get

$$\frac{i\omega\rho_0 c_{p0}}{\kappa_0}R = \frac{1}{r}\frac{d}{dr}(r\frac{d}{dr}R) - \frac{l^2}{r^2}R \tag{2.16}$$

where l is the eigenvalue to the θ dependent portion of the separated equation, ω is the eigenvalue of the time dependent portion of the separated equation, $\rho_0 c_{p0}$ is the volumetric specific heat of the background medium, κ_0 is the thermal conductivity of the background medium, and i is $\sqrt{-1}$. This can be re-written as the differential equation defining the modified Bessel functions (either $I_l(z)$ or $K_l(z)$ [158]) by making a change of variables $z = \sqrt{\frac{i\omega\rho_0 c_{p0}}{\kappa_0}}r$ for $\omega \neq 0$. Hence, the time-dependent (i.e. the transient regime) solution has eigenfunctions of the form

$$T_l^{(tr)}(r,\theta,\omega) = \left(a_l I_l(z) + b_l K_l(z)\right) e^{il\theta + i\omega t}. \tag{2.17}$$

with a_l and b_l being arbitrary constants determined by the initial and boundary conditions.

On the other hand, when $\omega = 0$ (i.e. the steady state) the temperature distribution becomes defined by the solution to Laplace's equation

$$T_l^{(SS)}(r,\theta) = \left(A_l r^l + B_l r^{-l}\right) e^{il\theta} \tag{2.18}$$

for $l \neq 0$ (A_l and B_l are generalizations of a_l and b_l) and

$$T_0^{(SS)} = A_0 + B_0 \ln(r) \tag{2.19}$$

for $l = 0$. Thus, the general solution can be written $T(r, \theta, \omega) = \Sigma_{l=0}^{\infty} T_l^{(SS)} + T_l^{(tr)}$.

When considering the perfect cloak (PC) defined by equation 2.15a, we can use the old coordinate transformation of

$$r' = \frac{b}{b-a}(r-a) \tag{2.20}$$

(again, b is the exterior radius of the cloak, a is the radius of the cloaked domain, r' is the coordinate system – in real space – inside the cloak, r is the coordinate system of the mathematically equivalent geometry defined in Ch. 2.2) to reduce the solution in the primed coordinates to the homogeneous case defined be equation 2.12. Specifically, we use solutions that depend upon the new effective position $z = \sqrt{i}b/(b-a) * k_0 r$, where $k_0 = \sqrt{\omega \rho_0 c_{p0}/\kappa_0}$ is the effective thermal wave vector of the homogeneous background.

For a steady state cloak (SSC) the material parameters are

$$\bar{\kappa}_r = \kappa_0 \frac{r'-a}{r'} \tag{2.21a}$$

$$\bar{\kappa}_\theta = \kappa_0 \frac{r'}{r'-a} \tag{2.21b}$$

$$\bar{\rho}\bar{c}_p = \rho_0 c_{p0} \left(\frac{b}{b-a}\right) \eta. \tag{2.21c}$$

where η measures the impedance mismatch between the cloak's outer boundary and the background ($\eta = 1$ is impedance matched). We can no longer use the coordinate transformation trick but instead must brute-force the solution (following Sklan et al. [156]). Using a new effective position variable $x = \sqrt{i\omega\rho_0 c_{p0}\eta b/\kappa_0(b-a)}(r-a)$ and again assuming a separable solution gives

$$0 = \partial_x(x\partial_x R) - \left[\frac{l^2}{x} + x + Ka\right] R \tag{2.22}$$

where $K = \sqrt{i\omega\rho_0 c_{p0}\eta b/\kappa_0(b-a)}$. We solve this equation by means of the method of Frobenius $R_l(x) = \Sigma b_{nl}^{\pm} x^{n\pm l}$ with recurrence relation [156]

$$b_{nl}^{\pm} = \frac{1}{n(n \pm 2l)}(Kab_{n-1,l}^{\pm} + b_{n-2,l}^{\pm}). \tag{2.23}$$

Cloak	κ_r/κ_0	κ_θ/κ_0	$\rho c_p/\rho_0 c_{p0}$
PC	$(r-a)/r$	$r/(r-a)$	$[b/(b-a)]^2(r-a)/r$
SSC (M)	$(r-a)/r$	$r/(r-a)$	$b/(b-a)$
SSC(Mis)	$(r-a)/r$	$r/(r-a)$	$[b/(b-a)]^2$
BC $\{r \in (a, r_1)\}$	κ_1/κ_0	κ_1/κ_0	$\rho_1 c_{p1}/\rho_0 c_{p0}$
BC $\{r \in (r_1, b)\}$	κ_2/κ_0	κ_2/κ_0	$\rho_2 c_{p2}/\rho_0 c_{p0}$

Table 2.1: Parameters for the cloaks considered in this section. Perfect cloak (PC), impedance matched steady state cloak (SSC (M)), impedance mismatched SSC (SSC (Mis)) ($\eta \equiv b/(b-a)$), and bilayer cloak (BC). The inner layer of the cloak has radius a while the outer layer radius b, as in Fig. 2-7. From Sklan et al. [156]

This recurrence relation is gives the exact solution, but we can gain some additional insight through expanding the solution by powers of Ka. Even terms in the series become

$$b_{2m,l}^{\pm(0)} = \frac{1}{2m(2m \pm 2l)} b_{2m-2,l}^{\pm(0)} + O\left([Ka]^2\right) \tag{2.24}$$

which is the same as series expansion for I_l (for +) and K_l (for -). Whereas, for odd terms the relation depends upon every lower-power even term and so becomes

$$b_{2m+1,l}^{\pm(0)} = Ka \sum_{n=0}^{m} \frac{|2n-1|!!}{(2m+1)!!} \frac{(2n \pm 2l - 1)!!}{(2m \pm 2l + 1)!!} b_{2n,l}^{\pm(0)} + O\left([Ka]^3\right) \tag{2.25}$$

(!! is the factorial of only odd terms). Because $b_{2m+1,l}^{\pm(0)}$ is completely determined by $b_{2n,l}^{\pm(0)}$ the odd terms are therefore a function of the modified Bessel functions. Ergo, we term these components $\mathcal{F}[R_l(x)]$ [156]. [4] Unfortunately, $\mathcal{F}[R_l(x)]$ is not a tabulated function, so this is as far as we can get by purely analytical techniques. Note, though, that $\mathcal{F}[R_l(x)]$ is an additional term in the solution whose presence reveals a deviation from the background (even in the impedance matched case). This is therefore the equivalent of the scattering field for the steady state cloak. Note too that the strength of the scattering field is determined by the perturbative expansion of Ka, a dimensionless parameter that depends upon the size of the cloaked region. Decreasing the size of the cloaked domain therefore improves the performance of the cloak. For reference, the various cloaks considered in this section are summarized in Table 2.1

[4] For spherical cloaks, the derivation is equivalent save for the replacement of l with $l + 1/2$.

2.3.2 Simulation of the SSC

To proceed with analyzing this scattering field $\mathcal{F}[R_l(x)]$, we turn to COMSOL multiphysics [157], a finite element simulation method. To aid in comparison with experiments, we use a rectangular domain (dimensions L =70 mm by $L_\perp$ =50 mm) centered around a cloak (dimension a =13 mm, b =20 mm) with one pair of edges at fixed temperature and the other pair thermally insulating (Fig. 2-7). Given the linearity of eq. 2.12, one boundary's temperature is set to 0 (as is the initial T) while the other's is set to 1 (so $\Delta T \equiv 1$). It is helpful to use the natural units of L (the separation of the heat sources) and the diffusion time $\tau_D = L^2\rho_0 c_{p0}/\kappa_0$. Since the background medium is $\kappa_0 = 71.4\text{W/m}\cdot\text{K}$, $\rho_0 = 2100\text{kg/m}^3$, and $c_{p0} = 1000\text{J/kg}\cdot\text{K}$, the diffusivity is $D = \kappa_0/\rho_0 c_{p0} = 3.4\cdot 10^{-5}\text{m}^2/\text{s}$ and therefore the diffusion timescale is $\tau_D = L^2/D = 144.12\text{s}$.

Using these conditions, our simulations give Fig. 2-8, where each column is a snapshot at a different time. The first row is the case of a homogeneous background, such as would be observed if the cloak were absent. The second is the solution to SSC (with $\eta = b/(b-a)$ to increase contrast), i.e. what would be observed with the cloak present. The third is the difference between the first and second rows $\delta T = T^{(SSC)}(\vec{r},t) - T^{(H)}(\vec{r},t)$. This signal δT is the deviation from the expected background and as such is the signal whose detection is tantamount to the detection of a thermal cloak. δT is initially small and principally confined to the region of the cloak's surface that has been heated (see Fig. 2-8g). However, in Fig. 2-8h δT later grows and becomes observable to outside observers. When the solution reaches steady state in Fig. 2-8i, invisibility is restored; as would be expected for a steady state cloak (SSC) ($\delta T \neq 0$ is confined to within the cloak).

2.3.3 Time and Space Dependences of the Deviation of the SSC

To gain a better sense of what is going on between snapshots, we analyze δT for several points outside the cloak. In particular, in Fig. 2-9 we compare δT for the SSC with $\eta = 1$ (i.e. impedance matched case, where the cloak has the same properties as a PC at $r = b$), $\eta = b/(b-a) > 1$ (impedance mismatched but with $\sqrt{\eta}k_S = k_C$), and the PC. As $\delta T \equiv 0$ outside of a perfect cloak (this will be proven in Ch. 2.3.5), any deviation for the PC must be

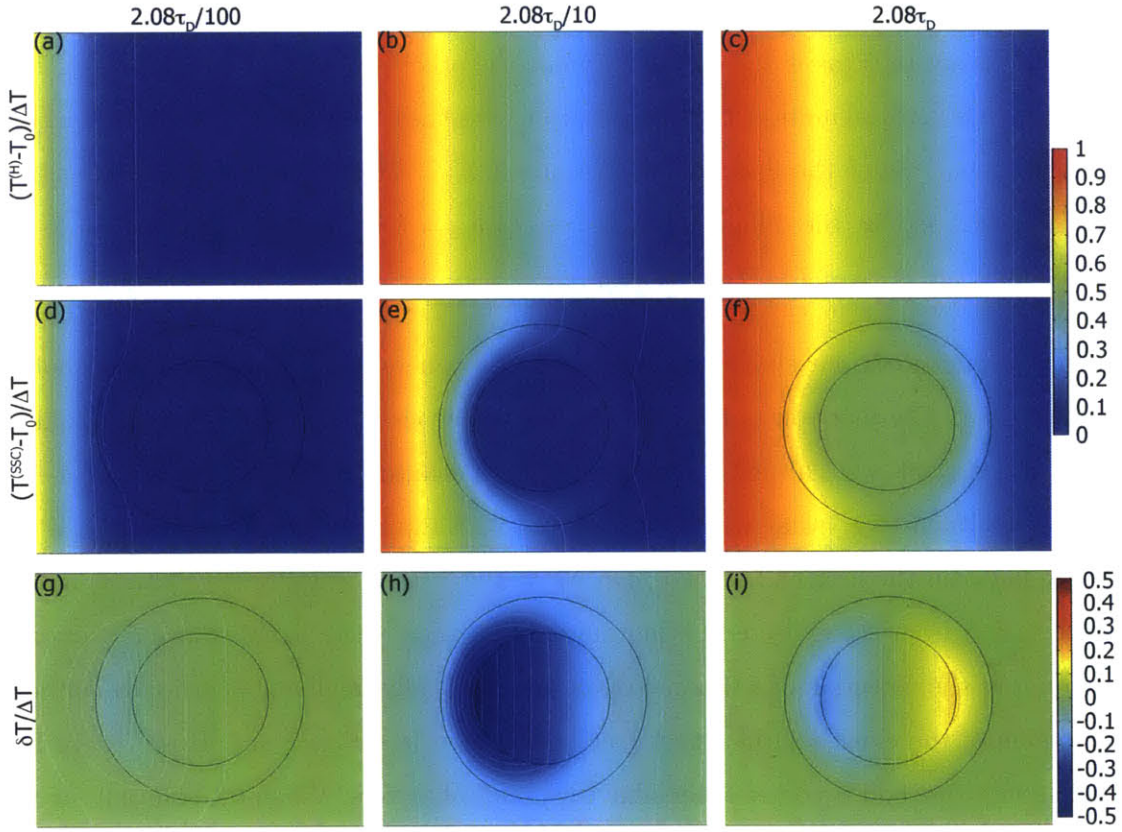

Figure 2-8: Simulation of detecting the temperature profile of a mismatched SSC ($\eta = b/(b-a)$). Columns correspond to $2.08\tau_D/100$, $2.08\tau_D/10$, and $2.08\tau_D$ respectively. Rows correspond to the homogeneous case (no cloak), SSC, and $T^{(SSC)} - T^{(H)}$. Black circles denote the location of the cloak (for reference in the homogeneous case), colored domains are isotherms, and grey lines are constant separation isotherms. From Sklan et al. [156].

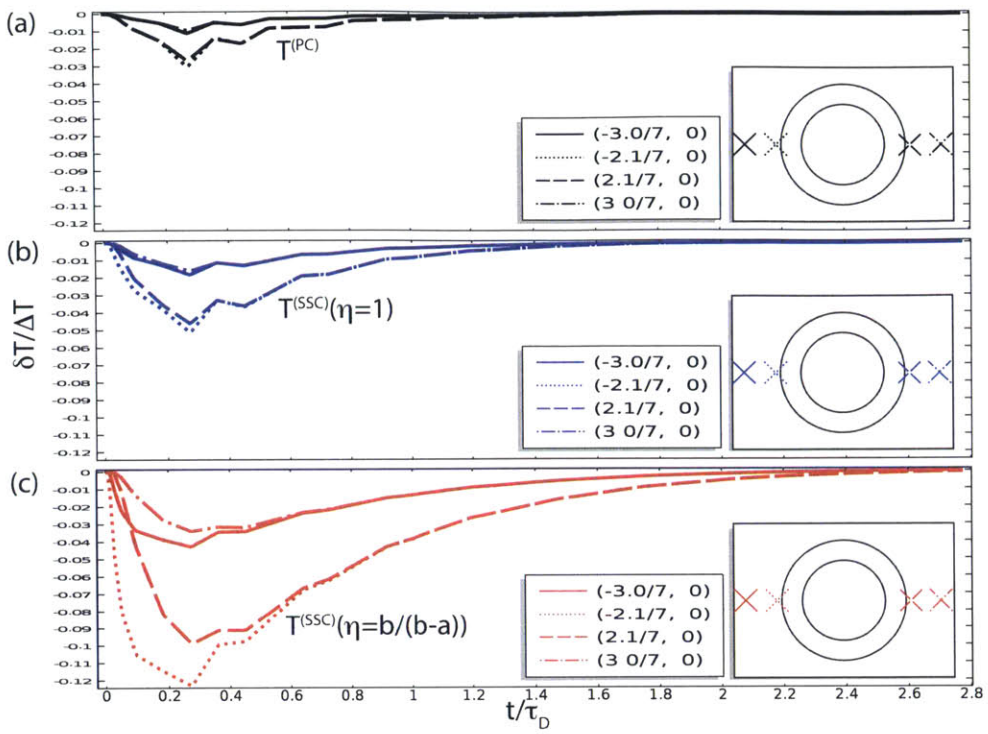

Figure 2-9: Time evolution of the temperature deviation δT at representative points outside the cloak. Black (a), blue (b), and red (c) curves denote the PC, impedance matched SSC, and impedance mismatched SSC. Line styles correspond to individual points, shown in the insets. From Sklan et al. [156].

a numerical artifact of discretizing κ and thereby removing $\kappa_\theta \to \infty$ [5]. However, regardless of impedance $\delta T^{(SSC)} > \delta T^{(PC)}$ outside the cloak, i.e. the SSC performs worse. This is the signature of relying upon a homogeneous ρc_p.

Somewhat surprisingly, the position dependence of δT is approximately just a scaling factor and so the extrema at different locations all nearly coincide instead of being separated by a propagation time. To clarify this, in Fig. 2-10 we examine several slices of δT along y =constant for $t = 2.08\tau_D/100$, $2.08\tau_D/10$, and $2.08\tau_D$ (or 3s, 30s, and 300s) (blue, green, and red lines, respectively) to observe the spatial dependence more precisely. The slices are chosen to be centered on the cloak, slightly offset, and outside the cloak. The perturbation is initially limited to where the cloak that has been reached by the applied heat current. As time passes and heat spreads, δT too grows and spreads throughout the domain. When everything approaches steady state, δT falls. The linear dependence inside the cloak for

[5] In 2.3.5 we show that removal of this singularity introduces scattering fields which scale to lowest order like $1/\ln k_C \delta$, where δ is the deviation at the inner boundary and $k_C = b/(b-a)k_0$

steady state implies that $T^{(SSC)}$ inside this domain is essentially constant. Outside the cloak δT is effectively a sine curve. This is clearest for the slice outside the cloak [6], but even for the other two their linear drop-off away from the surface of the cloak corresponds to the linear section of a sine curve.

2.3.4 Time-dependence of the Temperature Difference

The results of Figs. 2-9 and 2-10 make for a surprising result. Unlike in the conventional wave picture, our scattering field here does not actually propagate. Instead, it is closer to a damped standing wave pattern. To see how such a phenomenon could arise, consider equation 2.12 for some arbitrary domain

$$\rho C \partial_t T = \nabla \cdot (\kappa \nabla T) \tag{2.26a}$$

$$T(\vec{r}, 0) = T_i \tag{2.26b}$$

$$T(\partial r, t) = T_{r_i} \tag{2.26c}$$

where ∂r are the boundaries of the domain and the boundary conditions are stationary. In this case, there exists a steady state profile $\partial_t T^{(SS)} = 0$ that uniquely satisfies the boundary conditions. By linearity, $T = T^{(SS)} + T^{(tr)}$ where the transient term is defined by

$$\rho C \partial_t T^{(tr)} = \nabla \cdot \left(\kappa \nabla T^{(tr)}\right) \tag{2.27a}$$

$$T^{(tr)}(\vec{r}, 0) = T_i - T^{(SS)} \tag{2.27b}$$

$$T^{(tr)}(\partial r, t) = 0. \tag{2.27c}$$

Assuming that, for some frame, the materials are everywhere homogeneous, we can Fourier transform over space ($\nabla^2 T^{(tr)} \equiv -k^2 T^{(tr)}$) to get

$$T^{(tr)}(\vec{r}, t) = \int T^{(tr)}(\vec{k}, 0) e^{-k^2 D t} e^{-ik \cdot r} \frac{d^n k}{(2\pi)^{n/2}} \tag{2.28a}$$

$$T^{(tr)}(\vec{k}, 0) = \int e^{ik \cdot r} \left[T_i - T^{(SS)}(\vec{r})\right] \frac{d^n r}{(2\pi)^{n/2}}, \tag{2.28b}$$

[6] Except for the initial curve, which contains higher terms that decay faster than the fundamental mode

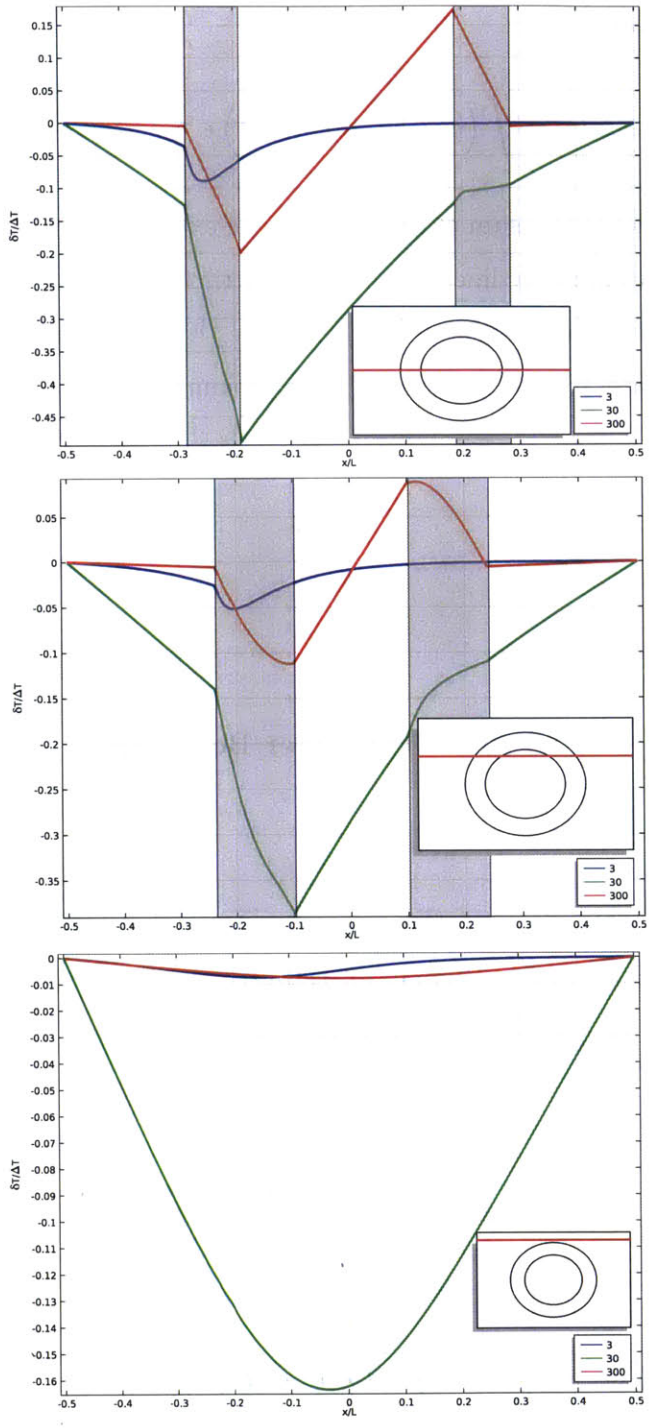

Figure 2-10: Space dependence of δT of the SSC. Slices are along the middle of the cloak (plot (a), $y = 0$), slightly offset from the center (plot (b)$y = 1.1/7$), and outside the cloak (plot (c) $y = 2.2/7$). The blue, green, and red curves are at $2.08\tau_D/100$, $2.08\tau_D/10$, and $2.08\tau_D$, respectively. From Sklan et al. [156].

where $D = \kappa_0/\rho_0 c_{p0}$ is the thermal diffusivity. If two systems only differ in ρc_p, their temperature difference becomes

$$\delta T(\vec{r}, t; \Delta D) = \int \left(e^{-k^2 D_a t} - e^{-k^2 D_b t}\right) e^{-ik\cdot r} \frac{T^{(tr)}(\vec{k}, 0) d^n k}{(2\pi)^{n/2}}. \tag{2.29}$$

Ergo, the time dependence is a sum of the difference of exponentially decaying terms. So for short times δT is approximately linear while for long time scales it decays exponentially. If only one Fourier mode is excited then δT is separable. If a small number of well separated Fourier modes dominate $T^{(tr)}(\vec{k}, 0)$ then δT is approximately separable, as we see in Fig. 2-9.

2.3.5 Sensitivity of a Cloak to the Inner Boundary

To determine the role of the discretization in our simulations, we next turn a direct extension of the scattering solutions used in Ruan et al. [118] to consider a PC that has lost a section of the inner boundary of thickness δ. We showed with equation 2.17 that the solution for $\omega \neq 0$ takes the form

$$T_l^{(tr)}(r, \theta, \omega) = (a_l I_l(z) + b_l . K_l(z))\, e^{il\theta + i\omega t} \tag{2.30}$$

Whereas the steady state of $\omega = 0$ has solutions following equation 2.18

$$T_l^{(SS)}(r, \theta) = \left(A_l r^l + B_l r^{-l}\right) e^{il\theta} \tag{2.31}$$

for $l \neq 0$ and equation 2.19

$$T_0^{(SS)} = A_0 + B_0 \ln(r) \tag{2.32}$$

for $l = 0$. The domains I, II, III are defined to be external to the cloak, inside the cloak, and the cloaked region. The boundary conditions (continuity of T and $\hat{n} \cdot \kappa \nabla T$) relating

these domains are

$$\begin{aligned}
a_l^{(I)} I_l(\sqrt{i}k_B b) + b_l^{(I)} K_l(\sqrt{i}k_B b) &= a_l^{(II)} I_l(\sqrt{i}k_C[b-a]) \\
&\quad + b_l^{(II)} K_l(\sqrt{i}k_C[b-a]) \qquad (2.33a) \\
\kappa_0 k_B \left[a_l^{(I)} I_l'(\sqrt{i}k_B b) + b_l^{(I)} K_l'(\sqrt{i}k_B b)\right] &= \kappa_r k_C \left[a_l^{(II)} I_l'(\sqrt{i}k_C[b-a])\right. \\
&\quad \left. + b_l^{(II)} K_l'(\sqrt{i}k_C[b-a])\right] \qquad (2.33b) \\
a_l^{(III)} I_l(\sqrt{i}k_B[a+\delta]) &= a_l^{(II)} I_l(\sqrt{i}k_C\delta) + b_l^{(II)} K_l(\sqrt{i}k_C\delta) \qquad (2.33c) \\
\kappa_0 k_B a_l^{(III)} I_l'(\sqrt{i}k_B[a+\delta]) &= \kappa_r k_C \left[a_l^{(II)} I_l'(\sqrt{i}k_C\delta)\right. \\
&\quad \left. + b_l^{(II)} K_l'(\sqrt{i}k_C\delta)\right], \qquad (2.33d)
\end{aligned}$$

where $k_B = \sqrt{\omega\rho_0 c_{p0}/\kappa_0}$ and $(b-a)k_C = bk_B$ (the diffusive wave vector for 2.21a). In particular, the incident field is $a_l^{(I)}$, the scattered field is $b_l^{(I)}$, and the penetrating field is $a_l^{(III)}$. Note that we have expanded our solution using the eigenfunctions found in Sec. 2.3.1 and that $b_l^{(III)}$ is tautologically 0 since $K_l(0)$ diverges. Using these definitions of k and κ from 2.21a the first boundary conditions can be rewritten

$$\begin{aligned}
a_l^{(I)} I_l(\sqrt{i}k_B b) + b_l^{(I)} K_l(\sqrt{i}k_B b) &= a_l^{(II)} I_l(\sqrt{i}k_B b) + b_l^{(II)} K_l(\sqrt{i}k_B b) \qquad (2.34a) \\
a_l^{(I)} I_l'(\sqrt{i}k_B b) + b_l^{(I)} K_l'(\sqrt{i}k_B b) &= a_l^{(II)} I_l'(\sqrt{i}k_B b) + b_l^{(II)} K_l'(\sqrt{i}k_B b), \qquad (2.34b)
\end{aligned}$$

which, for an arbitrary cloak radius b implies that $a_l^{(II)} = a_l^{(I)}$ and $b_l^{(II)} = b_l^{(I)}$. Using the last two boundary conditions and the identity for the Wronskian of modified Bessel functions $\mathcal{W}[I_l(z), K_l(z)] = -1/z$ [158] gives

$$\begin{aligned}
\frac{a_l^{(III)}}{a_l^{(I)}} &= \frac{-(\sqrt{i}k_B a)^{-1}}{\frac{\delta}{a+\delta}\frac{b}{b-a} K_l'(\sqrt{i}k_C\delta) I_l(\sqrt{i}k_B[a+\delta]) - I_l'(\sqrt{i}k_B[a+\delta]) K_l(\sqrt{i}k_C\delta)} \qquad (2.35a) \\
\frac{b_l^{(I)}}{a_l^{(I)}} &= \frac{I_l(\sqrt{i}k_C\delta) I_l'(\sqrt{i}k_B[a+\delta]) - \frac{\delta}{a+\delta}\frac{b}{b-a} I_l'(\sqrt{i}k_C\delta) I_l(\sqrt{i}k_B[a+\delta])}{\frac{\delta}{a+\delta}\frac{b}{b-a} K_l'(\sqrt{i}k_C\delta) I_l(\sqrt{i}k_B[a+\delta]) - I_l'(\sqrt{i}k_B[a+\delta]) K_l(\sqrt{i}k_C\delta)} \qquad (2.35b)
\end{aligned}$$

which can be expanded in the limit $\delta \to 0$. When $l \neq 0$ this becomes

$$\begin{aligned}
a_l^{(III)} &\approx \frac{(\frac{1}{2}\sqrt{i}k_C\delta)^l}{(l-1)!} \frac{(\sqrt{i}k_B a)^{-1}}{l(\frac{1}{2}\sqrt{i}k_B a)^{-1} I_l(\sqrt{i}k_B a) + \frac{1}{2} I_l'(\sqrt{i}k_B a)} a_l^{(I)} \qquad (2.36a) \\
b_l^{(I)} &\approx \frac{2(\frac{1}{2}\sqrt{i}k_C\delta)^{2l}}{l[(l-1)!]^2} \frac{l(\sqrt{i}k_B a)^{-1} I_l(\sqrt{i}k_B a) - I_l'(\sqrt{i}k_B a)}{4l(\sqrt{i}k_B a)^{-1} I_l(\sqrt{i}k_B a) + I_l'(\sqrt{i}k_B a)} a_l^{(I)}, \qquad (2.36b)
\end{aligned}$$

which vanish at $\delta = 0$. Whereas for $l = 0$ this becomes

$$a_0^{(III)} \approx -\frac{1}{(\sqrt{i}k_B a)I_0'(\sqrt{i}k_B a)\ln k_C\delta} a_0^{(I)} \tag{2.37a}$$

$$b_0^{(I)} \approx \frac{1}{\ln k_C\delta} a_0^{(I)}, \tag{2.37b}$$

which converges more slowly but again vanishes at $\delta = 0$. For $\omega = 0$ repeating this procedure gives

$$A_l^{(II)} = \left(\frac{b}{b-a}\right)^l A_l^{(I)} \tag{2.38a}$$

$$A_l^{(III)} = \frac{2b-2a}{2b-a}\left(\frac{b}{b-a}\frac{\delta}{a}\right)^l A_l^{(I)} \tag{2.38b}$$

$$B_l^{(I)} = \frac{-a}{2b-a}\left(\frac{b}{b-a}\delta\right)^{2l} A_l^{(I)} \tag{2.38c}$$

$$B_l^{(II)} = \frac{-a}{2b-a}\delta^{2l} A_l^{(I)} \tag{2.38d}$$

for $l \neq 0$ and $A_0^{(I)} = A_0^{(II)} = A_0^{(III)}$, $B_0^{(I)} = B_0^{(II)} = 0$ for $l = 0$ [156]. Ergo, when $\delta \to 0$ the temperature inside the cloak is constant and the there is no scattering. We therefore see that, as the name implies, a PC is a perfect cloak but even slight deviations from this can create strong scattering.

2.3.6 Experimental Test of SSC Deviations: The Bilayer Cloak

While the SSC model uses a realistic ρc_p, it still contains an idealized κ. Thus, to compare with experiments we must use discretized rings of constant κ. Specifically, we consider the bilayer cloak (BC) [159] [7]. Simulations were done using a rectangular domain of dimensions L =45 mm by $L_\perp$ =45 mm centered around a cloak with parameters given by Table 2.2. This gives a diffusivity of $D_0 = \kappa_0/\rho_0 c_{p0} = 7.67 \cdot 10^{-7}\text{m}^2/\text{s}$ and diffusion timescale $\tau_{D_0} = L^2/D$ = 2641.3s. The initial temperature was 273.15K with thermal baths at 333.15K, and T_0 =273.15K giving a ΔT of 60K [156]. Experiments on the BC used this setup, and the method from Han et al. [159], to give Fig. 2-11. Fig. 2-12 compares the normalized temperature deviation of the simulated and experimental BCs. They show good agreement, with only a slight discrepancy near the system's boundaries. This comes from a slightly

[7] The BC is particularly interesting as it was derived without relying upon transformation media methods.

Layer	Thickness [mm]	κ [W/m·K]	ρ [kg/m^3]	c_p [J/kg·K]
Background	N/A	$\kappa_0 = 2.3$	$\rho_0 = 2000$	$c_{p0} = 1500$
Outer Layer	$b = 12$	$\kappa_1 = 9.8$	$\rho_1 = 8440$	$c_{p1} = 400$
Inner Layer	$r_2 = 9.5$	$\kappa_2 = 0.03$	$\rho_2 = 50$	$c_{p1} = 1300$
Center	$a = 6$	$\kappa_3 = 205$	$\rho_3 = 2700$	$c_{p3} = 900$

Table 2.2: Parameters of the BC used in simulations and experiments. From Sklan et al. [156].

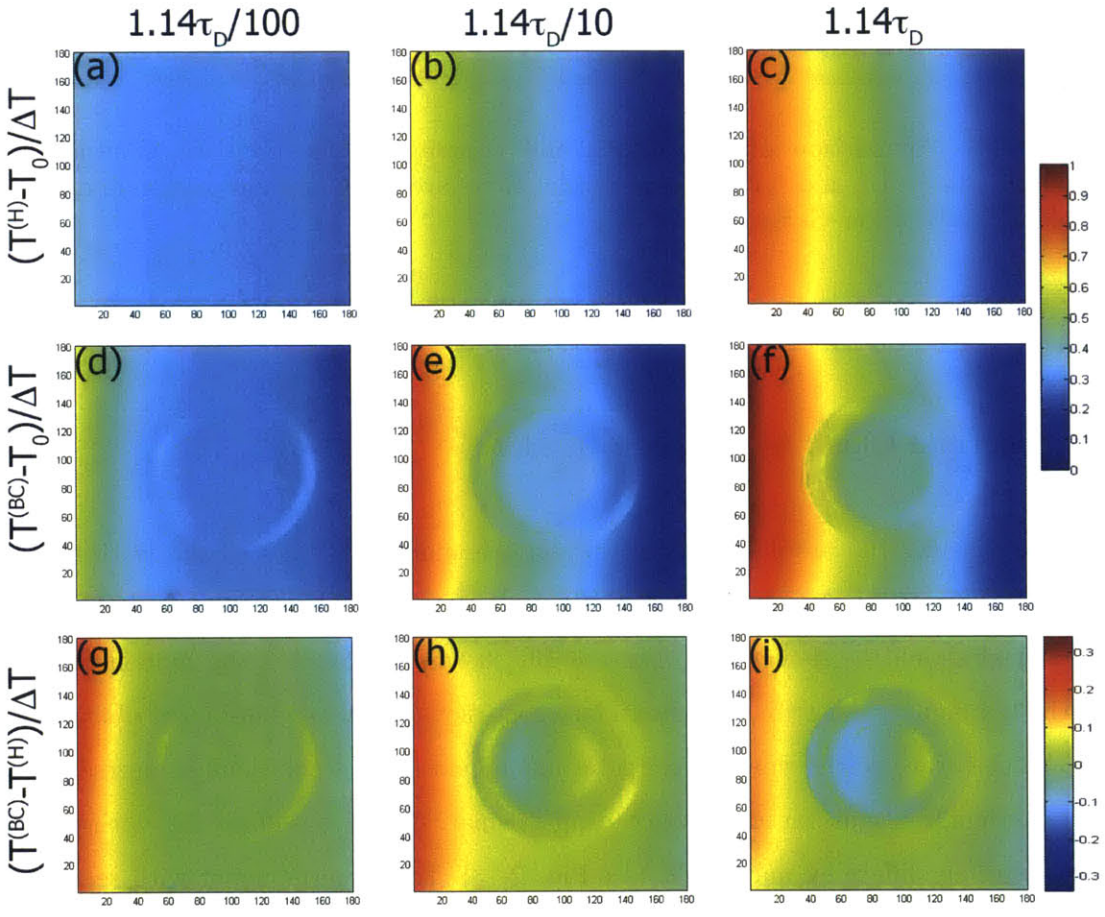

Figure 2-11: Measured temperature in the BC. Columns denote 30s ($1.14\tau_D/100$), 300s ($1.14\tau_D/10$), and 3000s ($1.14\tau_D$) respectively. Rows denote the homogeneous case (no cloak), BC, and $T^{(BC)} - T^{(H)}$. Color denotes temperature. From Sklan et al. [156].

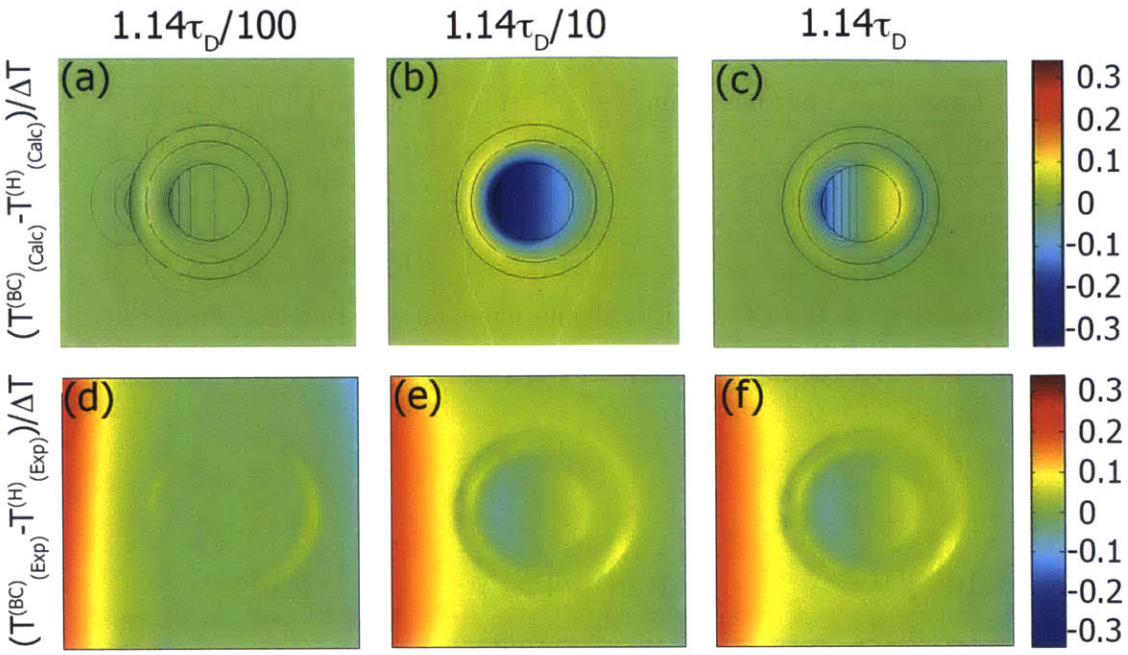

Figure 2-12: Comparison of simulations and experiments for the BC. Columns are $1.14\tau_D/100$, $1.14\tau_D/10$, and $1.14\tau_D$ respectively. Rows are δT for the simulation and experiment respectively. From Sklan et al. [156].

uneven heating in the experimental setup for both the BC and homogeneous cases.

2.3.7 Thermal Cloak as Thermal Insulator

Finally, we consider the problem of detecting objects hidden within a cloak. Both the PC and SSC have $\hat{r} \cdot \kappa \nabla T = 0$ at the boundary ($\kappa_r = 0$), so there no heat should be transferred and no signal should be detected [8]. For the BC, however, changing the hidden material effects the temperature distribution. Boundary conditions like those considered above mean that heat must traverse the cloak twice (entering and exiting), so the cloak is more effective in this case than in disguising its presence. In particular, simulations of the BC with varying cloaked materials differs by under0.1% (see Fig. 2-13). For a thermometer with sensitivity of 0.2K, more than a 200K gradient is required for the determination of the hidden material (whereas just detecting the BC requires a gradient of merely 3.64K).

Alternatively, one could try detecting a hidden temperature distribution, rather than a ma-

[8] Although, as in Ruan et al. [118], this is extremely sensitive to deviations of κ_r from 0 and as in Refs. [116, 117, 105] even a PC will transmit the mean value of T at the boundary

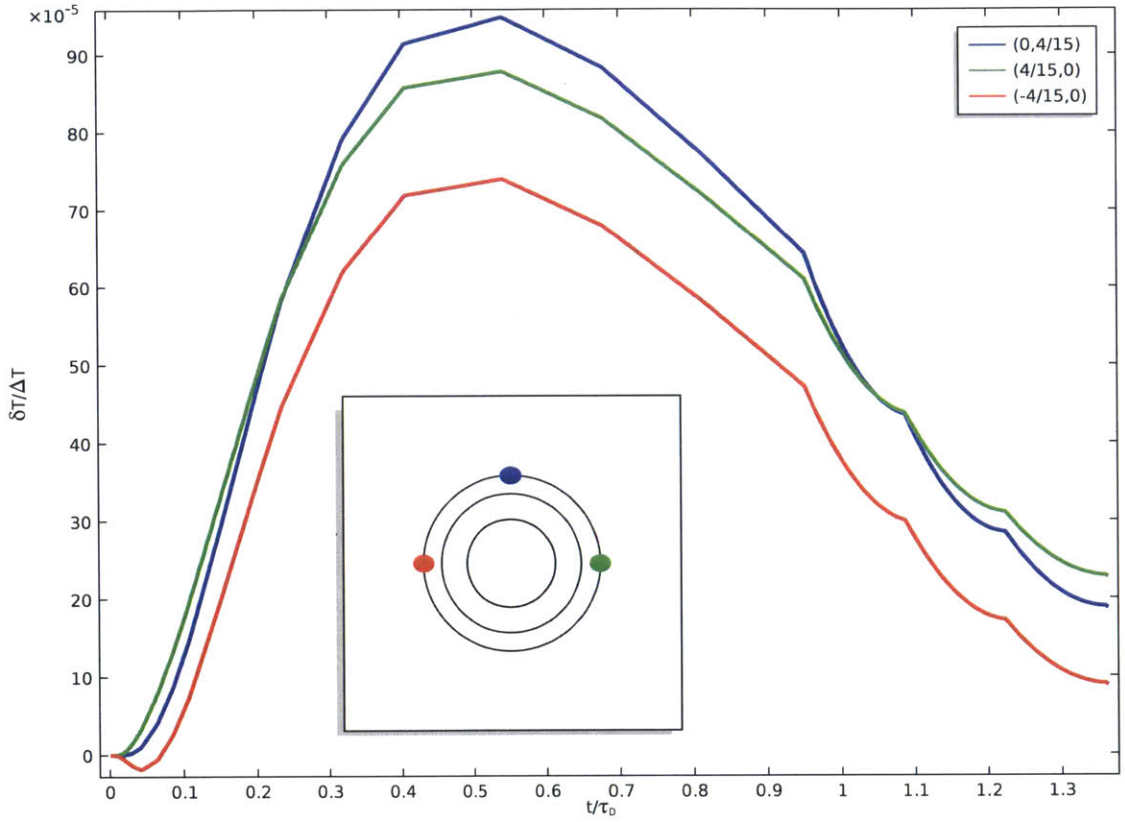

Figure 2-13: Evolution of the temperature deviation $(T^{(cloak+object)} - T^{(cloak)})/\Delta T$ for representative points external to the cloak. Color indicates the different points (see inset for key). From Sklan et al. [156].

terial. Here, initially confined heat diffuses out and only passes through the cloak once. Simulations in this case show a detectable signal of 1.5% (see Fig. 2-14), so a thermometer of similar sensitivity could detect a temperature gradient of at least 13.3K from the background. Hence, heat sources can likely be detected through the cloak, i.e. it is an imperfect insulator. Comparing the efficacy of the BC as an insulator with a thermal insulator possessing properties equal to the BC's insulating layer (basically, removing a layer) indicates that the BC is no better than a single layer insulator at suppressing this diffusion of heat into the environment. Thus, the realizable cloaks (i.e. those without a perfectly insulating inner boundary) are likely no better than conventional insulators at maintaining a temperature gradient. Moreover, even a PC [116, 117] with perfectly insulation at the inner boundary cannot prevent the matching of the average temperature inside and outside of the cloak, so the system will eventually equilibrate. For the PC, though, this would take much longer and produce a smaller leakage current, so the lack of a perfect insulating boundary increases detectability of an internal temperature distribution.

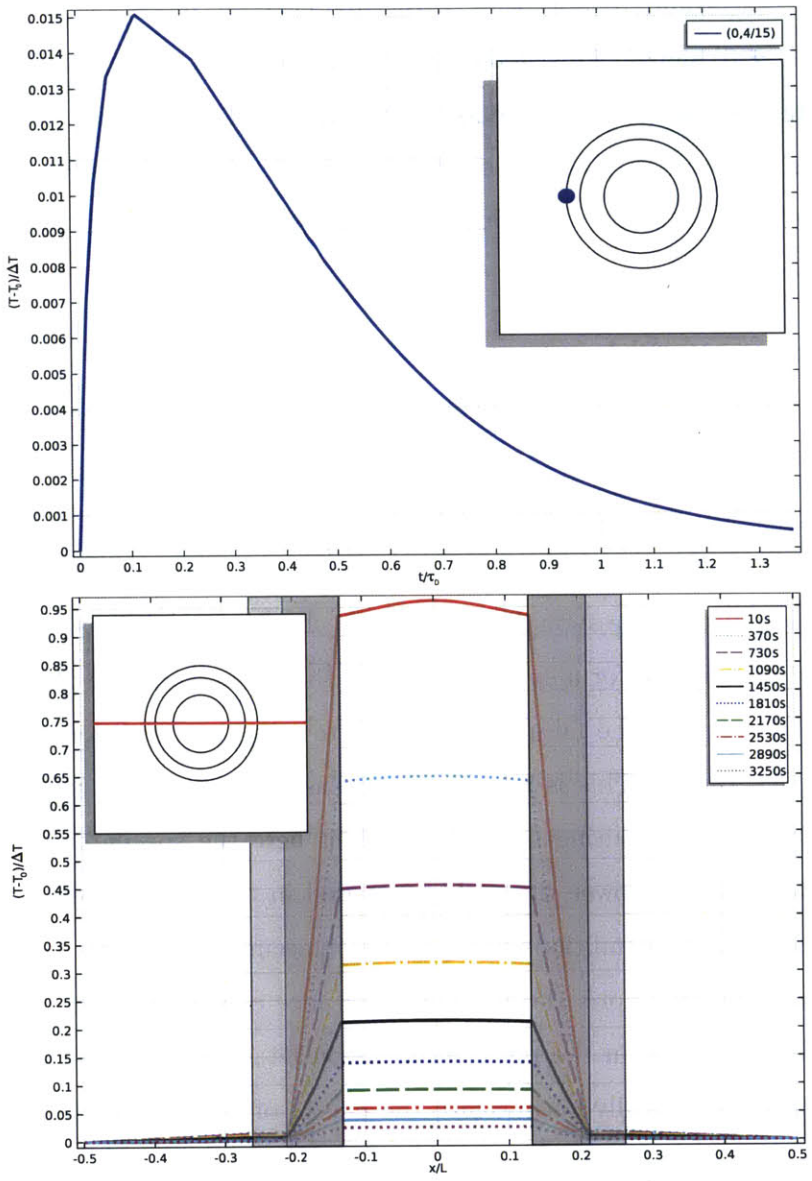

Figure 2-14: Temperature response of the BC used as an insulator. Plot (a) shows the time dependence of a representative point outside the cloak while plot (b) shows the spatial dependence of a slice through the cloak (see inset) at various times (in seconds). The fluctuation near the inner boundary is a numerical artifact of the discontinuity in temperature. From Sklan et al. [156].

2.4 Thermal Cloaking Conclusions

As we have seen, the standard approach to thermal cloaking renders the cloak detectable via a transient ($\omega \neq 0$) signal. This signal is due to neglecting the needed inhomogeneity of the volumetric heat capacity. Unfortunately, the range of values of ρc_p found in nature is quite limited, as it relates to the number of degrees of freedom possessed by the material. This means that perfect thermal cloaking is unlikely to be realizable even in the case of a perfectly engineered steady state cloak.

In the context of tuning, the behavior of the steady state cloak reveals several interesting aspects. It clearly fails because it cannot adapt to changing conditions. However, the prescription for an adaptive cloak that works at all frequencies is not a tunable material but an inhomogeneous one. Tunability, such as was discussed in Ch. 2.1 is an important tool but it is not the only issue for regulating transport. Tuning tends to be important when the operation of a device should change under changing conditions. In the context of cloaking, that is prescription for a space-time cloak [133]. In the failure of the steady state cloak, however, we also see the failure of a device to adapt to conditions varying beyond a specific frequency range. This is the same issue as is found in the use of non-tunable devices to circumstances requiring tunability (albeit here the specific frequency range is $\omega = 0$, much lower and narrower than what is found in tunable devices). A device that fails to adapt to changing conditions will produce inaccurate responses such as revealing a cloak's presence. Furthermore, devices will often face constraints that imply that they cannot perform perfectly, as in the physical limits on ρc_p. For both spatial and temporal tuning, the solution is typically to mitigate the effects of these errors (e.g. reducing the effective scattering strength Ka) or working around the problem (e.g. using multiple signals to tune a device [92, 93, 95, 96, 97, 98, 99]). Exploiting the thermal tunability of ρc_p and κ therefore offers the potential for restoring the operation of a thermal cloak, albeit a challenging one.

Chapter 3

Resonant Tuning

In Ch. 1, we showed that driving a system at or near its resonant frequency results in qualitatively different behavior than driving it far from the resonant frequency. In particular, at the resonant frequency an infinitesimal driving force can produce a finite response. For an energy band, when a tuning signal results in a resonant coupling, a qualitatively distinct phenomenon again occurs. Since the driving signal is producing waves at the same frequency as some phonon mode, these modes can hybridize, resulting in avoided crossings in the band structure and a modification of the phonon spectrum. Because this hybridization is controlled by the tuning signal, the location of the resonance may itself be tunable. In this chapter, we shall examine some forms of phonon resonance and how they have been used to various ends. We will then consider the question of whether information in phonons is accessible, and if so is it possible to construct phononic information processing elements or a phononic computer. Finally, we will combine these two threads by using resonant couplings to design a new class of phononic computers, one with some unusual properties.

3.1 Overview of Resonant Tuning Techniques

To illustrate the effects of mode mixing, we follow an example given in Deymier [7]. Consider a pair of one-dimensional harmonic oscillator chains coupled in the following manner

$$m_1\ddot{u}_i = K_1\left(u_{i+1} - 2u_i + u_{i-1}\right) + K_C\left(v_i - u_i\right) \tag{3.1a}$$

$$m_2\ddot{v}_i = K_1\left(v_{i+1} - 2v_i + v_{i-1}\right) - K_C\left(v_i - u_i\right) \tag{3.1b}$$

where v refers to the displacement of the second chain and k_C is the coupling constant (all other parameters defined from equation 1.1). Assuming solutions of the form $u_n = u_0 e^{i\omega t + ikna} = u_0 * v_n/v_0$ gives the matrix equation

$$\det\begin{bmatrix} 4K_1\sin^2\frac{ka}{2} + K_C - m_1\omega^2 & -K_C \\ -K_C & 4K_2\sin^2\frac{ka}{2} + K_C - m_2\omega^2 \end{bmatrix} = 0 \tag{3.2}$$

which can be solved to give (setting our unit of ω to $\sqrt{K_1/m_1}$, m to m_1, and K to K_1, so that we define $m = m_2/m_1$ and $\omega_2 = \sqrt{K_2/m_2}$)

$$\begin{aligned}\omega^2 &= (1+\frac{1}{m})\frac{K_C}{2} + 2(1+\omega_2^2)\sin^2\frac{ka}{2} \\ &\pm \sqrt{4(1-\omega_2^2)^2\sin^4\frac{ka}{2} + 2(1-\frac{1}{m})(1-\omega_2^2)K_C\sin^2\frac{ka}{2} + (1+\frac{1}{m})^2(\frac{K_C}{2})^2}.\end{aligned} \tag{3.3}$$

We plot this dispersion relation for $m = 2, K_2 = K_1, K_C = 0.1$ in Fig. 3.1, where the dotted lines indicate the decoupled modes. Note that these bands, which had previously intersected at the origin, have now split into two, with a higher energy band having finite ω at $k = 0$. These modes then approach their decoupled limits for larger k. To elucidate this effect, we repeat these calculations, replacing the harmonic coupling of the second lattice ($K(u_{n+1} + u_{n-1} - 2u_n)$) with an array of decoupled oscillators ($-Ku_n$). This essentially replaces the Debye approximation of this lattice with an Einstein approximation, i.e. one where all the oscillations for a lattice occur at a fixed frequency. The new band structure is plotted in 3.1, where we again see the lifting of the phonon bands. We also see that the bending of the band structures from their decoupled limit is strongest around the point where the decoupled modes intersect. This bending is a manifestation of level repulsion and

is also referred to as mode mixing since it implies that the excitations are a hybridization of the two constituent modes. When two modes are resonant with each other (same frequency and wave vector), a small interaction between the two will break the degeneracy and bend the bands away from each other. This effect is quite general, as typically the modes need to be non-degenerate in some other conserved quantity (e.g. inversion symmetry) for a crossing to persist.

3.1.1 Optical Resonance

Surprisingly, the first class of phonon resonances discovered occurred with photons. Even though the speed of light is several orders of magnitude larger than the speed of sound, the presence of optical phonon modes with non-zero frequency at the Gamma point ($\vec{k} = 0$) means that there are still resonances to be exploited. These hybrid modes are referred to as "phonon polaritons" and were first discovered by Tolpygo [160] and Fano [161]. The coupling here arises because the crystal lattice is composed of ions and so can possess a finite dipole moment. The oscillation of this polarization (or polarization wave, hence polariton) can be driven by either acoustic of optical excitation. While this gives a very strong resonance in many materials, the difference between photons and phonons does have some drawbacks. In particular, photon modes are difficult to dynamically tune (although the use of phoxonic or optomechanical devices, discussed in Sec 4.2.2 show some promise for static control). As such, controlling the optical signal has little effect on the phonon band structure, although it can be used to amplify phonon modes and produce controllable phonon [162, 163, 164, 165, 166] or phonon polariton [167] wavefronts. A fruitful approach to tuning the phonon resonance is possible, however. Rather than tuning the resonance through varying the frequency of the optical excitation, the photon frequency is held fixed and its effective wavelength is modulated. This was done by Katayama et al. [168], who placed a transmission grating between the light source and the material, then varied its position to control the wavelength of excited phonon polaritons (which have wavelengths equal to the light intensity pattern projected onto the material) and thereby tune the location of the phonon resonance. Poolman et al. [169], on the other hand, used acoustic phonons to tune phonon polaritons. Specifically, they used the Autler-Townes effect to induce resonant gaps in the polariton spectrum. This occurs because the acoustic phonons are anharmonic, creating an effective

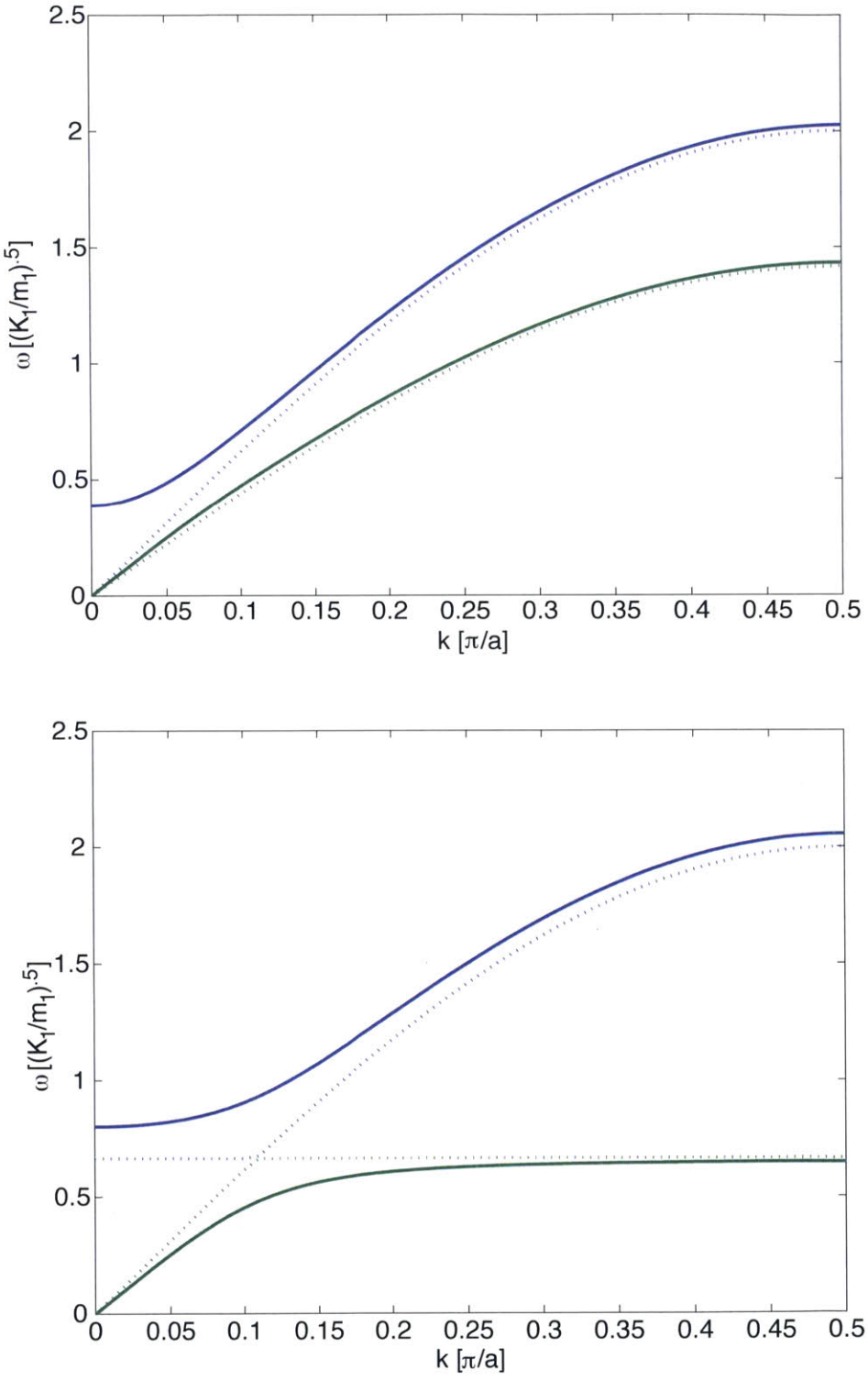

Figure 3-1: Mode mixing and level repulsion in two degenerate modes. Dotted lines indicate uncoupled modes. In (a) the modes are a pair of acoustic waves while in (b) it is an acoustic mode and a resonator of fixed frequency.

grating that can scatter polaritons. As the intensity of the acoustic phonons increases, this can lead to the generation of higher frequency phonons from anharmonic combination of acoustic phonons or the parametric driving of the lattice grating. This means that the phonon intensity becomes a parameter that can tune the location of the resonant band gaps, changing the location of the polariton resonance and therefore the frequency of the photons radiated from the system (Poolman et al. were specifically interested in using this technique for generating THz photons). Recently, a new approach to polariton tuning was developed that exploits the existence of multiple polariton modes. There also exist plasmon polariton modes. These plasmon polaritons are the result of electronic charge density oscillations producing a wave of varying polarization, and these plasmon polaritons can couple to the phonon polaritons. Brar et al. [170] showed that plasmons and phonons can hybridize, which was applied to polaritons by Kumar et al. [171] and Dai et al. [172] (with later additions by Sun et al. [173] and Wu [174]), Since the plasmons are electronic excitations, they can easily be tuned by applying a voltage across the sample, and thereby tune the resonance between plasmon polaritons and phonon polaritons (their hybridization is termed plasmon-phonon polariton). This effect is shown in Fig. 3-2, where an applied voltage drives the band structure from (d) to (e).

3.1.2 Electric Resonances

In Ch. 2.1.4, a DC or low frequency electric field was applied to control the properties of a piezoelectric or electrorheological material. However, when working with AC or higher frequency field, the waves of alternating voltage can create resonance effects with the phonon modes. This was first exploited by Wang et al. [175] (and later improved upon by Chen et al. [176] and Casadei et al. [177]) to tune the phonon band structure via an effective, tunable Young's modulus ($E = 9\lambda G/(3\lambda + G)$ where ${c_{ijk}}^k = 3\lambda\delta_{ij}$ defines the bulk modulus and the shear modulus $2G\delta_{ij} = c_{ijkk} - {c_{ijk}}^k/3$). They used a phononic crystal composed of a beam with piezoelectric patches attached to inductive circuits (thereby allowing the propagation of waves of voltage oscillations). Bergamini et al. [178] show the connection between these resonances and the resonances of an LC (inductor-capacitor) circuit, as the piezoelectric itself acts as a capacitor, while Hou and Assouar [179] develop an analytic expression for the one-dimensional band structure of an LC piezoelectric phononic material. By changing

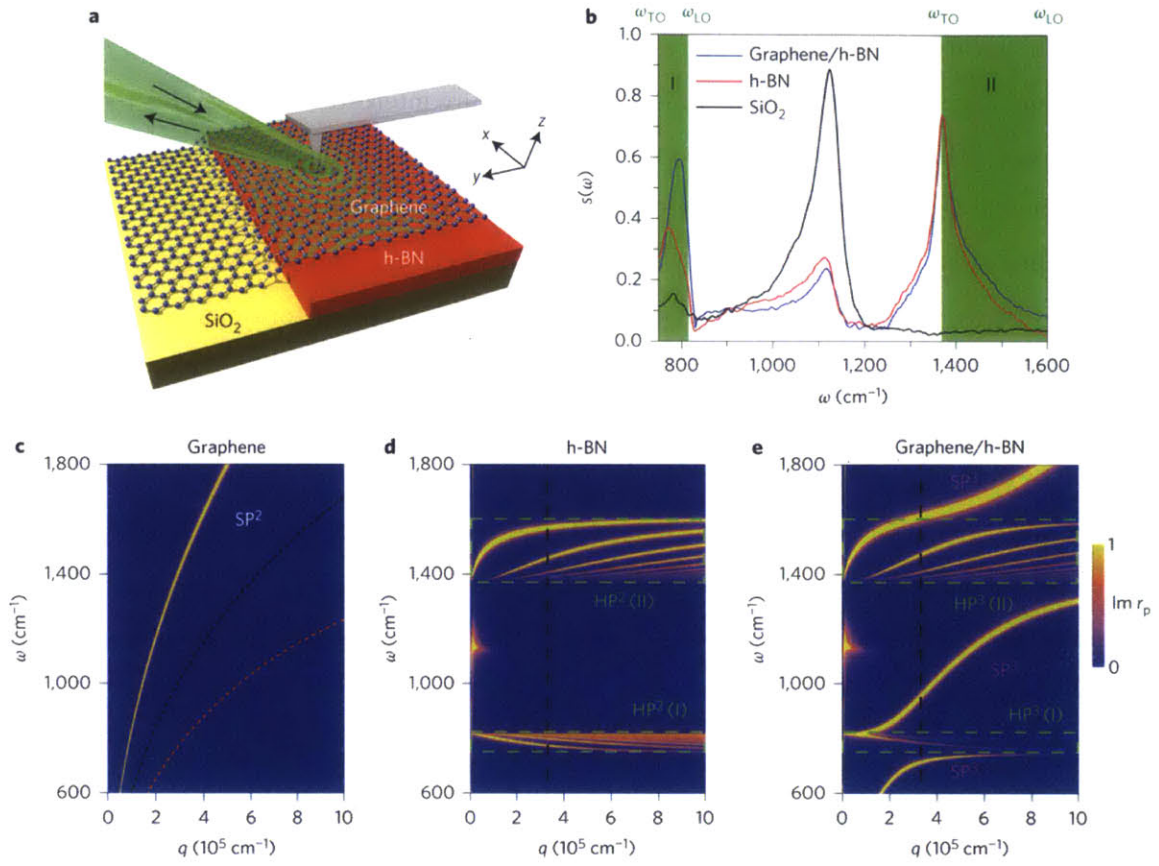

Figure 3-2: Plasmon-phonon polariton resonance tuned with electric field. (a) Experimental setup, black arrows denote infrared beams incident on and scattered from an atomic force microscope tip. (b) Measured spectra of the structure. (c) Calculated dispersion of the surface plasmon polaritons in freestanding graphene for Fermi energies 0.08, 0.15, and 0.37 eV. (d) Calculated hyperbolic phonon polaritons (HP^2) in hexagonal boron nitride (h-BN), black line is predicted to have the strongest coupling to the AFM while the green rectangles contain regions of hyperbolic bands. Isolated resonance near the origin is due to the substrate. (e) As (d) but with a Fermi energy of 0.37 eV, yielding hyperbolic plasmon-phonon polaritons (HP^3) and surface plasmon-phonon polaritons (SP^3). Figure from S. Dai, Q. Ma, M. K. Liu, T. Andersen, Z. Fei, M. D. Goldflam, M. Wagner, K. Watanabe, T. Taniguchi, M. Thiemens, F. Keilmann, G. C. A. M. Janssen, S-E. Zhu, P. Jarillo-Herrero, M. M. Fogler, D. N. Basov, *Nat. Nanotechnol.* **10**, 682-686 (2015) reprinted by permission from Macmillan Publishers Ltd: Nature Nanotechnology, copyright 2015 [172].

the frequency of these oscillations (either by changing the frequency of the applied AC voltage [175] or by changing the applied inductance/impedance [178]), the location of the phonon resonance could be tuned. This is shown in Fig. 3-3. Note the presence of the backwards bending dispersion relation in Fig. 3-3a and Fig. 3-3c. This is a generalization from Fig. 3.1 to include finite lifetimes, which turns the wave vector complex and bridges the gap with short lifetime modes. A similar effect was used in Zhou and Chen [180], where they used locally resonant phononic crystals filled with an electrorheological materials (as in Liu and Shaw [181]). These locally resonant phononic crystals are metamaterials whose structural resonances can induce phonon band gaps at much lower frequencies than the Bragg scattering phononic crystals used in Ch. 2.1. Their use of electrorheological inclusions in the locally resonant phononic crystal meant that they could tune the shear modulus of the crystal, thereby tuning the size of the band gaps. The location and number of the gaps, however, was defined by the local geometry and so was not changed by this resonant coupling. These two approaches are reviewed in Chen and Huang [182], whereas Kwon et al. [183] combine them and use an array of piezoelectric locally resonant metamaterials in a phononic crystal array with inductive shunts. Chen et al. [184] showed how such active elastic metamaterials allowed for tuning material properties in a way that satisfied the requirements of transformation acoustics (explained in Ch. 2.2). Krylov et al. [185], on the other hand, used an array of micron-scale cantilevers. The vibrations of these cantilevers was parametrically driven (explained in more detail in Ch. 4.1) by an electric field. When the field's frequency was slowly varied past the resonant frequency of the beams, they observed the sudden onset of multiple instabilities. This changed the standing wave pattern of the cantilevers. Each of the instabilities corresponded to the onset of a new standing wave pattern with a different wavelength.

In addition to using electric fields in isolation to tune electron-phonon resonances, there has also been work on the effects of static magnetic fields and varying electric fields. This was principally done for strong magnetic fields on graphene, where the magnetic field creates Landau levels. Changing the electric field changes the Fermi level, and thereby the occupancy of the highest occupied Landau level. Filling the highest Landau level can block electronic transitions. These transitions can resonate with the phonon modes, giving rise to an effect termed magneto-phonon resonance. As such, tuning the Fermi level can have strong

effects on the magneto-phonon resonance, as demonstrated theoretically in Ando [193] and experimentally in Leszczynski et al. [194].

3.1.3 Magnetic Resonance

The investigation of resonant effects between magnetic fields and phonons has necessarily relied upon indirect couplings. Phonons, being much more massive than electrons and having their ionic charges screened by the surrounding electrons, have only very weak direct couplings to applied magnetic fields. Hence, the first proposed magnetic resonance effect was for spin waves in ferromagnetic crystals, i.e. a magneto-acoustic effect. The resonant aspects of this were proposed by Kittel [195], although phenomenological work for these systems was simultaneously developed by Vlasov [196]. These effects relied upon the existence of magnons (spin waves) in magnetic materials. These magnons can resonantly couple to phonons. Moreover, the magnon modes can be shifted by means of an applied magnetic field (which gives them a finite frequency at $k = 0$), thereby shifting the location of the magnon-phonon resonance. Unlike the other couplings described in this section, magnon resonance has not been used to tune band structures. Magnon coupling is found in other contexts. Early experimental tests of this resonance were done in yttrium iron garnet (YIG), a ferrimagnet, for example Matthews and LeCraw [197]. Furthermore, these resonances have been observed in antiferromagnets (as in Boiteux et al. [198] and Turov [199]) or molecular paramagnets (Kochelaev [200], Tucker [201], and Tokman et al. [202]). On the phonon side, all of the resonances considered here were for acoustic phonons, while Sytcheva et al. [203] observed an anomalous form of phonon resonance which Thalmeier [204] argued was indicative of phonon resonance from an optical phonon. Ando [205], meanwhile, considered optical phonons in graphene, which can couple to electronic transitions between Landau levels in strong magnetic fields (i.e. magneto-phonon resonance). Paramagnetic materials, in contrast with magnetically ordered materials (ferromagnets, antiferromagnets, ferrimagnets, etc.), do not possess well-defined magnon modes. Instead, the resonances that arise in paramagnets are due to couplings to field polarized electron spins [202], electronic orbital angular momentum [204], or electronic orbital transitions [205]. In addition to these couplings, though, there have been additional phonon resonances observed in nonmagnetic materials due to the existence of narrow ranges where electromagnetic waves can propagate

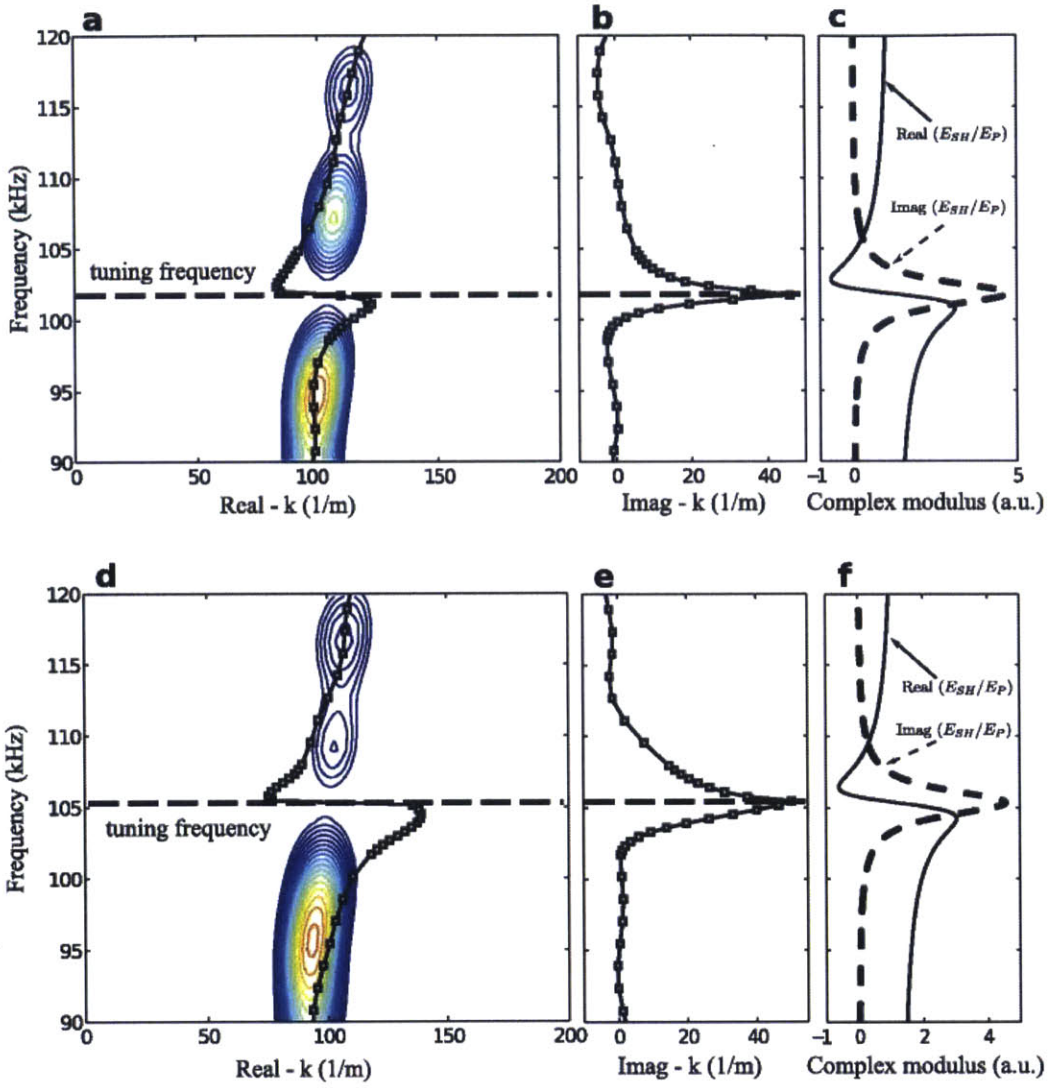

Figure 3-3: Experimentally measured piezoelectric-phonon resonance band gap. (a) Color contours are experimentally measured dispersion, while the black curve the estimate of the real part of the phonon dispersion. Backwards bending is indicative of resonance. (b) Estimated imaginary part of the wave vector. (c) real and imaginary part of the Young's modulus. (d)-(f) same as (a)-(c) but with inductance shifted from $L = 1890\mu H$ to $1560\mu H$. From Reprinted with permission from F. Casadei, T. Delpero, A. Bergamini, P. Ermanni, and M. Ruzzene, *J. Appl. Phys.* **112**, 064902 (2012). Copyright 2015, AIP Publishing LLC [177].

unimpeded. These can arise from Doppler-shifted cyclotron resonance (that is, the rotational motion of electrons around extrema of the Fermi surface can permit the propagation of photons within a Doppler-shift sized window of its frequency, see Mertsching [206] for a review) [207], helicons (circularly polarized photons propagating through uncompensated metals, see Petrashov [208] for a review) [209], and dopplerons (the same, but for compensated metals [210]) [211, 212]. These effects are summarized in Gudkov and Gavenda [213].

3.1.4 Phonon-Phonon Resonance

The exploitation of phonon anharmonicity to control phonon transport properties is distinct from other forms of resonant tuning. This is because this effect is strongest in highly anharmonic materials, i.e. ones where the simple phonon band picture is less applicable. In this regime, harmonic phonon signals will induce additional components at other frequencies, resulting in a wave packet containing many different frequency components. As such, it makes more sense to speak of phonon transmission properties here than to define phonon band structures. This is the approach taken by Li et al. [190], where they use a granular phononic crystal driven by a frequency ω_o above the cutoff of the acoustic band. While this frequency would normally be blocked, they add a second signal ω_c below the cutoff, where the anharmonicity induces additional frequencies of the form $n\omega_o \pm m\omega_c$ (n, m integers). Since some of these signals are below the cutoff, they can propagate. While they propagate they will also interact again with the control signal, generating frequencies inside the band gap. This includes the original signal at ω_o, and so the signal within the band gap can propagate. Similar techniques exist for nanoelectromechanical resonators, anharmonic fluids, and helicoidal phononic crystals (Hatanaka et al. [186, 187], Campos-Pozuelo [188] and Liang et al. [189], and Li et al. [191], respectively). While these are not, strictly speaking, resonant effects (ω_c is necessarily different from ω_o), this approach leads to a purely phononic resonant switch. Ganesh and Gonella [192] drive a granular phononic crystal at a single frequency in the lowest acoustic band. Because of the material's anharmonicity, as they increase the amplitude of the phonon current additional modes at integer multiples of the original frequency are produced. Since these frequencies are in other branches (higher acoustic branches or optical branches), they can have very different properties even at the same wave

vector. In particular, their group velocities can have different magnitude and direction. This allows them to tune the angular distribution of the transmitted waves, as well as to make the low frequency phonons take on properties associated with higher frequency modes (such as the direction of polarization and form of the displacement). This last effect is illustrated in Fig. 3-4c,d

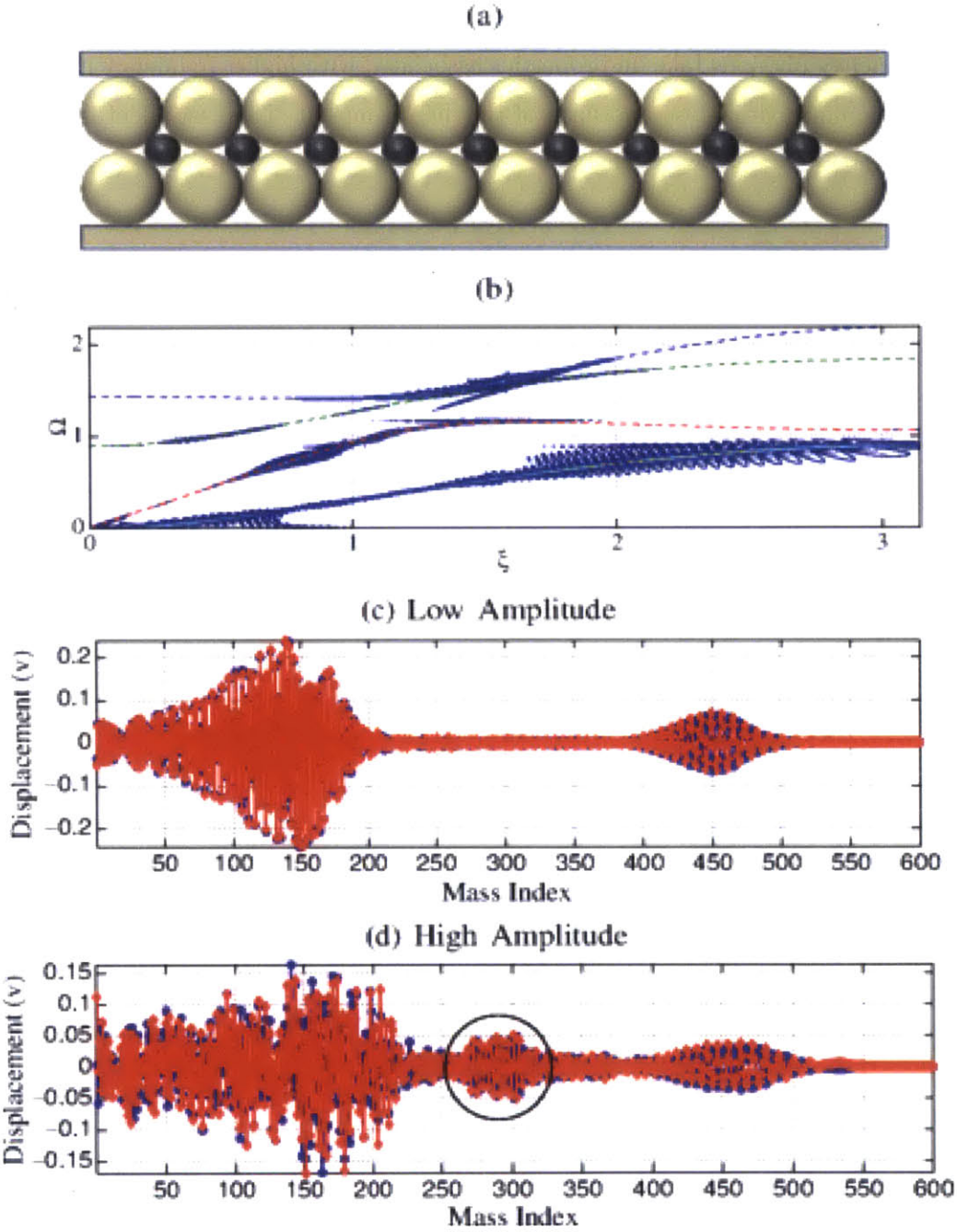

Figure 3-4: Mode mixing due to phonon-phonon resonance. (a) The granular phononic crystal structure. (b) High amplitude, anharmonic phonon modes' occupation distribution (colored contours) superimposed over the linear phonon spectrum (dotted lines). (c,d) Phonon displacement profile vs. site index (labeled "mass index") for (c) low amplitude phonons and (d) high amplitude phonons. The additional deformation component is circled. Reprinted figure with permission from R. Ganesh and S. Gonella, *Phys. Rev. Lett.* **114**, 054302 (2015). Copyright 2015 by the American Physical Society [192].

3.2 Phonon Computing

In Ch. 2.3 we considered the problem of detecting a thermal cloak. This was done by applying a temperature profile and then analyzing the heat current that was scattered back. Depending upon where the heat current had been inside of the cloak we could learn different things. In particular, currents that penetrated the inner boundary of the cloak would contain information about the nature of the cloaked object, while currents that merely scattered off the outer boundary of the cloak did no more than disclose the location and existence of the cloak. Thus we see that heat currents can transport information. Given that this is the case, the possibility of information processing with heat seems a natural extension. Some work has been done on this [2], particularly on the heat carrier-agnostic approach (reviewed by Li et al. [1]) that only considers temperature profiles. Here, however, we shall take a narrower approach and just review aspects of phonon computing that address phonon transport directly (both these topics and some related ones like quantum phononic computers are reviewed in Sklan [2]). We will also postpone a discussion of optomechanical phonon computers to Ch. 4.2.2, as they use light of higher frequency than phonons and are therefore a high frequency phenomenon.

The idea of using vibrations for computation actually arose in the design of early forms of RAM, where acoustic waves in fluid delay lines were briefly used [214]. This approach then lay forgotten save for a lone attempt to use destructive interference of surface acoustic waves to construct logic gates in the 1970s [215]. Modern attempts at phononic computers, however, have been chiefly concerned with the creation of diodes (i.e. to allow a current to pass in one direction but not the reverse). This remains a controversial topic, as the majority of these diodes do not violate reciprocity and so do not meet the strictest criteria for a diode [216]. Reciprocity here means that, if we send some arbitrary signal through a generic system and allow it to scatter, the time-reversed scattered signal will reproduce the original input. It is possible to break reciprocity by breaking time-reversal symmetry, or more weakly by adding nonlinearity (whether nonlinear phononic diodes meet the criteria for being a diode remains particularly contentious). However, as these approaches can be difficult, it is often easier to break some spatial symmetry (normally parity symmetry), which means that the signal used for the "reverse" configuration passes through a different

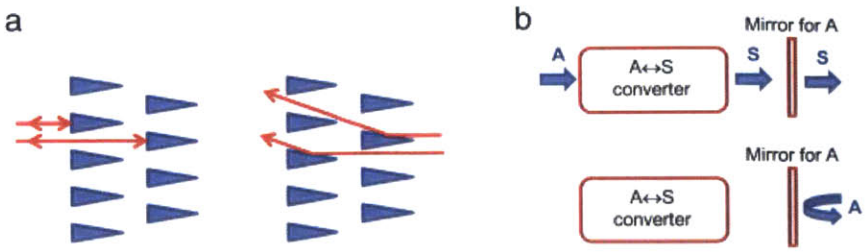

Figure 3-5: Proposed phonon diode designs. (a) An array of triangular scatterers. (b) Mode converting diode. Converts an antisymmetric plate mode (A) into a symmetric mode (S) and a selective mirror with high reflectivity for the A mode and high transmission for the S mode. Reprinted from *Wave Motion*, **50**, A. A. Maznev, A. G. Every, and O. B. Wright, Reciprocity in reflection and transmission: What is a 'phonon diode'?, 776-784, Copyright (2013), with permission from Elsevier [216].

channel than the output signal in the "forward" configuration. For example, in Fig. 3-5a, the signal transmitted by the triangular scatterers leaves at an angle while the inputs in both configurations approach head on.

3.2.1 Parity-Breaking Phononic Diodes

Essentially the basic approach to constructing parity break phononic diodes is, as laid out in Fig. 3-5, to use some asymmetric scattering to guide the transport of two "dual" signals. Triangular scatters [217] are a common approach, as the resultant bottleneck is rather intuitive and rectification (preferential flow) can be experimentally confirmed in real-time as demonstrated by Danworaphong et al. [218] for surface acoustic waves (SAW) in porous silicon and Alagoz [219] for sound in air with wooden rods. In analogy to triangular scatters, there is the use of asymmetric surface roughness in layered media. Sun et al. [220] and Jia et al. [221] both use this approach layers of textured steel planes in water. Specifically, the planes are smooth on one side and have periodic rectangular bumps on the other. The textured side converts incident waves into modes that can propagate through the steel plate, while the smooth side does not. Texturing need not be attached to the layer (see Fig. 3-6b), as shown by Sun and Zhang [222] with a layer of spherical scatters in front of a series of smooth planes. Zhu et al. [223] use a pair of phononic crystals in a wire to construct a Lamb wave rectifier. One phononic crystal is a one-dimensional antisymmetric array (top-bottom-top) while the other is a symmetric array. Antisymmetric waves incident upon the antisymmetric grating hybridize and create symmetric excitations; whereas the symmetric grating blocks

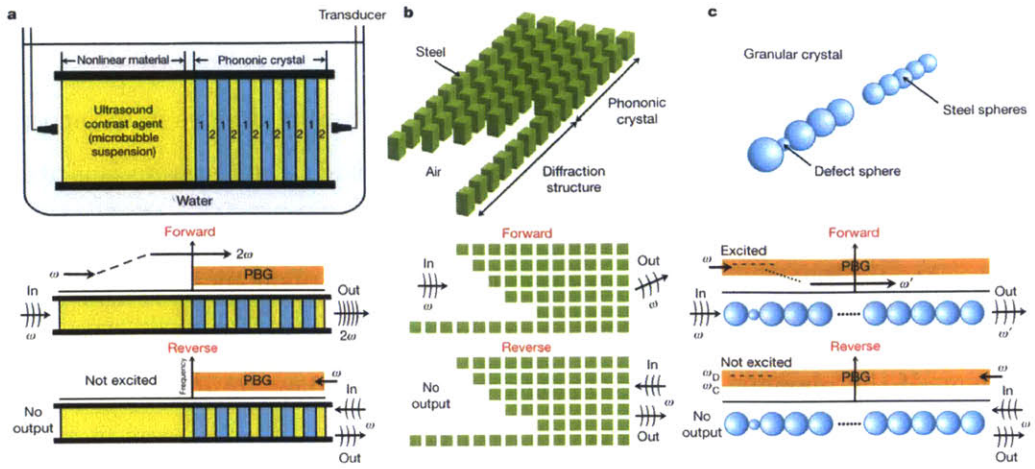

Figure 3-6: Acoustic Diodes. (A) Nonlinear diode using a nonlinear medium and phononic crystal filter. As in Liang et al. [230]. (B) Linear diode using asymmetric scattering, as in Sun et al. [220]. (C) Nonlinear diode using a nonlinear granular lattice, with defect serving as mode conversion and lattice serving as filter. As in Boechler et al. [42]. Figure from M. Maldovan, Nature 503, 209-217 (2013) reprinted by permission from Macmillan Publishers Ltd: Nature, copyright 2013 [224].

asymmetric waves but transmits symmetric waves. Changing the stress loading on the rod, these transmission characteristics can be changed to swap the roles of the symmetric and antisymmetric modes.

Phonon scattering in phononic crystals creates other avenues for rectification. Yuan et al. [228], study a phononic crystal inside a bent waveguide. The phononic crystal is designed to have a partial band gap along the ΓX direction of the Brillouin zone but not the ΓM direction. Hence, waves incident normal to the phononic crystal are blocked by the partial band gap and waves incident along the bent segment of the waveguide lie within the partial band gap. Another method of angle-dependent phononic crystal rectification was developed by Cicek et al. [229] for a pair of phononic crystals. The phononic crystals are designed to have very different Brillouin zones and are oriented along different angles at the interface. Thus incident waves from each side will be at different angles and so correspond to different vectors in the Brillouin zone. In the forward configuration, the first phononic crystal rescales the phonon wave vector without altering its direction. This wave vector is refracted in the second phononic crystal to produce a transmitted signal at a new angle [1]. In the reverse direction, though, waves incident on the second phononic crystal are blocked by a partial

[1] And another transmitted signal with k vector separated by a reciprocal lattice vector from the primary transmission peak

band gap.

A popular approach to breaking reciprocity with these scattering designs is to incorporate nonlinear elements. Liang et al. [230] is typical of this method. Their system is a phononic crystal superlattice (layers of water and glass) connected to a nonlinear fluid medium (see Fig. 3-6a). At the frequency of the incident phonons, the phononic crystal has a gap. In the nonlinear medium, however, phonons at this frequency also excite modes at twice the frequency. If the phonons hit the phononic crystal first, they are damped and cannot excite this anharmonic frequency doubling. On the other hand, if the phonons hit the nonlinear medium first, they excite the second mode, which can then traverse the phononic crystal. The frequency dependence of this technique was studied further in Liang et al. [231], where they examined the role of the different band gaps in the phononic crystal. Liang et al. [232] experimentally confirmed this approach [2] using an ultrasound contrast agent (UCA) microbubble suspension as their nonlinear medium. These bubbles expand or contract with acoustic excitation (see Guo et al. [233]), thereby creating the nonlinearity necessary for second harmonic generation. Ma et al. [234] extend this approach to a solid one or two dimensional lattice of harmonic oscillators. In particular, they create a lattice with a particular fundamental mode in the gap and its integer multiples in an optical band. They then incorporate a nonlinear oscillator to produce a third harmonic signal, thereby creating a band of strong rectification.

Boechler et al. [42] developed another approach to nonlinear acoustic rectification. They use a one-dimensional lattice of macroscopic metal spheres with Hertzian contact, also a granular crystal. Through changing the initial compression force applied to the spheres, their stationary deformation can be changed, thereby modulating the contact force's nonlinearity. In addition, the granular crystal lattice has a band gap above a critical frequency. Incorporating a defect (a sphere with a different diameter) results in a localized mode with a frequency inside the band gap (see Fig. 3-6c). If the defect is close to an edge, it can be excited easily, at which point nonlinear effects from the rest of the lattice will down-convert the signal into propagating modes within the acoustic pass band. Conversely, driving the lattice at the defect frequency far from the defect will not excite any appreciable amplitude vibration. Thus, no down-conversion occurs and the signal cannot propagate. This system

[2] And later numerically optimized in Liang et al. [233]

also exhibits an amplitude dependent bifurcation in the forward configuration. Low amplitude driving will be insufficient for down-conversion, and so will not propagate. Merkel et al. [235] examine a three dimensional extension of this system. In addition to the role of compression, they also incorporate gravity in their treatment. Because each layer is subject to a force from the weight of the layers above it, there is an inhomogeneous compression. They experimentally and numerically observe that this yields rectification of longitudinal modes moving with or against the direction of gravity. This effect can be partially tuned through controlling the initial compression.

3.2.2 Time-reversal Breaking Diodes

Time-reversal breaking phononic diodes are clear cases of diode-like behavior that unambiguously break reciprocity. However, there are far fewer means of locally break time-reversal symmetry, being essentially limited to magnetic fields, rotational motion, and active driving. One example of such a magnetic field based system will be explored in the following section (Ch. 3.3), but the others will be explored here. Fleury et al. [236] use a rotating frame for acoustic waves in air. Rotation is produced using a fan inside a circular chamber that is then linked up to three equally spaced channels. Waves entering one channel will travel along both the clockwise and counterclockwise paths to reach the exits. The phase difference between the clockwise and counterclockwise components at each exit can be tuned through fan speed, thereby tuning the transmission through each exit. This is because waves moving with or against the direction of rotation effectively experience Doppler shifts to frequency $\omega \pm \omega_{Cor}$. They numerically (see Fig. 3-7) and experimentally observe that the rotation speed can be optimized, to eliminate transmission through one exit (say, channel 1 to 3) and enhanced transmission through the other (say, channel 1 to channel 2). Permutations of the incident phonon channel results in a similar operation.

Zanjani et al. [237] study a plate acoustic waveguide incorporating a modulation domain. Within this modulation domain, the material parameters (e.g. stiffness, density) are spatially and temporally modulated via a traveling wave [3]. Phonons of the appropriate frequency propagating with the modulation wave will be converted to a new mode, while

[3]This temporal modulation breaks time reversal symmetry

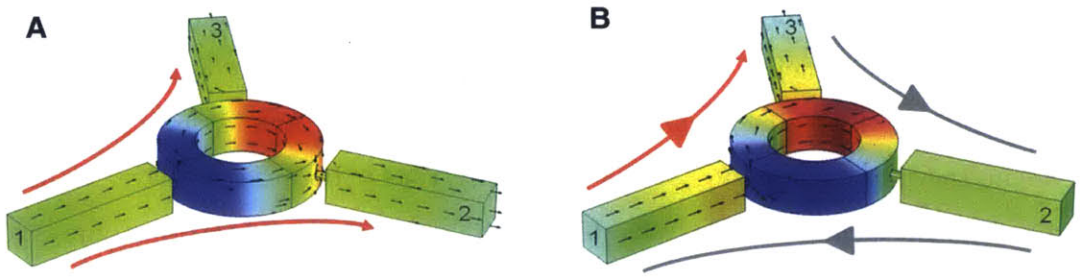

Figure 3-7: Rotational rectification. (A) When the ring is stationary, signals propagate symmetrically through each branch. (B) When the ring rotates, the broken symmetry blocks transmission along one branch. Figure from R. Fleury, D. L. Sounas, C. F. Sieck, M. R. Haberman, and A. Alù Science 343, 516 (2014). Reprinted with permission from AAAS [236].

phonons propagating against the modulation wave will not. Upon isolating the direction of propagation in this way, filtering allows the selective passage of only one direction of phonons.

Finally, Popa and Cummer [238] consider a metamaterial composed of a piezoelectric membrane sandwiched between two asymmetric Helmholtz resonator cavities. The asymmetry of the cavities means that they transmit different frequency modes. The piezoelectric is attached to a nonlinear electronic circuit that takes the measured signal from the desired direction and converts it into the signal needed to pass through the other cavity. Signals from the opposite direction, however, are filtered out by the resonator and the electronics.

3.2.3 Phononic Transistors

Phononic transistors are devices that make the transmission of one phonon current dependent upon the state of another. Their operation is less controversial than that of phononic diodes and they can be divided into two classes: direct (where the tuning of phonon transmission is due to phonon-phonon coupling) and indirect (where the tuning is mediated through some other signal). The former are essentially examples of phonon-phonon resonance, which we reviewed in Ch. 3.1.4. The latter are also closely related to the technology of phononic switches, where the transmission of phonons is contingent upon another (non-phononic) signal. The tuning techniques considered throughout this text are often used in the operation of phononic switches, as the control of phonon velocity, amplitude, and phase are the most

basic aspects of phononic transistors. Not every switch design is a transistor, though, since it is also necessary that the phonon modes can be converted into some means of controlling the other signal. The problem of phonon transduction (e.g. piezoelectric effects, optomechanics) will not be considered here, however, as there most common forms are already considered in the context of tuning.

3.2.4 Phononic Logic

The first phononic logic gates used destructive interference. As mentioned earlier, this field was initiated by Owens and Sallee [215] for surface acoustic waves. For example, a NOT gate used two signals traversing a piezoelectric. The first signal was a predefined clock signal, the other carried information. When this second signal was applied, it would necessarily be completely out of phase with the clock, resulting in destructive interference that would prevent the transmission of either signal. Withholding this signal, on the other hand, allowed the clock signal to be transmitted. NAND and OR gates were created in a similar manner by allowing additional clock signals and inputs. Masmanidas et al. [239] independently hit upon this approach many years later in a somewhat more limited fashion. They used a pair of orthogonal NEM (nanoelectromechanical) cantilevers where the cantilevers were driven by out of phase AC currents. If either current were applied in isolation, then the cantilevers would oscillate. However, if both or neither current were applied then there would be no oscillation. Thus they constructed an XOR gate but did not seek to develop other logic gates. It was not until Bringuier et al. [240] that the approach of Owens and Sallee [215] was fully updated. Since they used a phononic crystal, periodicity gave them more flexibility in constructing destructive interference. If two waves differ by a reciprocal lattice vector, then even if they are at different angles they can be mapped onto the same point in the Brillouin zone. This can be exploited to control the phase each wave will gain while traversing the phononic crystal. Upon leaving the phononic crystal, the two waves will again diverge and so the transmitted beam will split. However, the wavefronts of these beams will still overlap, and so there will be destructive interference at along a family of hyperboloids. Placing a detector at a location of destructive interference allows the logic gates to work in much the same way as before. For each logical input there will be a pair of signals – one containing information and one fixed reference (a generalization of Owen and Sallee's

clock signal). Again, like Owens and Sallee [215], the application of the information-bearing signal will induce destructive interference at the detector, such as in a NOT gate (shown in Fig. 3-8). With two distinct logical inputs and two in phase reference signals, the resultant device is a NAND gate. With two distinct logical inputs and two out of phase reference signals, the resultant device is an XOR gate. Using NAND and NOT gates, de Morgan's laws show that it is possible to construct any arbitrary classical logic operation. In addition, using a phononic crystal allows for more flexibility in the incident angles of various inputs while simultaneously making for a more compact interference based computer.

A different approach to phononic logic comes from the supplementary materials of Boechler et al. [42]. In their main text they developed a nonlinear granular phononic crystal that could serve as a rectifier through the asymmetric placement of a defect with a localized mode in the band gap. Since this design relied upon nonlinear interactions, the amplitude of oscillations in the defect mode had to exceed some critical value. An AND gate could therefore be constructed by using a pair of phase-matched signals that are individually too weak to be transmitted but whose total amplitude exceeds the critical threshold. For an OR gate, on the other hand, they used a pair of defects in a y-shaped lattice, so that each defect could be addressed individually by a different signal. As such, having either signal exceed threshold allowed the signal to be transmitted. However, one limitation of this approach is that a NOT gate could not be constructed without the spontateous generation of oscillations when none are applied. Li et al. [190] attempted to solve this problem by designing logic gates out of granular crystal transistors, whereas Boecheler et al. [42] only considered granular crystal rectifiers. While Boechler et al. [42] required a defect, Li et al. [190] had several signals at different frequencies and used their nonlinear interactions to the induce transmission of a phonon current for a frequency inside the band gap. In this, they follow the approach Mahboob et al. [241] (discussed in the next paragraph) and used three signals of incommensurate frequency (i.e. no $f_a \neq nf_b + mf_c$ for any rational n, m). Specifically, two of the signals were of low frequency modes that fell within the acoustic band (the inputs) while the last one was a high frequency mode that fell inside the band gap (the reference). Anharmonicity allows the two low frequency modes to combine and create a high frequency mode at a distinct frequency, which can be detected as an AND operation. Anharmonic coupling of either low frequency mode with the high frequency one will allow

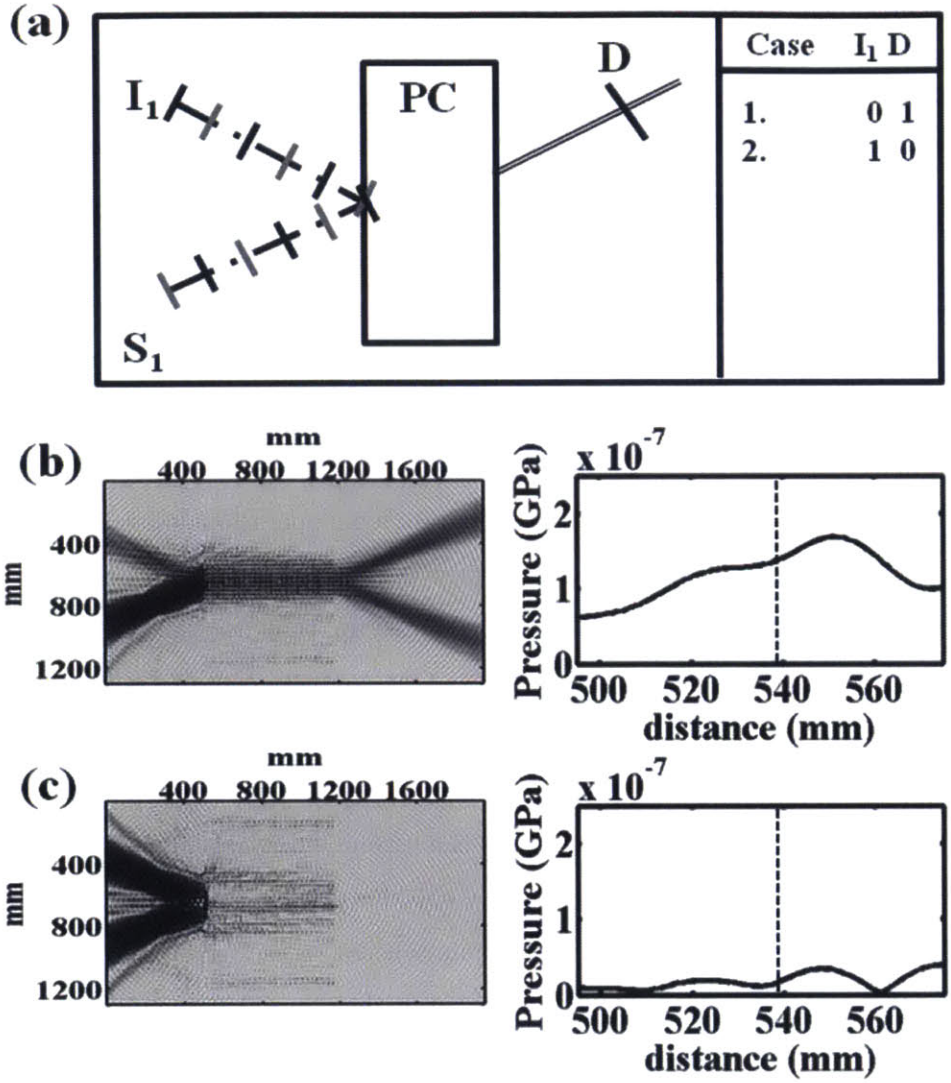

Figure 3-8: A NOT gate using destructive interference and a phononic crystal. (A) Schematic showing input signal I, reference source S, and output detector D (and a truth table of the logic operation). (B) Intensity profile predicted at D if signal I is absent. (C) Intensity profile predicted at D if signal I is present. Figure reprinted with permission from S. Bringuier, N. Swinteck, J. O. Vasseur, J.-F. Robillard, K. Runge, K. Muralidharan, and P. A. Deymier, J. Acoust. Soc. Am. 130, 4 (2011). Copyright 2011, Acoustic Society of America [240].

the high frequency mode the propagate, and so its detection is an OR operation. For a NOT gate, on the other hand, additional signals at the low frequencies are again necessary. These signals are once again out of phase with the previous ones, creating destructive interference (as in Refs. [215, 239, 240]).

Using phonons as an information carrier, due to their strong nonlinearity and wave nature, allows for interesting new avenues in nonlinear classical information processing. Mahboob et al. [241] developed one form of frequency-domain parallel computing (another is presented in Ch. 3.4.5) using an NEM resonator. This is distinct from the more common frequency domain multiplexing (i.e. the simultaneous transmission of information over multiple frequencies), as performing logic operations upon elements of a multiplexed signal remains difficult. In most cases, the signal is simply demultiplexed (say, by using a series of filters to select out different frequencies), performing separate logic operations on each of them, and then recombining them. The need to demultiplex is eliminated here however, through the exploitation of the phonon's anharmonicity. In their setup, they use a piezoelectric mechanical resonator with multiple electronic contacts. One contacts contains a two-dimensional electron gas, which they initially drive at twice the NEM resonator's fundamental frequency so as to input information (they call this driving the pump, in analogy with parametric amplification). Directly above the electron gas is a second electrical input, which is initially driven at precisely the fundamental mode (they call this driving the signal) (see Fig. 3-9a). The signal can excite a finite phonon population, whereas the pump is too weak to do so. By allowing the pump or signal input to drift from their initial frequencies, their anharmonic interaction can create excitations at new, incommensurate frequencies. The creation of different frequencies corresponds to different combinations of driving signals, which in turn allows them to distinguish the outputs of different logic operations (see Fig. 3-9b). For the resonator to act as an AND gate, two pump inputs are used at $2f_0 \pm \Delta$ (where f_0 is the resonator's fundamental mode) and a single signal is driven at $f_0 - \delta$. When these inputs interact new so-called "idler" modes are excited at the frequency differences ($f_0 \pm \Delta - \delta$) which can in turn create second order excitations at $f_0 \pm 2\Delta + \delta$. These second order idler modes will be excited only if both pump signals are applied, and as such their presence denotes an AND operation (see Fig. 3-9c). On the other hand, to create an OR gate, two signal inputs at $f_0 \pm \Delta + \delta$ are used in conjunction with the previous pump inputs. Either

pump input can now couple to its corresponding signal to excite an $f_0 - \delta$ mode, thereby denoting an OR operation. In addition, using destructive interference of the two $f_0 - \delta$ signals converts the OR operation into an XOR (see Fig. 3-9d). The authors then claim that AND, OR, and XOR allow them to create all classical logic operations, but de Morgan's laws require that there is also a NOT gate. However, if one of the inputs in the XOR gate is fixed (as in Owens and Sallee [215] and Masmanidis et al. [239]), then a NOT gate can be constructed. Since this approach relies upon each logic output having a separate, distinguishable frequency, needing to fix some frequency inputs is a drawback here. On the other hand, their method can perform all 2^{N+1} N-bit logic operations to be performed within a single circuit element. This presents a notable reduction in circuit size while increasing parallel information processing.

3.2.5 Phononic Memory

Since phonons can generally couple to other information carriers and sometimes possess longer lifetimes than they do, phononic information storage has arisen in a number of unrelated fields. A great deal of focus went into the transduction of electronic signals (and optical signals, covered in Ch. 4.2.2) to vibrations of a nanoelectromechanical (NEM) oscillator. The early work in this field generally relied upon static deformations of NEM via an electric field, such as Rueckes et al. [242] with carbon nanotube (CNT) arrays, but further development extended this to non-stationary phonon modes. Cleland and Geller [243], used a piezoelectric membrane separating two Josephson junctions to store and transform signals. Rabl et al. [244] take a similar approach to the coupling of spins separated by magnetized NEMs. Most research this field, however, has focused on classical electronics and optomechanics (Ch. 4.2.2).

Badzey et al. [245] extended Rueckes' approach [242] to a non-stationary setup. They experimentally verify that driving a CNT with an AC current makes it behave like a Duffing oscillator

$$\ddot{x} + 2\gamma\dot{x} + \omega_0^2 x \pm k_3 x^3 = F\cos\omega t. \tag{3.4}$$

The nonlinearity of a Duffing oscillator is exhibited by its bistability, as it exhibits hysteresis and jumps between two states as a function of amplitude and frequency. These

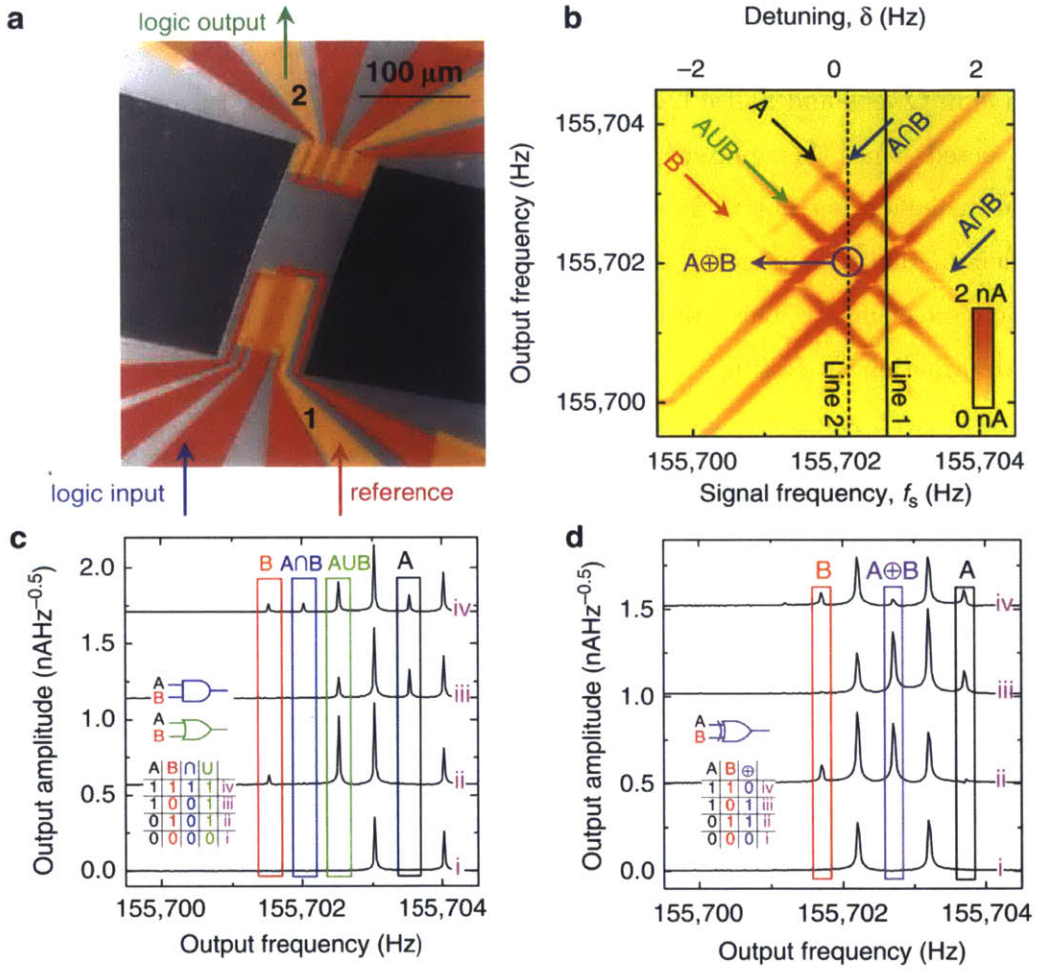

Figure 3-9: Nonlinear, frequency domain parallel computing. (A) Schematic of the NEM resonator. (B) Spectral decomposition of the resonator's logic. The two pump inputs (purple arrow in (A)) are held at fixed frequencies and form the A and B inputs, while the signal input's (red arrow in (A)) frequency f_s can vary. Lines branching off from the main diagonal denote the logic outputs (green arrow in (A)), the different interaction peaks denoting AND (blue), OR (green), and XOR (purple). (C)-(D) Output amplitude with fixed signal frequency, traversing the solid (C) and dashed (D) black lines of (B). Figure adapted from I. Mahboob, E. Flurin, K. Nishiguchi, A. Fujiwara, and H. Yamaguchi, Nat. Commun. 2, 198 (2011) reprinted by permission from Macmillan Publishers Ltd: Nature Communications, copyright 2011 [241].

jumps imply that a low amplitude, low frequency modulation can induce switching in the oscillator between its high and low amplitude states (these are maintained via a constant amplitude, high frequency driving force). Venstra et al. [246] find a similar bistable memory due to mechanical nonlinearity using microcantilevers. Khovanova and Windelen [247] used the Pontryagin control method to optimize the energy pulse needed to switch these resonators between states. Mahboob and Yamaguchi [248] took a suspended silicon nanoribbon placed between two two-dimensional electron systems to create the mechanical analog of a "parametron," which is a bistable harmonic oscillator that was proposed as a logic device in the early stages of computer development. They found that the mechanical resonant frequency could be tuned using a DC piezoelectric coupling. The NEM exhibited resonance when driven at the resonant frequency and a parametric resonance of a modulated signal at twice the resonant frequency (as expected due to parametric resonance, discussed in Ch. 4.1). Upon driving the oscillator, it has almost no displacement for driving signals below the resonant frequency (and so is monostable), large net displacement (due to buckling, which can be positive (0 phase) or negative (π phases), and so is bistable) around the resonant frequency, and tristable (0 or π phase buckling as well as no displacement) at frequencies above the resonant. Since 0 and π phases are bistable, they exhibit hysteresis and therefore can be used for reading, writing, and storage of information. They demonstrate this by using an initially monostable oscillator, selecting a phase using a weak resonant frequency biasing signal, and finally switching to the desire state (0 or 1) through applying a larger amplitude parametric actuator pulse at the parametric resonance (twice the fundamental resonance). Once the biasing pulse ends, the system retains a stable buckling, whereas when the parametric pulse ends it relaxes to the no displacement state. They extended this work in Mahboob et al. [249], where they identify additional parametric resonances. These frequencies can be individually addressed using the same algorithm to store one bit of data in the displaced oscillations of these resonances. Moreover, the information can be swapped between resonant frequencies through the anharmonic interactions between the parametric pulses.

As we have seen, phononic storage principally used acoustic resonators. The study of the acoustic properties of these systems has constituted a separate branch of study, principally as a means of evaluating the nature of phonon dissipation. There are a plethora of phonon

dissipation mechanisms, the understanding and minimizing of which are crucial to construct stable phononic memory. Direct measure of dissipation in nanoscale resonators was undertaken by Hill et al. [250]. There, they used suspended nanobeams of varying lengths as well as planar structured nanobeams (i.e. torsional rotators). Through analyzing the magnetic field and temperature dependence of the low temperature dissipation, they could differentiate between the various factors dissipation mechanisms and their relative strengths. To do this, they needed to minimize extrinsic loss mechanisms: (1) Purely mechanical effects such as clamping (that is, loss induced by the strain from a mechanical support), surface roughness, and internal dislocations. (2) Thermal effects like localized heating (particular that produced by Kapitza resistance), thermoelastic loss (strain induced local temperature gradients), and thermal expansion. (3) Phonon anharmonicity (made negligible by only using small amplitude phonons) and gas friction (obviated through working in a vacuum). This allowed them to isolate the intrinsic dissipation mechanisms. These are principally due to defects (e.g. chemical contamination or surface effects) and can take often be approximated as two level systems (transitions between localized defect states) or $D - x$ centers (where donor atoms couple to an unknown defect). In particular, they determined that the principle loss mechanism in their resonators arose from internal defect motion. In addition, they determined that while surface effects became increasingly important as they reduced system size, this could not be simply explained by a change in the surface-to-volume ratio but constituted a purely nanoscale effect. One use feature of acoustic resonators for information storage is their exceptionally large quality factors, an important measure of the resilience of the confined phonons against decay. However, these quality factors tend to reduce dramatically in smaller systems or for higher frequencies. Thus, Sun et al. [251] can find a quality factor of the order 10^3 at GHz frequencies (principally due to losses through the mechanical support of their microdisk resonator). While Goryachev et al. [252] work with a bulk acoustic wave resonator (a high quality crystal slab with curved edges to confine waves to the center of the resonator) and find a quality factor of the order 10^9 at MHz (at ultralow temperature). Finally Chakram et al. [253] studied a room temperature mesoscale resonator at MHz frequencies and found a quality factor of order 10^7 (principal losses from coupling to the mechanical support). An overview of the various loss mechanisms in a bulk acoustic wave resonator, their functional dependences, and their control was given in Goryachev et al. [254].

3.3 Methods: Magneto-acoustics

In this section we will derive the analytic expressions for the equation of motion of phonons in magneto-acoustic materials. In particular, we will consider ferromagnetic materials (the most common class of magneto-acoustic). Our derivation will initially follow the approach of Boiteux et al. [198] for antiferromagnets, i.e. a purely quantum model. We will then turn to a classical model, taken from Gudkov and Gavenda [213].

3.3.1 Quantum Model of Magneto-acoustic Interaction

To begin, let's consider the volumetric energy $\mathcal{H} = \int H dV$ of a ferromagnet in an inhomogeneous magnetic field $\vec{B} = (-B'x, -B'y, B(z))$ where $B' = dB(z)/dz$. Ignoring the electronic orbital contributions

$$H = \sum_{phonon} \hbar\omega_f(q) \left[a_f^\dagger(q)a_f(q) + \frac{1}{2}\right] + \sum_{spin} J(R_i, R_j) S_i \cdot S_j + g\mu_B \left(B' \frac{xS_x + yS_y}{2} - BS_z\right) \tag{3.5}$$

where a_f is the phonon destruction operator of mode f, $J(R_i, R_j)$ is the exchange coupling, R_i is the i^{th} lattice site's location, S is spin, g is the spin g factor, and μ_B is the Bohr magneton. Since $J(R_i, R_j)$ depends upon the locations of atoms in the lattice, it has an implicit functional dependence on phonons through the atomic displacement. Taylor expanding this in terms of ionic displacement from equilibrium gives

$$H_{spin} = \sum_{spin} J_{ij} S_i \cdot S_j + g\mu_B \left(B' \frac{xS_x + yS_y}{2} - BS_z\right) + \sum_{\alpha\beta\gamma\delta,i} G^i_{(\alpha\beta),(\gamma\delta)} S^i_\alpha S^j_\beta \epsilon^i_{\gamma\delta} \tag{3.6}$$

where J_{ij} is the equilibrium exchange coupling and G is the magnetoelastic coupling tensor [4]. Its value for different geometries is given by Dobrov [255], but for O_h group materials like

[4] Boiteux et al. [198] make a mistake in their version of this equation, which reads $S^i_\alpha S^i_\beta$.

garnets (i.e. common magneto-acoustics), it takes the form:

$$
\begin{aligned}
G &= \left[\begin{array}{ccc|ccc}
G_{1111} & G_{1122} & G_{1133} & & & \\
G_{2211} & G_{2222} & G_{2233} & & 0 & \\
G_{3311} & G_{3322} & G_{3333} & & & \\
\hline
 & & & G_{1212} & G_{1223} & G_{1213} \\
 & 0 & & G_{2312} & G_{2323} & G_{2313} \\
 & & & G_{1312} & G_{1323} & G_{1313}
\end{array}\right] \\
&= \left[\begin{array}{ccc|ccc}
 & & & & & \\
 & G_{11}\begin{bmatrix} 1 & -\frac{1}{2} & -\frac{1}{2} \\ -\frac{1}{2} & 1 & -\frac{1}{2} \\ -\frac{1}{2} & -\frac{1}{2} & 1 \end{bmatrix} & & & 0 & \\
 & & & & & \\
\hline
 & & & & & \\
 & 0 & & & G_{44}\begin{bmatrix} 1 & & \\ & 1 & \\ & & 1 \end{bmatrix} & \\
 & & & & &
\end{array}\right].
\end{aligned}
\tag{3.7}
$$

From this we rewrite our spin-phonon Hamiltonian in terms of the anticommutator operator) as

$$
\begin{aligned}
H_{sp} &= \sum \left[G_{yz,\gamma\delta}\{S_y, S_z\} + G_{xz,\gamma\delta}\{S_x, S_z\} + G_{xy,\gamma\delta}\{S_x, S_y\} + G_{xx,\gamma\delta}S_x^2 + G_{yy,\gamma\delta}S_y^2\right. \\
&+ \left. G_{zz,\gamma\delta}S_z^2\right]\epsilon_{\gamma\delta} \\
&= \sum \left[G_{23\gamma\delta}\{S_y, S_z\} + G_{13\gamma\delta}\{S_x, S_z\} + G_{12\gamma\delta}\{S_x, S_y\} + G_{11\gamma\delta}S_x^2 + G_{22\gamma\delta}S_y^2\right. \\
&+ \left. G_{33\gamma\delta}S_z^2\right]\epsilon_{\gamma\delta} \\
&= \frac{G_{44}}{2}\left[\{S_y, S_z\}\epsilon_{yz} + \{S_x, S_z\}\epsilon_{xz} + \{S_x, S_y\}\epsilon_{xy}\right] + \frac{G_{11}}{2}\left[3\left(S_x^2\epsilon_{xx} + S_y^2\epsilon_{yy} + S_z^2\epsilon_{zz}\right)\right. \\
&+ \left. -S^2{\epsilon_i}^i\right].
\end{aligned}
\tag{3.8}
$$

We now make use of the lowest order Holstein-Primakoff coordinates for magnon modes

$$
S_+^i = \sqrt{2S - \alpha_i^\dagger\alpha_i}\,\alpha_i \approx \sqrt{2S}\alpha_i \tag{3.9a}
$$

$$
S_-^i = \sqrt{2S - \alpha_i^\dagger\alpha_i}\,\alpha_i^\dagger \approx \sqrt{2S}\alpha_i^\dagger \tag{3.9b}
$$

$$
S_z^i = S - \alpha_i^\dagger\alpha_i \approx S \tag{3.9c}
$$

where $S_\pm = S_x \pm iS_y$ and α is the magnon mode destruction operator. Terms proportional to S_z^2 introduce a static magnetic energy correction to the phonon band structure but do not couple magnons to phonons to lowest order in magnon modes. This correction is typically ignored. Terms proportional to S_x^2, S_y^2, or $\{S_x, S_y\}$ are quadratic in α and therefore are also neglected to lowest order in α. Only the terms proportional to $\{S_x, S_z\}$ or $\{S_y, S_z\}$ are nontrivial and give

$$H_{sp} = \frac{G_{44}}{2}\left(\{S_y, S_z\}\epsilon_{yz} + \{S_x, S_z\}\epsilon_{xz}\right). \tag{3.10}$$

This can be Fourier transformed in Holstein-Primakoff coordinates to give

$$\begin{aligned} H &= \hbar\omega_i(q)\left(a_i^\dagger(q)a_i(q) + \frac{1}{2}\right) + \hbar\omega(q)\alpha^\dagger(q)\alpha(q) \\ &+ g\mu_B B'(z)\sqrt{\frac{S}{2}}\left(x^-(-q)\alpha(q) + x^+(-q)\alpha^\dagger(q)\right) - g\mu_B B(z)S \\ &+ A\left[\alpha^\dagger(q)\left(a_y(q) + a_y^\dagger(-q)\right) - \alpha^\dagger(-q)\left(a_y^\dagger(q) + a_y(-q)\right)\right] + h.c. \\ &+ iA\left[\alpha^\dagger(q)\left(a_x(q) + a_x^\dagger(-q)\right) - \alpha^\dagger(-q)\left(a_x^\dagger(q) + a_x(-q)\right)\right] + h.c. \end{aligned} \tag{3.11a}$$

where i is now mode index, $A = -G_{44}\sqrt{\hbar\omega S^3/Mc_s^2}$ (M is mass and c_s is speed of sound), $\hat{x}^\pm = \hat{x} \pm i\hat{y}$ is a function of the electronic orbitals [5], and h.c. is short for "Hermitian conjugate." We can now write the equation of motion for the creation and destruction operators

$$i\hbar\frac{d}{dt}\begin{vmatrix} a_+(q) \\ a_+^\dagger(\bar{q}) \\ \alpha^\dagger(\bar{q}) \\ a_-(q) \\ a_-^\dagger(\bar{q}) \\ \alpha(q) \end{vmatrix} = \begin{bmatrix} \hbar\omega_p & & -2iA & & & \\ & -\hbar\omega_p & 2iA & & & \\ -iA^* & -iA^* & -\hbar\omega_s & & & \\ & & & \hbar\omega_p & & -2iA^* \\ & & & & -\hbar\omega_p & 2iA^* \\ & & & iA & iA & \hbar\omega_s \end{bmatrix} \begin{vmatrix} a_+(q) \\ a_+^\dagger(\bar{q}) \\ \alpha^\dagger(\bar{q}) \\ a_-(q) \\ a_-^\dagger(\bar{q}) \\ \alpha(q) \end{vmatrix} \tag{3.12}$$

where $a_\pm = a_x \pm ia_y$, ω_p is the dispersion of the decoupled phonon branch (i.e. $c_s k$ to lowest order), and ω_s is the dispersion of the decoupled magnon branch (i.e. $g\mu_B B$ to lowest order).

[5] This is typically negligible compared to the magnetic contribution in ferromagnets or antiferromagnets. In paramagnets or diamagnets this couples to the electrons in partially occupied p orbitals.

This can be solved to give

$$(\hbar^2\omega^2 - \hbar\omega_p^2)(\hbar\omega \pm \hbar\omega_s) \pm 4|A|^2\hbar\omega_p = 0. \tag{3.13}$$

(Note that $|A|^2$ has a factor of ω_p). This implicitly defines the dispersion relation for the right and left circularly polarized modes. The difference between them defines gives the circular birefringence, which produces the acoustic Faraday effect.

In fact, the acoustic Faraday effect is not the most general form of the magneto-acoustic interaction, as it only arises for certain geometries. Specifically, it assumes that the phonon wave vector is oriented along the direction of magnetic field (i.e. $\hat{z}$). This geometry, we will see, gives a linear rather than a circular birefringence and is referred to as the Cotton-Mouton effect. However, to properly express the Couton-Mouton effect, and its connection with acoustic Faraday effect, we need additional terms that are more easily expressed in classical rather than quantum models of magneto-acoustics.

3.3.2 Classical Model of Magneto-acoustic Interactions

Following Gudkov and Gavenda, their most general form of linear magneto-acoustic interaction is

$$\left[\begin{array}{ccc|cc} & & & i\frac{b_2}{M_0}k_3 & \\ & M_{elast} & & & i\frac{b_2}{M_0}k_3 \\ & & & i\frac{b_2}{M_0}k_1 & i\frac{b_2}{M_0}k_2 \\ \hline & -i\gamma b_2 k_3 & -i\gamma b_2 k_2 & -i\omega & \gamma(H + \frac{2a}{M_0}k^2) \\ i\gamma b_2 k_3 & & i\gamma b_2 k_1 & -\gamma(H + \frac{2a}{M_0}k^2) & -i\omega \end{array}\right] \left|\begin{array}{c} u_1 \\ u_2 \\ u_3 \\ m_1 \\ m_2 \end{array}\right| \tag{3.14}$$

where

$$M_{elast} = \begin{bmatrix} c_{1111}k_1^2 + c_{1313}(k_2^2+k_3^2) & (c_{1122}+c_{1313})k_1k_2 & (c_{1122}+c_{1313})k_1k_3 \\ (c_{1122}+c_{1313})k_1k_2 & c_{1111}k_2^2 + c_{1313}(k_1^2+k_3^2) & (c_{1122}+c_{1313})k_2k_3 \\ (c_{1122}+c_{1313})k_1k_3 & (c_{1122}+c_{1313})k_2k_3 & c_{1111}k_3^2 + c_{1313}(k_1^2+k_2^2) \end{bmatrix} + -\rho\omega^2 \begin{bmatrix} 1 & & \\ & 1 & \\ & & 1 \end{bmatrix}, \quad (3.15)$$

$(k_1, k_2, k_3) = (k_x, k_y, k_z)$, $\gamma = g\mu_B/\hbar$ is the gyromagnetic ratio, b_2 is the magneto-acoustic constant $2G_{44}\sqrt{S^3\rho M_0/\hbar\gamma M}$ (G is the magnetoelastic constant, S is atomic spin, M_0 is net magnetization, M is phonon effective mass, ρ is density), H is the applied magnetic field, a is the magnetic exchange energy (typically neglected), M_0 is the net magnetization (assumed to be along z), and m are the fluctuations about this net magnetization (necessarily transverse to lowest order). Note that this model still makes some assumptions (neglecting magnetic anisotropy, phonon dispersion, and optical phonon modes). Nevertheless, it is the most general formalism developed for addressing magneto-acoustic effects.

Recognizing that our system is symmetric for rotations about the z axis, we can simplify this to only phonons along wave vectors of the form $k(\sin\theta, 0, \cos\theta)$ to get

$$\begin{aligned} 0 = {} & \left(\rho\omega^2 - c_{1111}k^2\right)\Big[\left(\rho\omega^2 - c_{1313}k^2\right)^2\left(\omega^2 - \omega_s\omega_m\right) \\ & - \left(\rho\omega^2 - c_{1313}k^2\right)\gamma\frac{b_2^2}{M_0}k^2\left(\omega_m\cos^2\theta + \omega_s\cos^2 2\theta\right) - \gamma^2\frac{b_2^4}{M_0^2}k^4\cos^2\theta\cos^2 2\theta\Big] \\ & - \left(\rho\omega^2 - c_{1313}k^2\right)\gamma\frac{b_2^2}{M_0}k^2\Big[\omega_s\left(\rho\omega^2 - c_{1313}k^2\right)\sin^2 2\theta + \gamma\frac{b_2^2}{M_0}k^2\cos^2\theta\sin^2 2\theta\Big] \quad (3.16) \end{aligned}$$

where

$$\omega_m = \gamma\left(\frac{2a}{M_0}k^2 + H + 4\pi M_0\sin^2\theta\right) = \omega_s + 4\pi\gamma M_0\sin^2\theta. \quad (3.17)$$

This determinant defines the dispersion relation along an arbitrary direction, which we plot in Fig. 3-10. Notice that this includes multiple hybridizations of the magnon modes with the phonons, one for the longitudinal modes and one for the transverse modes. In general, these hybridizations have no particular symmetry.

However, along high symmetry directions ($\theta = 0, \pi/2$), things simplify a great deal. Along

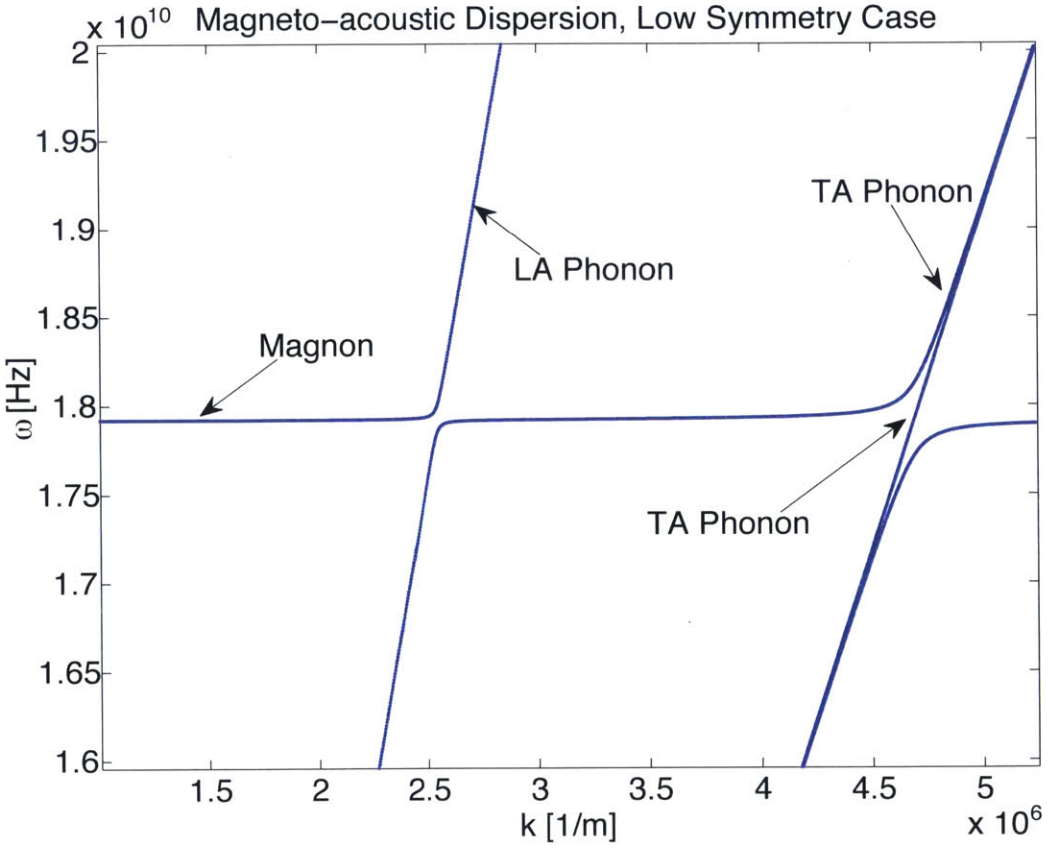

Figure 3-10: Magneto-acoustic dispersion relation near band crossings for the low symmetry case. Bands are linear elsewhere. Note the hybridization of the magnon and LA phonon modes as well its hybridization with one of the TA phonon modes.

$\theta = 0$ eq. 3.17 becomes

$$0 = \left(\rho\omega^2 - c_{1111}k^2\right)\left[\left(\rho\omega^2 - c_{1313}k^2\right)^2\left(\omega^2 - \omega_s^2\right) - 2\left(\rho\omega^2 - c_{1313}k^2\right)\omega_s\gamma\frac{b_2^2}{M_0}k^2 - \gamma^2\frac{b_2^4}{M_0^2}k^4\right] \tag{3.18}$$

[6] which can be factored as

$$\left(\rho\omega^2 - c_{1111}k^2\right)\left[\left(\rho\omega^2 - c_{1313}k^2\right)\left(\omega + \omega_s\right) + \frac{\gamma b_2^2 k^2}{M_0}\right]\left[\left(\rho\omega^2 - c_{1313}k^2\right)\left(\omega - \omega_s\right) - \frac{\gamma b_2^2 k^2}{M_0}\right] \tag{3.19}$$

to get the same equations as eq. 3.13. We therefore see that the two approaches give equivalent results.

On the other hand, when $\theta = \pi/2$ we have

$$0 = \left(\rho\omega^2 - c_{1111}k^2\right)\left(\rho\omega^2 - c_{1313}k^2\right)\left[\left(\rho\omega^2 - c_{1313}k^2\right)\left(\omega^2 - \omega_s\omega_m\right) - \frac{b_2^2}{M_0}k^2\omega_s\right]. \tag{3.20}$$

Notice that now two of the phonon modes have decoupled from the magnon modes in this case. Specifically, the $\hat{y}$ polarized transverse phonons, which are perpendicular to both $\vec{k}$ and $\vec{H}$ have no coupling to the magnetic field and so are unaffected, while the $\hat{x}$ polarized phonons are strongly coupled to the magnons. This is the Cotton-Mouton effect, i.e. linear birefringence. The dispersions for both high symmetry cases are shown in Fig. 3-11. Unlike in Fig. 3-10, along the high symmetry direction the bands only hybridize once. The longitudinal modes do not hybridize because they are symmetry protected in these directions, either by mirror symmetry (Cotton-Mouton regime) or rotational symmetry about the $\hat{z}$ axis (Faraday regime). This latter regime is also important because the eigenmodes of the transverse phonons (and hybridized magnons) are circularly polarized, indicative of a strong time-reversal symmetry breaking.

3.3.3 Acoustic Faraday Effect

Before going any further in analyzing the specifics of the magneto-acoustic interaction, there is one final correction that the model in Gudkov and Gavenda [213] failed to account for, namely the existence of finite lifetimes. Phonons have comparatively long lifetimes

[6] Gudkov and Gavenda [213] have an error in their form of this equation, which reads $(\rho\omega^2 - c_{1313}k^2)(\omega^2 - \omega_s\omega_m)$.

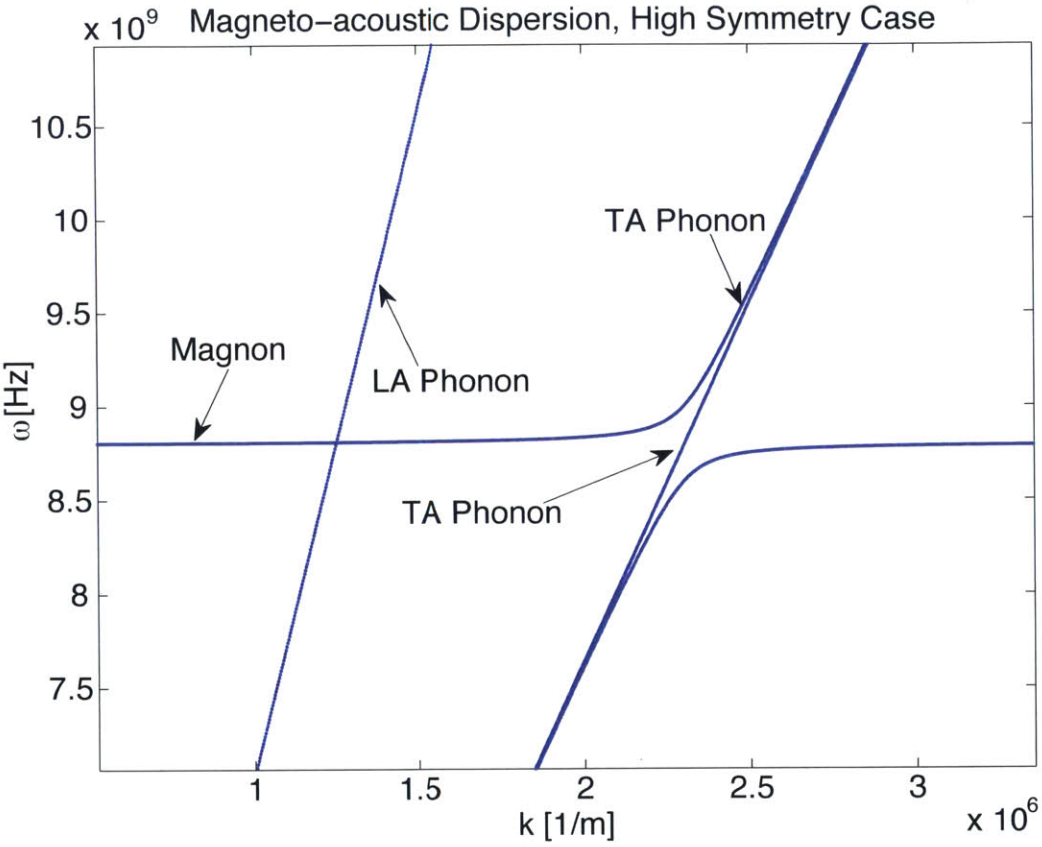

Figure 3-11: Magneto-acoustic dispersion relation near band crossings for the high symmetry case. Bands are linear elsewhere. Note the crossing of the magnon and LA phonon modes (unlike in Fig. 3-10), as well as the hybridization of one TA phonon mode with the magnon mode. The resonant frequency is slightly shifted between this figure and the general case in Fig. 3-10 because of the magnon mode's angular dependence.

in magneto-acoustics, with their chief dissipation mechanism being due to finite magnon lifetimes. This can be modeled by adding a finite lifetime term to the magnon modes (of the form $\dot{m} = -m/\tau$ where τ is the lifetime). Adding that term to the dispersion relation (and dropping the magnon dispersion correction as negligible), we can solve for the dispersion (as $k(\omega)$ rather than the standard $\omega(k)$)

$$k_{\pm} = \omega\sqrt{\frac{\rho}{c_{1313}}}\frac{1}{\sqrt{1 - \frac{\gamma}{\gamma H \pm (\omega - \frac{i}{\tau})}\frac{b_2}{c_{1313}}\frac{b_2}{M_0}}} \tag{3.21}$$

which we can simplify in terms of dimensionless quantities $\Omega = \omega\tau$, $\beta = \gamma\tau H$, $\xi = \gamma b_2^2 \tau / c_{1313} M_0$, $\mu = 4\pi\gamma\tau M_0$ and $l = \sqrt{c_{1313}\tau^2/\rho}$ to give

$$k_{\pm} = \frac{\Omega}{l}\left(1 - \frac{\xi}{\beta \pm \Omega \mp i}\right)^{-1/2}. \tag{3.22}$$

When a linearly polarized wave enters a circularly birefringent medium, it acquires a phase difference that we can express as

$$u(z) = \frac{1}{2}\begin{bmatrix} 1 & 1 \\ -i & i \end{bmatrix}\begin{bmatrix} e^{ik'_+ z - k''_+ z} & \\ & e^{ik'_- z - k''_- z} \end{bmatrix}\begin{bmatrix} 1 & i \\ 1 & -i \end{bmatrix}\begin{vmatrix} u_x(0) \\ u_y(0) \end{vmatrix} \tag{3.23}$$

$$= \frac{1}{2}\begin{vmatrix} e^{ik'_+ z - k''_+ z}[u_x(0) + iu_y(0)] + e^{ik'_- z - k''_- z}[u_x(0) - iu_y(0)] \\ -ie^{ik'_+ z - k''_+ z}[u_x(0) + iu_y(0)] + ie^{ik'_- z - k''_- z}[u_x(0) - iu_y(0)] \end{vmatrix} \tag{3.24}$$

where z is the position an arbitrary distance along the magneto-acoustic and $k_{\pm} = k'_{\pm} + ik''_{\pm}$. Since we're interested in the phase acquired, we set the initial polarization to be $\phi = 0$ (i.e. $u(0) = u_x(0)\hat{x}$), giving

$$\tan^2\phi = \frac{\cosh[k''_+ - k''_-]z - \cos[k'_+ - k'_-]z}{\cosh[k''_+ - k''_-]z + \cos[k'_+ - k'_-]z} = \tan\frac{[k_+ - k_-]z}{2}\tan\frac{[k^*_+ - k^*_-]z}{2}. \tag{3.25}$$

Neglecting circular dichroism gives

$$\phi = \frac{k_+ - k_-}{2}L \tag{3.26}$$

where L is the total length of the magneto-acoustic. This is the standard form of the acoustic Faraday effect, which rotates the angle of polarization. Materials that realize this effect are

called gyrators. Illustrative cases of real and imaginary Δk are shown in Fig. 3-12 which is approximately Lorentzian.

3.3.4 Cotton-Mouton Effect

Using the formalism developed for the acoustic Faraday effect, the dispersion relation for the Cotton-Mouton effect is

$$k = \omega\sqrt{\frac{\rho}{c_{1313}}}\frac{1}{\sqrt{1-\frac{\gamma^2 H}{(i\omega+\frac{1}{\tau})^2+\gamma^2 H(H+4\pi M_0)}\frac{b_2}{c_{1313}}\frac{b_2}{M_0}}} \tag{3.27}$$

or

$$k = \frac{\Omega}{l}\left(1-\xi\frac{\beta}{(i\Omega+1)^2+\beta(\beta+\mu)}\right)^{-1/2}. \tag{3.28}$$

The other transverse polarization is just $k = \omega\sqrt{\rho/c_{1313}} = \Omega/l$. The difference between these wave vectors gives the linear birefringence for the real part and linear dichroism for the imaginary part. Note, though, that the imaginary part is solely from the polarization coupled to the magnetic field (i.e. when $\hat{n}\|\hat{H}$). Thus any dichroic losses in this regime are due solely to that polarization, and the material acts like a perfect linear polarizer. The dependence of this dispersion relation's real and imaginary parts is illustrated in Fig. 3-13.

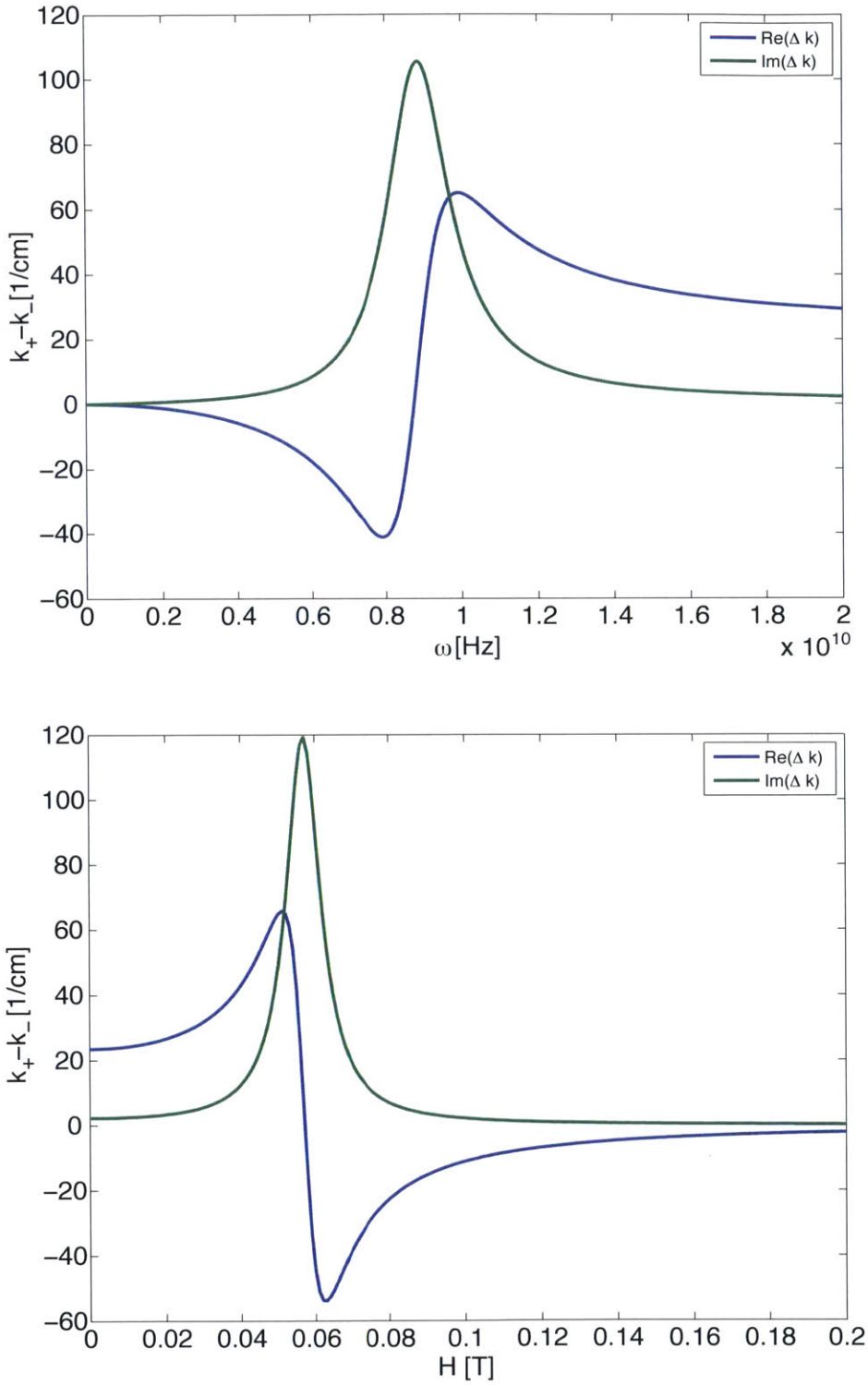

Figure 3-12: Functional dependence of the acoustic Faraday effect. (A) Frequency dependence for $H = 0.05$T. Approximately Lorentzian. (B) Magnetic field strength dependence for $\omega = 10$ GHz. Again approximately Lorentzian.

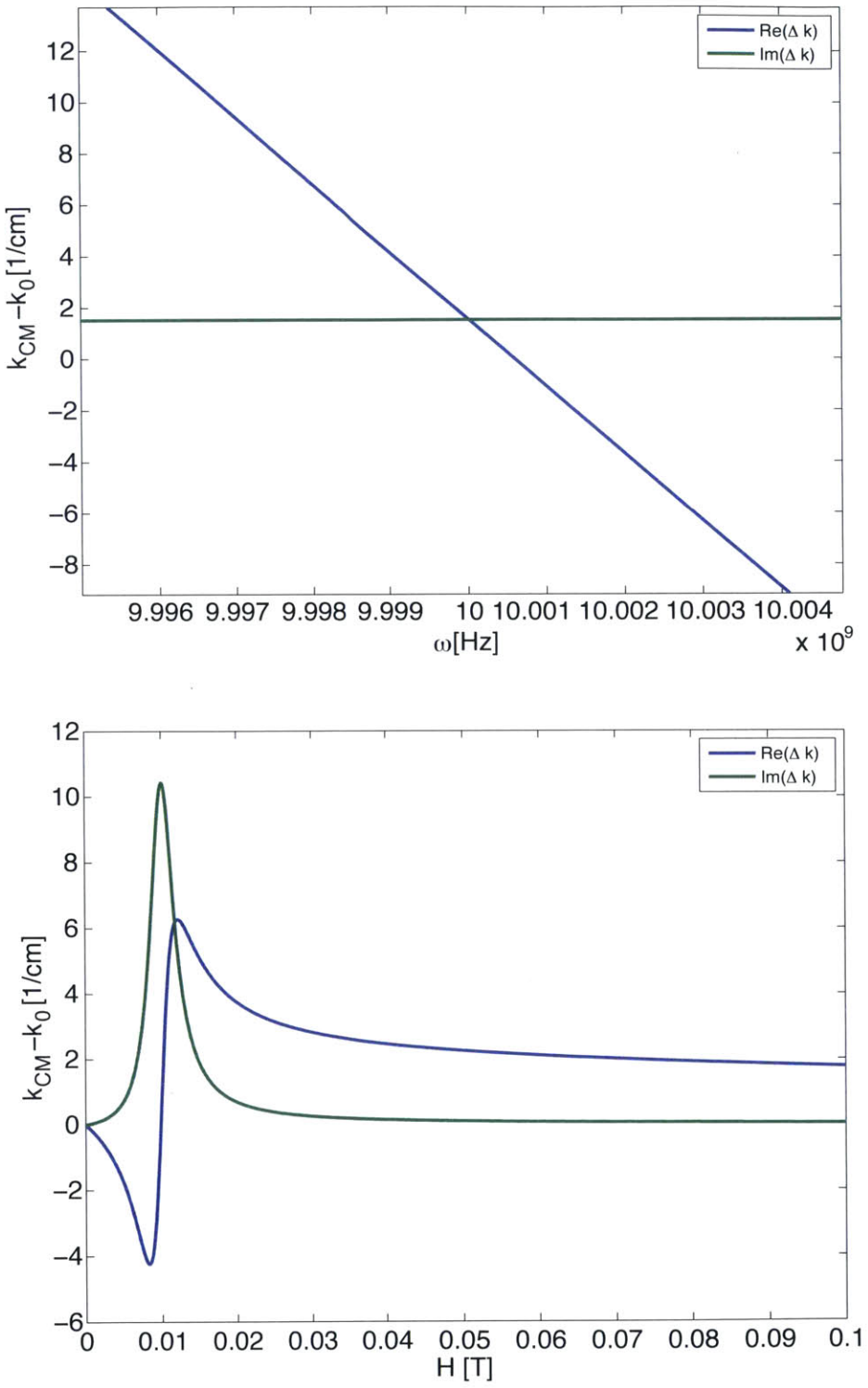

Figure 3-13: Functional dependence of the Cotton-Mouton effect. (A) Frequency dependence for $H = 0.01$T. Note linearity of real and imaginary parts. (B) Magnetic field strength dependence for $\omega = 10$ GHz. Approximately Lorentzian. Real part decays much more slowly than imaginary part.

3.4 Magneto-acoustic Phonon Computing

The techniques for phonon computing considered in Ch. 3.2, with very few exceptions, suffer from the limitations imposed on reciprocal devices. The nonreciprocal approaches to phonon computing, on the other hand, have been limited by the use of moving parts [236] or complicated driving methods [237, 238]. Similar limitations also apply to computing elements using thermal phonons (such as thermal diodes, transistors, logic, and memory [1, 257, 258, 259, 260, 261]). One contributing factor keeping phononic computers constrained to reciprocal devices has been the assumption that a phononic computer would act like an electronic one. In particular, for electronics information is encoded in a scalar voltage intensity (high or low voltage = logical 1 or 0) and as such it was seen as natural that phononic information would be encoded in the same way – as a scalar temperature (hot or cold = logical 1 or 0) or intensity (present or absent = logical 1 or 0). Moreover, electronic circuits rely more upon breaking spatial symmetries and interfacial effects (e.g. pn junctions) for constructing circuits, ergo phononic circuits principally were designed around engineering interfaces or asymmetric scattering. This has led to a focus on nanostructures [262, 263] or 1D nonlinear materials [1, 257, 258, 264] to boost the surface-to-volume ratio, however these devices are difficult to fabricate.

By moving past the presumption of a strict analogy between electronic and phononic computing, we can construct alternative phononic computing architectures that more directly address the challenges of phononic transport control. In this section, we illustrate this principle by making an analogy with an information carrier that bears little resemblance to electrons, namely photonic computing. As such, it is natural for us to encode information using the phonon's polarization for a current of transverse acoustic phonons (in particular we define transverse vertical as logical 1, transverse horizontal as logical 0, and leave the longitudinal phonons unused as we restrict ourselves to purely transverse or longitudinal magnetic fields where LA modes are decoupled from the magnetic field, see Ch. 3.3). Our circuit elements must therefore modify some arbitrary transverse, elliptic polarization, and therefore we require gyrators (which rotate the polarization angle, also called Faraday rotators in photonics) and polarizers (which filter out a linear polarization) from which to construct diodes (also called isolators or Faraday isolators in photonics [265]) and transis-

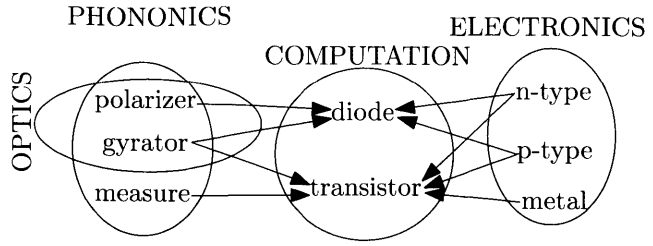

Figure 3-14: Decomposition of abstract logic elements into their constitutive components in electronics, optics, and phononics. Circles denotes the classes of information carriers: electronic, optical, phononic, and (abstract) logical. Each circle contains a list of elementary devices that control these information carriers. For electronics, optics, and phononics, the basic elements are typically a single material or interface while for logical signals are more abstract and as such defined by their effect on information. Arrows indicate which the relation between the basic material elements and their composition into abstract logic elements. From S. R. Sklan and J. C. Grossman, *New J. Phys.* **16**, 053029 (2014) [256].

tors. The decomposition of abstract logic elements into the basic devices of electronics, optics, and phononics is illustrated in Fig. 3-14. To make sure that our devices fall into the strong reciprocity breaking regime, we require systems that unambiguously break time-reversal, rather than reflection, symmetry – and as such we will make use of magnetic fields. For there to be a strong coupling between magnetic fields and a phonon current, we use magneto-acoustic materials (see Ch. 3.3).

3.4.1 Magneto-acoustic Phonon Isolators

In optics, isolators are constructed though sandwiching a $\pi/4$ gyrator between a pair of linear polarizers that are rotated by $\pi/4$ with respect to each other (see Fig. 3-15)) [265]. In the forward configuration, a signal enters, becomes polarized along first polarizer, acquires a rotated polarization from the gyrator, and emerges with a polarization parallel to the second polarizer's. Conversely, in the reverse configuration the signal becomes polarized and then acquires the same rotation in polarization, thereby emerging orthogonal to the second polarizer. Using the Cotton-Mouton effect for polarizers and the acoustic Faraday effect for gyrators, we are able to construct both polarizers and gyrators from magneto-acoustics just by sculpting the magnetic field's strength and orientation. To optimize an isolator for a single frequency input, one must select magnetic field strengths such that dichroism is minimized in the gyrator (as even weak circular dichroism can render destructive interference

imperfect) and strong dichroism for the polarizers.

In designing our gyrators and polarizers we can independently select the field strength, phonon frequency, and magneto-acoustic length. We do not concern ourselves with optimizing the properties of the magneto-acoustic, taking them to be fixed and using values from a representative experiment [266]. We select a phonon frequency of 10 GHz, which slightly larger than that in Guermeur et al. [266] but more clearly reveals the operation of our circuits. $k(H)$ is then analytically calculated and numerically evaluated for each element's dispersion and these are used to select realizable magnetic fields strengths that simultaneously give desirable amounts of birefringence and dichroism (0.01T for the polarizers and 0.1T for the gyrator). Finally, we select lengths such that the gyration ($\theta = L(k'_+ - k'_-)/2$) is as close to $\pi/4$ as possible and that the filtering ($\alpha = \exp(-k''_{\|}L)$) of the undesired polarization is strong. The resulting isolator is then evaluated numerically by calculating the phase acquired by the phonon current as it traverses each element. The intensity profiles of the different combinations of input polarizations and directions are plotted in Fig. 3-15, which reveals that the circuit unambiguously blocks (with more than a 95% loss of intensity) all inputs except for the desired polarization and direction. Since the right and left circularly polarized eigenmodes in the acoustic Faraday effect regime have opposite signs in their imaginary components [7], the amplification observed in the forward configuration is to be expected.

3.4.2 Magneto-acoustic Phonon Transistors

Designing a transistor necessitates that we use a more sophisticated approach than was needed for the isolator. In particular, having some form of measurement operator is necessary for the creation of a transistor in our framework. Measurement of polarization-dependent phonon intensity is somewhat challenging at high frequencies and while we don't consider this problem in detail Fig. 3-16 illustrates a heuristic approach. It is quite likely there are more efficient or more sensitive experimental realizations of a measurement operator, however the form we sketch here is conceptually simple and sufficiently functional for designing a proof of concept phonon transistor. In particular, our measurement operator can be separated into

[7] the exponentially growing component arising from the extraction of energy from the magnetic field via the magnons.

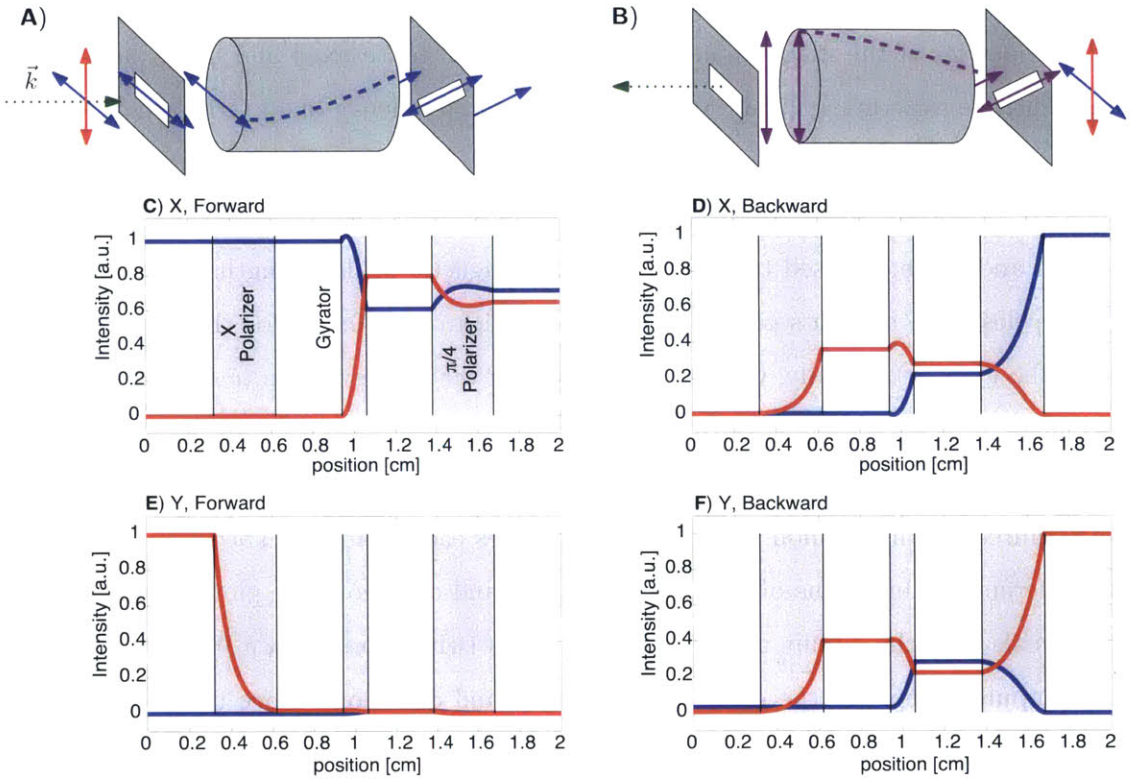

Figure 3-15: Operation of an isolator (A), (B): Model schematic of an isolator constructed from a gyrator (cylinder) placed between by two polarizers (rectangles, where the gaps denote the polarization that is not blocked). Blue and red lines denote the x and y polarizations, with the purple line (in (B) only) constituting a superposition of both. The Green lines indicate the direction of signal propagation (that is, the wave vector, $\vec{k}$). (A) Forward configuration. Unpolarized signal enters, becomes polarized, gyrated, and then leaves. (B) Backward configuration. Unpolarized signal enters, becomes polarized, gyrated, and then blocked. (C)-(F): Simulation of the isolator in operation. Blue and red lines are the intensities of their respective polarizations. Grey rectangles indicate magneto-acoustic material, which is arranged in the same pattern as in (A) and (B). (C) and (D) have the incident signal x-polarized (the allowed input polarization), while (E) and (F) have the incident signal y-polarized. In (C) and (E) the signal approaches in the forward configuration, whereas in (D) and (F) the signal approaches from the reverse configuration. Only in (C) is the signal transmitted without appreciable loss in intensity. From S. R. Sklan and J. C. Grossman, "Phonon diodes and transistors from magneto-acoustics." *New J. Phys.* **16**, 053029 (2014). Available under a Creative Commons Attribution 3.0 license [256].

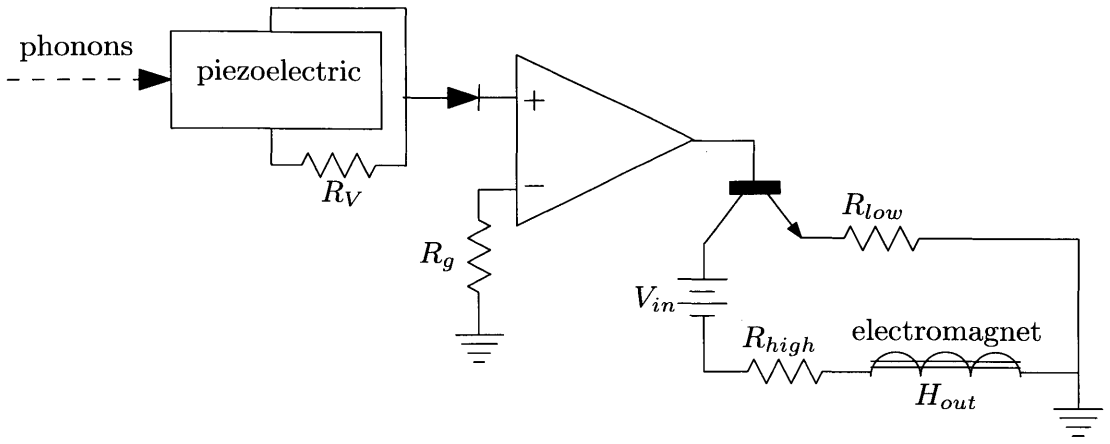

Figure 3-16: Heuristic measurement operator. Phonon current traverses piezoelectric, which transduces an electronic signal that is proportional to the amplitude of one phonon polarization polarized. The resultant AC voltage is then rectified with a diode and amplified via an op amp to produce a constant DC voltage. This voltage is used to switch between applying or suppressing ($R_{high} \gg R_{low}$) a current that drives an electromagnet (producing a magnetic field). In this figure, a magnetic field withheld upon the application of a phonon current exceeding a threshold value. From S. R. Sklan and J. C. Grossman, "Phonon diodes and transistors from magneto-acoustics." *New J. Phys.* **16**, 053029 (2014). Available under a Creative Commons Attribution 3.0 license [256].

multiple steps: detection and transduction (piezoelectric), rectification (electronic diode), amplification (op amp), and application (electronic transistor, electromagnet). These steps are all differentiated and each is in principle realizable.

Once we have a measurement operator, we can construct a transistor by sending a fixed logical 0 signal into a gyrator and then selecting whether or not a magnetic field should be applied via measuring a second phonon current's polarized intensity. If the polarized intensity exceeds the threshold then a magnetic field is withheld (the gyration is strongest as $B \to 0$ [8].) Remanence magnetization (also called residual magnetization) within the magneto-acoustic thus supplies the magnetic field to required for the operation of the gyrator working. On the other hand, when the polarized intensity falls below the threshold, a magnetic field will be applied to the magneto-acoustic, thereby suppressing the circular birefringence and partially cancelling the gyration (perfect cancellation requires $B \to \infty$). Fig. 3-17a,b summarizes the operation of the transistor in these two cases. Since the transistor input signal is not the same as the output signal, it is possible for a relatively

[8] In actuality a small, non-zero field is probably preferable as this model does not include thermal fluctuations reducing the magneto-acoustic's remanence magnetization from the saturation magnetization

modest intensity input to produce a high intensity output. This effectively amplifies the information-carrying current, as is typical for a transistor [9].

If the transistor is to work as a logic operation in our basis, the gyration should ideally be $\pi/2$. Repeating the process previously used to design the isolator (magnetic field of 10^{-4}T for off and 0.5T for on), we model the transistor in Fig. 3-17c,d. In these simulations we abstract the measurement device and instead focus upon the effect of applying or withholding a magnetic field.

3.4.3 Error Sensitivity

While these circuit elements clearly perform their desired operations, there remain are imperfections for each element. For example, when a field is applied to the transistor and so the gyrator is off, the relatively weak field intensity allows a small gyration to persist. On the other hand, when no field is applied and the gyrator is on, circular dichroism prevents perfect destructive interference between the left and right circularly polarized modes, which results in a small horizontally polarized remnant signal. In particular, for an incoming signal at $\phi_{in} = 0$ and the magneto-acoustic length optimized for $\phi_{out} = \pi/2$, the outgoing polarization angle is limited by

$$\tan\phi = \coth\left(\frac{\pi}{2}\frac{\mathrm{Im}[k_+ - k_-]}{\mathrm{Re}[k_+ - k_-]}\right) \tag{3.29}$$

[10]. This error can be compensated for by allowing some fuzziness in our definitions of the polarization angles encoded as logical 0 or 1 (this is especially reasonable as the piezoelectric transduction method used in in Fig. 3-16 is rather insensitive to the undesired polarization), there is a more stringent limit implied by these errors. Because the erroneous phases acquired

[9]Circular dichroism in the gyrator could, in principle, also induce amplification of a current passing from source to drain of. However, the amplified component would be necessarily circularly (and not linearly) polarized, and therefore it would need a greater complexity in the circuit design. In particular, it would require polarizers also that would also be driven by the measurement gate (i.e. error-correction) to maintain the linearly polarized logical one and zero basis that we have been using. A circular basis, on the other hand, could exploit this amplification, however it would also complicate the design, particularly the measurement operator.

[10]Numerical results slightly exceed this limit, and we observe numerically that the maximum of ϕ occurs using a transistor that is slightly thinner than would be predicted by $L = \pi/(k'_+ - k'_-)$ (the length we assume in eq. 3.29). This is fairly negligible, however, and in most scenarios the estimated length is sufficiently accurate for our designs.

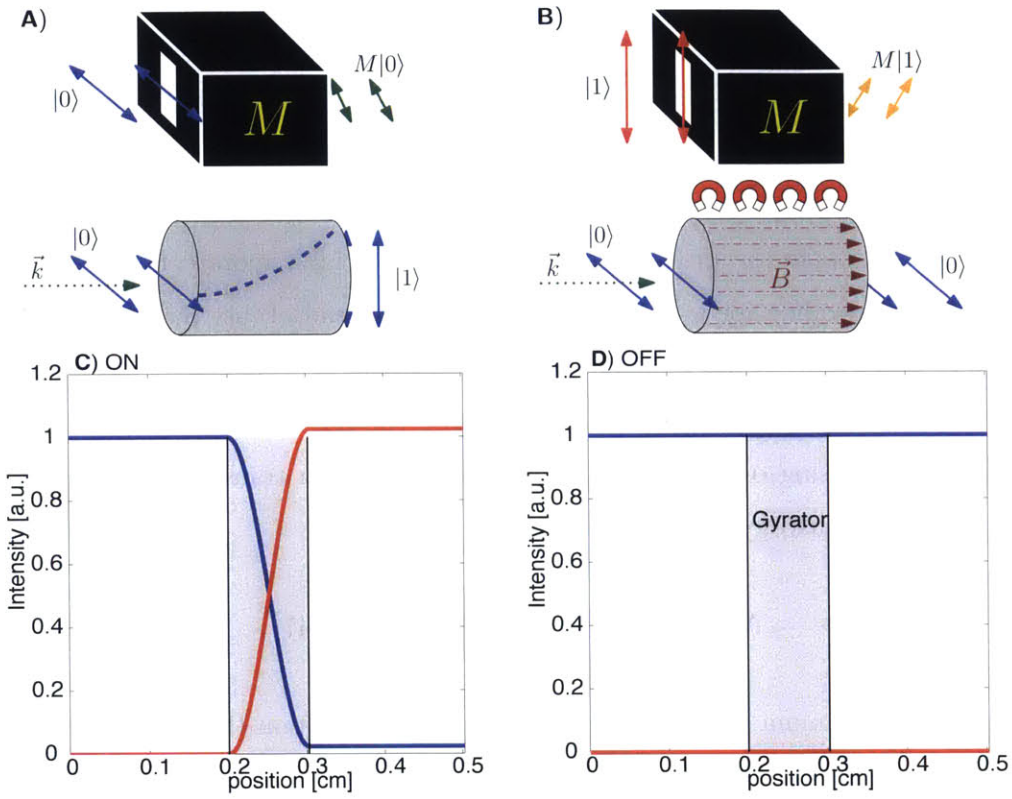

Figure 3-17: Simulation of a phonon transistor. Conventions are the same as Fig. 3-15. (A) Schematic model of the transistor in the on state. The black box labeled M indicates the measurement operator, a heuristic of which is presented in Fig. 3-16. (B) Schematic model of the transistor in the off state. The magnets represent the creation of a magnetic field (dark red lines) applied to the gyrator. (C) Simulation of the transistor in the on state (where no suppressing field), switching the phonon current from 0 to 1 as it goes from source to drain. (D) Simulation of the transistor in the off state (where the suppressing field is applied), and no switching of the phonon polarization occurs. From S. R. Sklan and J. C. Grossman, "Phonon diodes and transistors from magneto-acoustics." *New J. Phys.* **16**, 053029 (2014). Available under a Creative Commons Attribution 3.0 license [256].

by a signal traversing a transistor in the off state will accumulate, there exists a maximum total length of a series transistors that can be chained while simultaneously maintaining well-separated logic states. In practice, this difficulty can be partially mitigated by introducing repeater circuits (which maps a noisy input to a specific, less noisy value, such as we observe in our transistor design when the signal is sent to the gate, not the source) in sufficiently long operations. Thinking of each gyrator in a series as being tied to a different measurement gate, then this length constraint also determines the maximum number of independent inputs in a logic operation that can be performed without requiring a repeater. It is possible exceed this limit, however, as multiple phonon currents can superimpose, an approach we exploit in Ch. 3.4.5. To make the practical effects of this constraint more concrete, we need to define a specific encoding for a range of polarizations instead of just perfectly horizontally or vertically polarized. In particular, we now define logical 0 as $[0,\pi/5]$ and logical 1 as $[3\pi/10,\pi/2]$ (with the other quadrants mapped into the 1st by reflection symmetry). For this encoding and using our previous parameter values for a transistor, we find that the number of (fixed length) gyrators goes as

$$N = \text{floor}\left[6.4H^2 - 0.059|H| - 0.0047\right], \tag{3.30}$$

where N is the maximum number of gyrators, floor is a function that rounds down to the nearest integer, and H the applied field strength in Tesla. For variable length gyrators we can increase the number of transistors, but the total length of the series remains the fundamental constraint. From this relation we can also determine that minimum allowable field strength for the off state is therefore 0.4T. A similar limit for the on state also exists, but the fact that $B \approx 0$ for this regime makes it a weaker constraint on the number of stages and field strengths.

The existence of circular dichroism in the acoustic Faraday effect thus yields a systematic error which constrains computational power. In addition to such systematic errors, random errors can also degrade an isolator or transistor's operation. Although sufficiently thick polarizers are notably insensitive to such errors due to their exponential damping, gyrators can be extremely sensitive. Generally, this sensitivity is a function of frequency and magnetic field intensity. To evaluate the sensitivity of an arbitrary gyrator, we use the linearized equation of uncertainty propagation. When expressed in terms of fractional uncertainties,

	Polarizer	Gyrator	Transistor
δH	81.5μG	3.42G	25.0G
$\delta\omega$	3.32kHz	34.2MHz	49.5MHz
δL	30.0μm	12.0μm	10.0μm

Table 3.1: Maximum acceptable tolerances for errors in the independent parameters, given an assumption of 1% operational error. Each calculation is done for an error in isolation, i.e. assuming that all other errors are 0. The "polarizer" and "gyrator" columns correspond to the elements of the isolator. Tolerances for the transistor are calculated in the off state, where the constraints are more stringent. From S. R. Sklan and J. C. Grossman, "Phonon diodes and transistors from magneto-acoustics." *New J. Phys.* **16**, 053029 (2014). Available under a Creative Commons Attribution 3.0 license [256].

this gives the result:

$$\left|\frac{\sigma_{\Delta kL}}{\Delta kL}\right|^2 = \left(\frac{\sigma_L}{L}\right)^2 + \left|\frac{\partial \Delta k}{\partial H}\right|^2 \left(\frac{\sigma_H}{H}\right)^2 + \left|\frac{\partial \Delta k}{\partial \omega}\right|^2 \left(\frac{\sigma_\omega}{\omega}\right)^2. \tag{3.31}$$

This approach overestimates the effects of random errors, as it does not differentiate between contributions to the real and imaginary parts of the dispersion. To determine the maximum tolerance for a given source of error, we consider each of the errors acting in isolation. The results of this calculation are summarized in Table 3.1. The noticeably lower tolerances for the polarizers in the isolator come from a reliance upon resonant losses, which constrains $B(T)$. However, this is not too problematic as the operation of the polarizers is typically the least integral part of the isolator. So long as they yield appreciable losses, their precise magnitude is unimportant. Ergo we can more easily accept errors in our polarizers than in any other part of the circuit. Furthermore, the performance of a polarizer can be easily improved just by increasing its thickness until the undesired polarization is completely blocked.

3.4.4 Logic Gates

From diodes and transistors, it is possible to create arbitrary logic gates. We illustrate this with the circuit diagrams of all the two-input logic gates in Fig. 3-18, where the white dots are $\pi/2$ rotators, the black dots vertically activated control elements (no rotation when vertical polarization absent, $\pi/2$ rotation when present, similar to a controlled NOT gate), the two binary inputs are labeled X and Y and the output is Z. Notice that all of these

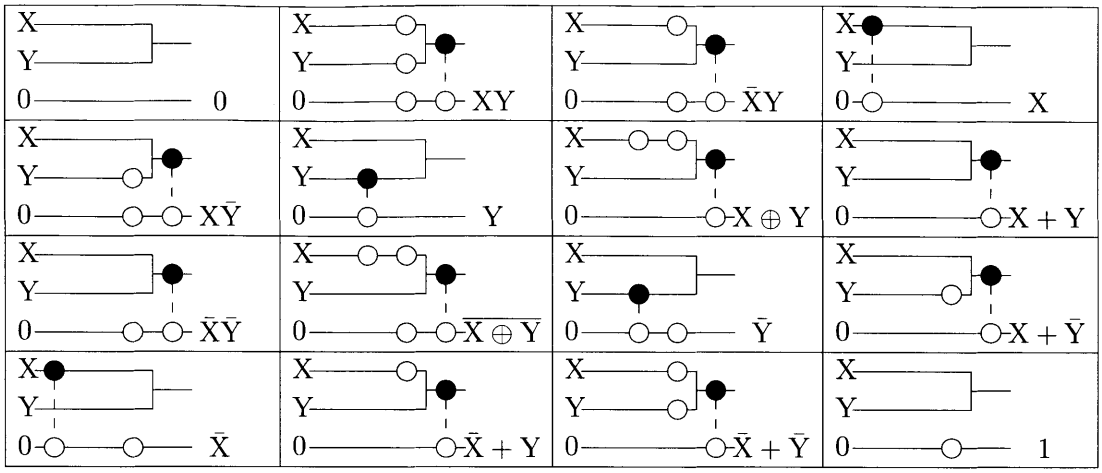

Figure 3-18: Table of all the two-terminal logic operations $Z(X, Y)$ implemented in the magneto-acoustic architecture. White dots are $\pi/2$ rotations and black dots are vertically activated control elements. Logic functions are denoted at the lower right corner (the output terminal) for each box in the table.

gates share basic similarities. In principle, we could create a gate containing controls and gyrators at every location, and then choose which ones to activate at a given time. This would be an arbitrary, programmable logic gate.

3.4.5 Frequency-domain Parallel Computing

We can even take this a step further by considering multiple frequencies of phonons multiplexed into a single signal. Since rotations are continuous and cumulative, any desired rotation can be split up into several smaller rotations that are controlled by several inputs. The nonlinearity of $k_+ - k_-$ in the acoustic Faraday effect (see Fig. 3-12 of Ch. 3.3) implies that the gyration is a nonlinear function of frequency. As such, splitting up the rotation means that each sum will in turn be different according to the relation

$$\Phi(\omega_i) \approx \sum_j \phi(\omega_i, H_j) L_j \tag{3.32}$$

where Φ is total rotation, ϕ is rotation per unit length, H_j is effective magnetic field strength of the j^{th} element, and L_j is its length. For there to be sufficient degrees of freedom that arbitrary rotations are possible at each frequency, it is necessary that ϕ is not separable (i.e. cannot be written in the form $f(\omega)g(H)$) and that there are at least as many elements

as there are frequencies (i.e. that $j \geq i$). In actuality 3.32 only works in the limit of no circular dichroism in the acoustic Faraday effect, which is at best an approximation. A more accurate calculation incorporating losses gives

$$\begin{aligned} \tan^2 \Phi(\omega_i) &= \tan\left(\frac{\sum_j [k_{j+} - k_{j-}]L_j}{2}\right) \tan\left(\frac{\sum_j [k^*_{j+} - k^*_{j-}]L}{2}\right) \\ &= \frac{\cosh\left(\sum \Delta k''_j L_j\right) - \cos\left(\sum \Delta k'_j L_j\right)}{\cosh\left(\sum \Delta k''_j L_j\right) + \cos\left(\sum \Delta k'_j L_j\right)} \end{aligned} \tag{3.33}$$

where k is the wave vector, Δk is the difference or right and left circular polarization $k_+ - k_-$, k' is the real part of k, and k''. Given the complexity of this relation, it is helpful to numerically evaluate this dispersion relation and the resulting rotations. As such, we again use the same experimental results used in Sklan and Grossman [256] and proceed to the simplest case of two frequencies.

To begin designing the two-frequency gate, it was helpful to consider the fixed parameters of element length and frequency. In particular the chosen frequencies must have sufficiently different nonlinear responses for a given magnetic field strength. Moreover, we also seek to minimize the overall length. To tackle this problem, we considered the rotation produced in the 0 applied field limit, where all the magnetic field is due to the internal magnetic field of YIG. The resulting gyration as a function of frequency and length is plotted in Fig. 3-19. This shows three operating regimes. In the low frequency, thin element limit there is no rotation, as expected. In the thick element limit there is strong circular dichroism, which damps the signal to the point that no logic operation can be performed and leaves a $\pi/4$ polarization. Lastly, in the triangle of high frequency, thin element, there are bands of maximum and minimum rotation. We select thicknesses of 0.13 and 0.27 cm, near the center of the first two bands and adding up to the third band when combined. Frequencies are chosen as 10 and 20 GHz, both frequencies falling within the peak of the first and second bands but only the higher frequency hitting the maximum rotation peak of the third band. That is, if only one element is active, both frequencies get affected, but if they are both active only one frequency is affected.

Given this determination of ω and L, the magnetic field is now varied to create more precise control of the out-going polarizations (and determine the required values of H). For this

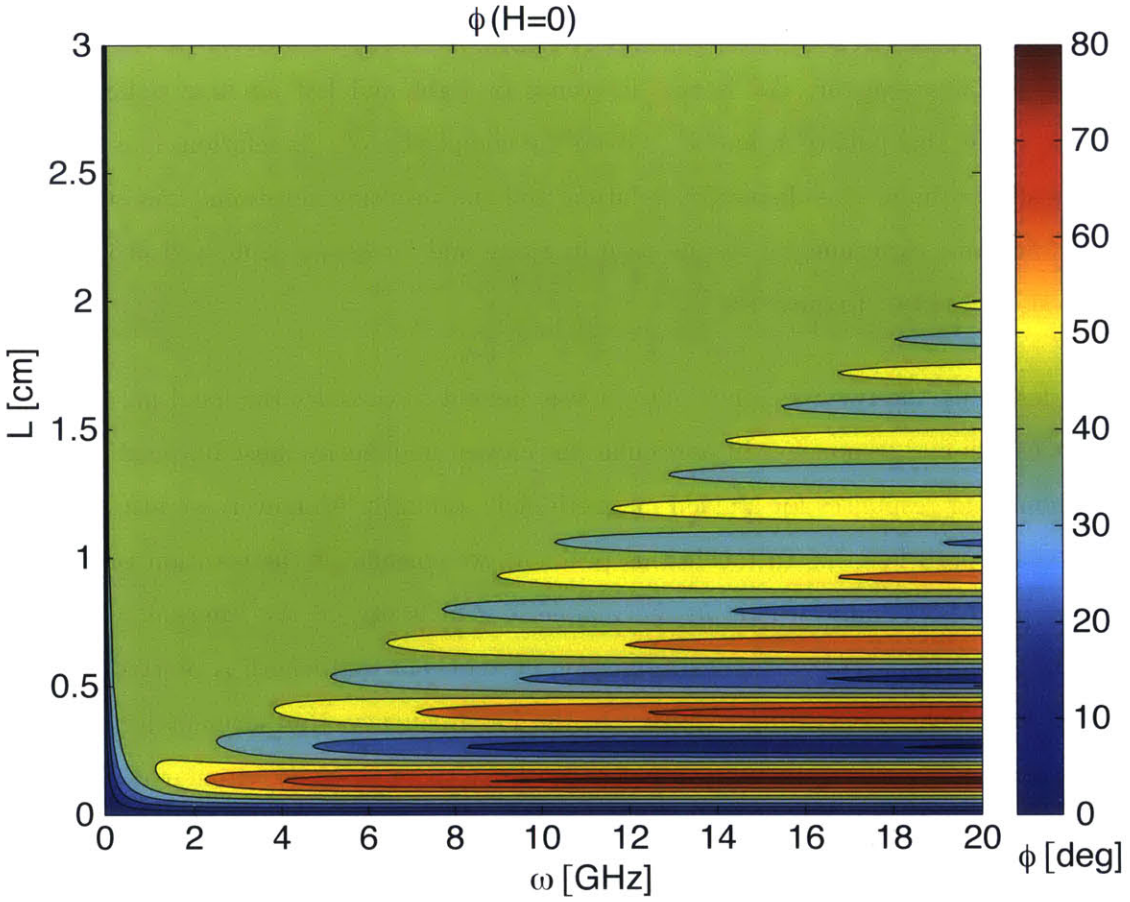

Figure 3-19: Rotation of a magneto-acoustic YIG gyrator in the intrinsic field limit. Length of the element is plotted along y, frequency of phonon current is along x. Color contours denote angle of rotation.

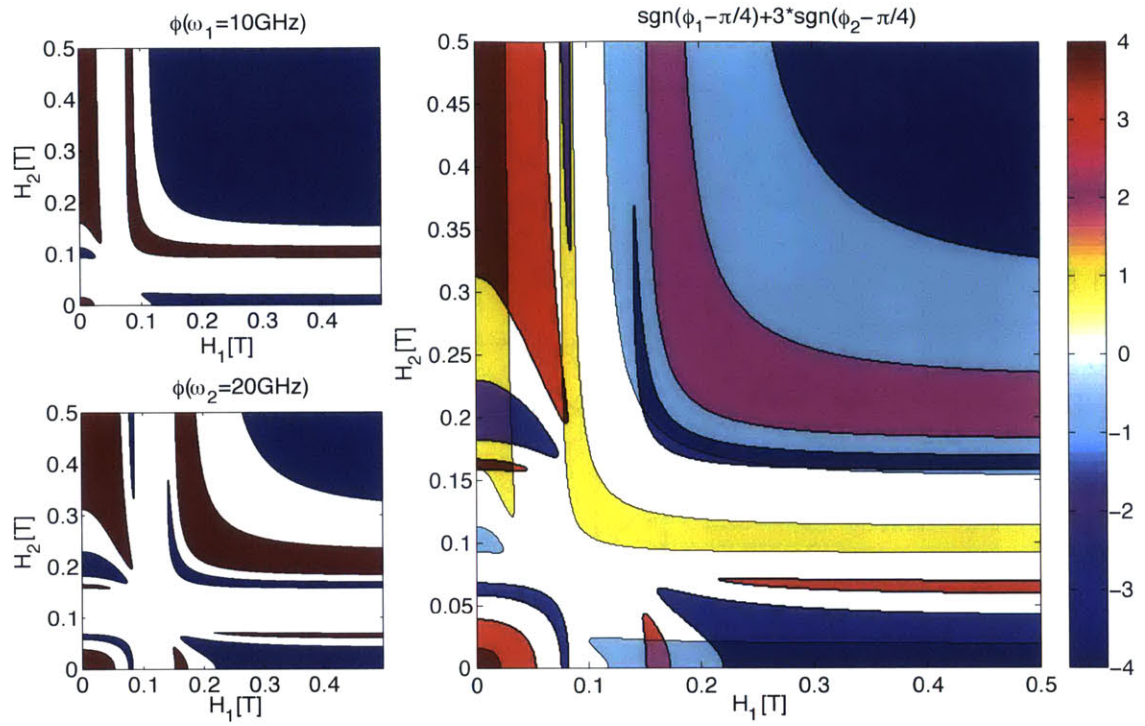

Figure 3-20: Logic outputs of the magneto-acoustic gate as function of applied field strengths. Part (a) is for 10 GHz and part (b) is for 20 GHz. The blue domain is for no rotation (logical 0 output), red is full rotation (logical 1 output) and white is intermediate (undefined logic value). Part (c) is the combination of the phase of parts (a) and (b), with logic states $(f(10), g(20)) = (0,0)$ for dark blue, (N/A,0) for blue, (1,0) for purple, (0,N/A) for cyan, (N/A,N/A) for white, (1,N/A) for yellow, (0,1) for magenta, (N/A,1) for red, and (1,1) for dark red.

to be useful, though, we must again broaden our logic states from precisely vertically or horizontally polarized signals. Instead, a range of acceptable polarizations defines each of the states. For this problem we select $[0, \pi/6)$ as logical 1 and $(\pi/3, \pi/2]$ as logical 0, leaving the intermediate region as a buffer. This allows us to define the logical output for a set input frequency and polarization as a function of total rotation vs. magnetic field strengths, which we plot in Fig. 3-20. Parts a and b of Fig. 3-20 are of the two frequencies individually and are colored to show the logic states in each part of the phase diagram. Part c overlays the phase boundaries of the previous parts, the intersections of which define regions where the magnetic fields are tuned to produce the desired logic operations on each frequency. The size of the domains also determines the error tolerance of the magnetic fields (similarly, the bands in Fig. 3-19 determine the error tolerances for lengths and frequencies).

Hence, selecting magnetic fields of $(H_1, H_2) = 0.25, 0.01$ T for an output of $(\Phi_1, \Phi_2) = (0,0)$,

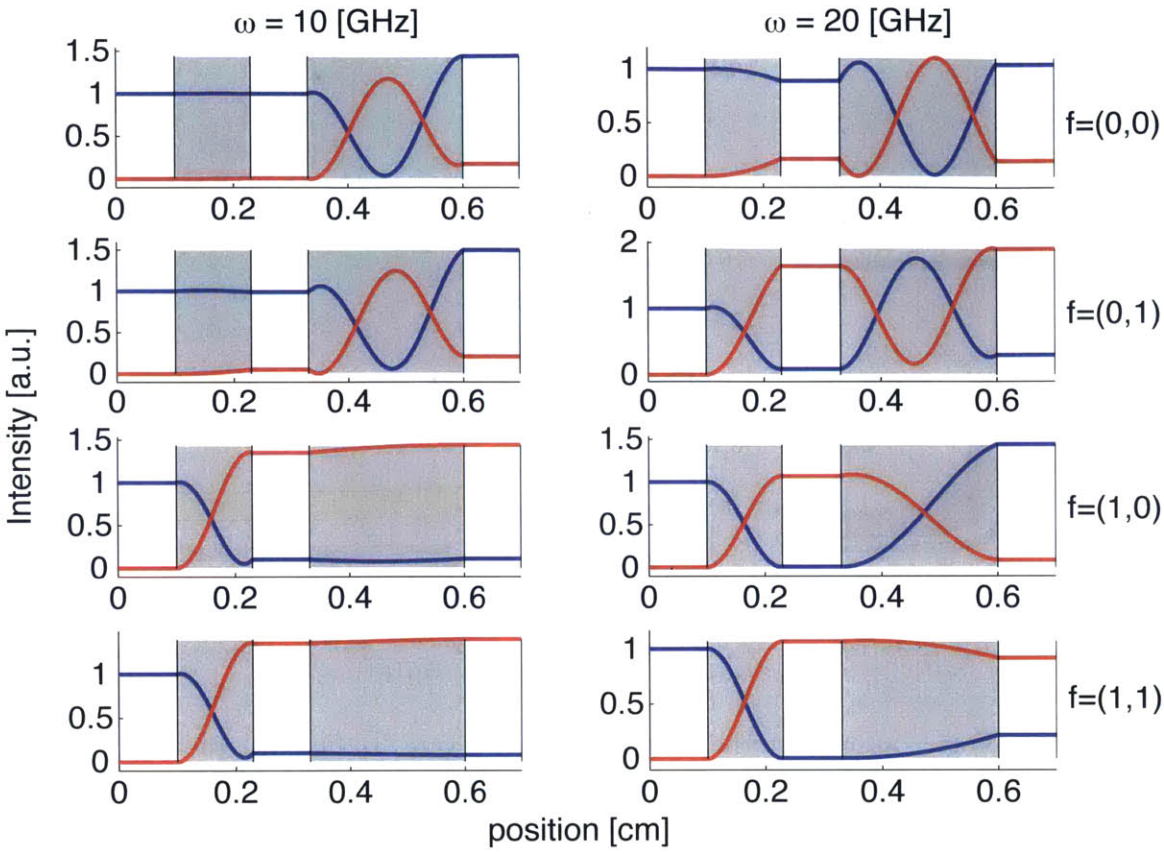

Figure 3-21: Numerical simulations of signals passing through the two stage gyrator. Plots are phonon intensity vs. position. The blue line denotes horizontal polarization and the red line denotes vertical polarization. Shaded regions are the magneto-acoustically active domains. Columns denote frequency – 10 GHz for the first and 20 GHz for the second. Rows are different logic operations, corresponding to different magnetic field strengths.

(0.16, 0.01) T for $(0,\pi/2)$, (0.02, 0.2) T for $(\pi/2, 0)$, and (0.02,0.32) T for $(\pi/2, \pi/2)$ allows us to map out all the two frequency operations. We plot the simulations of our circuit in Fig. 3-21, the columns being for a fixed frequency and the rows being for fixed field strengths. The individual plots use the same conventions as Fig. 3-15 and Fig. 3-17. Crucially, while the outgoing polarizations are not perfectly horizontal or vertical, they are well within the range of accuracy required for stable logic values. Should further refinement be needed, though, there is always the option of using the Cotton-Mouton effect to eliminate the extraneous polarization.

It is perhaps illustrative to compare these results with those of Mahboob et al. [241]. In both approaches, a frequency domain multiplexed signal was sent to a nonlinear phononic device

used to perform multiple logic operations. The approach considered here, however, is more flexible in its frequency scaling (increasing as N rather than 2^N for N frequency inputs). Furthermore, the technique in Mahboob et al. [241] requires the nonlinear interaction of different frequencies to produce additional frequency components, while our parallelization method goes the opposite extreme and does not assume any interaction between frequencies.

3.5 Magneto-acoustic Phonon Computing Conclusions

We have shown that, when phonons are resonant with another signal, there is a strong mixing of modes resulting in hybridization of phonons with the other signal and level repulsion between them (which can open up band gaps). The resonance itself can in turn be tuned by means of a third signal, which is not necessarily at resonance but is coupled to one of the resonant modes. This effect is well illustrated in phonon computing, where the magneto-acoustic phonon computer that we described explicitly relied upon the hybridization of resonant phonons and magnons. With the phonon isolator, however, these resonances were fixed. As such, the phonon isolator was intrinsically a static device; it would do one operation regardless of conditions. The phonon transistor, on the other hand, used a tunable resonance and therefore was dynamically controllable. The same signal at the source of the transistor would not necessarily produce the same signal at the drain. This distinction between the transistor and the isolator is one of the major advantages of dynamical tuning, the ability to respond to changing requirements. Moreover, as the transistor was a nonlinear device, we were able to create a form of dynamical control that allowed for arbitrary logic operations across multiple independent frequencies, thereby opening up a new form of frequency domain parallel computing. This technique exploited multiple tunable resonances and could not be easily reproduced with a stationary device or linear operation. It also constitutes a potential avenue where exploiting the information content of phonon is preferable to other forms of information processing.

From the example of phonon computing, we also see another limitation of the band structure picture of solid-state dynamics. Because the band structure only shows the real part of the dispersion, it is unable to account for losses in the imaginary term. This is crucial when designing practical devices, as losses can affect the stability of an operation. The acoustic Faraday effect, for example, is often described as if circular dichroism does not exist; yet it proved unavoidable in designing realistic gyrators. Even more crucial, though, is the inability of the band structure to present information about the spatial wave functions. While the dispersion illustrates frequency and wave vector (the direction of propagation), it does not represent polarization. But polarization is not negligible, particularly when considering mode mixing as an avenue to breaking degeneracies. The band structures in the Cotton-

Mouton and acoustic Faraday regimes are superficially equivalent yet the transverse acoustic phonons' degeneracies are broken by different forms of symmetry breaking (rotational vs. time-reversal) in these cases. This in turn leads to very different effects of a magneto-acoustic for the same frequency resonance. The ability to tune polarizations or eigenmodes would therefore be a potentially valuable form of tuning beyond the simple band structure picture.

Chapter 4

High Frequency Tuning

In Ch. 1 we demonstrated that a system driven above its resonant frequency will be unable to keep up with the changes imposed by the tuning signal. This can lead to novel phenomena, as the system is unable to relax back to a steady state between changes. It can also produce additional resonances under the correct circumstances (i.e. parametric resonance) or to affect sudden changes to the band structure. These sudden changes can produce scattering (i.e. anharmonic perturbations that mix modes), an effect not seen at lower frequencies. However, because we require high frequencies, these effects are generally just the result of optical couplings, rather than the panoply of couplings we saw in previous chapters. In this chapter we will review parametric driving, ionic Raman as a means of producing non-equilibrium ground states, optomechanical control of phonons, and a means of modeling piecewise-deterministic Markov processes. We will then illustrate these principles with a means of optically tuning the phonon band structure to create opto-phononic switches and the inverse acousto-optic effect.

4.1 Parametric Driving

Back in eq. 1.6 we considered a simple harmonic oscillator driven by an external force. While this is a very common way of driving a system, it is not the only way. An alternative is to vary the parameters of the system by some external driving. This results in a generalization of the simple harmonic oscillator, such as

$$\ddot{u} + f(t)u = 0 \tag{4.1}$$

where $f(t)$ is a periodic function. This is the Hill equation, although a simple change of variables allows us to redefine it as the Floquet equation

$$\dot{\vec{w}} = A(t)\vec{w} \tag{4.2}$$

for periodic $A(t)$ [158]. The Floquet equation is the temporal equivalent of the Bloch equation, both admit solutions of the form

$$w_i(t) = e^{i\Lambda t}\chi(t) \tag{4.3}$$

with periodic function χ and complex eigenvalue Λ. The imaginary part of Λ indicates exponential growth or decay of the solutions. Exponential growth, as always, is a sign of resonance. Unlike in the simple driving picture, parametric resonances can occur at frequencies away from the natural resonance frequency. This can be seen with the special case of the Hill equation

$$\ddot{u} + (\omega_0^2 - 2\Delta\omega^2 \cos 2\Omega t)u = 0 \tag{4.4}$$

which is the Mathieu equation [158]. The Mathieu equation is the specific form generally considered for parametric oscillators, although the Hill equation is also often used [267]. The solutions to the Mathieu equation are (surprisingly enough) Mathieu functions, the properties of which are explained in detail in Abremowitz and Stegun [158]. But if we assume that the perturbation of $\Delta\omega^2$ is small, then we can approximate $u(t)\cos(2\Omega t)$ as $u_0(t)\cos(2\Omega t)$ where u_0 is the solution to the simple harmonic oscillator (eq. 1.6), i.e. $\sin(\omega_0 t + \phi)$ We can

therefore rewrite our equation of motion with this approximation as

$$\ddot{u} + \omega_0^2 u = 2\Delta\omega^2 u_0 \cos(2\Omega t)\sin(\omega_0 t + \phi) \tag{4.5}$$

This is resonant whenever $\cos(2\Omega t)\sin(\omega_0 t)$ has frequency ω_0. Since in general the product of $\cos\phi$ and $\sin\theta$ (or two cosines or two sines) can be expressed in terms of $\cos(\phi \pm \theta)$, our resonance condition for weak parametric driving becomes

$$2\Omega \pm \omega_0 = \omega_0 \tag{4.6}$$

which admits solutions $\Omega = 0, \Omega = \omega_0$. The first solution is the standard driving resonance effect while the second is a parametric resonance. Note that this resonance occurs when the parameter is varied at twice the resonant frequency and is therefore a high frequency driving effect. Using aperiodic functions (e.g. functions of random variables, such as we consider in Ch. 4.4) eliminates these resonances while revealing other high frequency effects.

4.2 Ultrafast Photon-Phonon Effects

4.2.1 Photoinduced Phase Transitions

An aspect of phonon-photon coupling that has recently gained particular prominence is the ionic Raman effect due to its ability to induce transitions to non-equilibrium states. Although this effect was first predicted many years ago by Wallis and Maradudin [268] and Martin and Genzel [269], it was not until Först et al. [270] experimentally confirmed it that ionic Raman became significant. Ionic Raman works similarly to stimulated Raman, where phonons at a particular mode are driven by a coupling with a different, optically driven mode. In stimulated Raman, the optically driven mode is typically electronic, while in ionic Raman the driven mode is infrared phonons. These phonons then anharmonically couple to the Raman modes, which are at a much lower frequency than the infrared phonons. Hence, a photon-phonon resonance in the infrared is used to control low frequency phonons. Specifically,

$$\ddot{u}_I + \omega_I^2 u_I = \frac{e^* E_0}{\sqrt{M_I}} \sin(\omega_I t) F(t) \tag{4.7}$$

$$\ddot{u}_R + \omega_R^2 u_R = A u_I^2 \tag{4.8}$$

where u_I is the infrared mode's displacement, e^* is the effective charge, E_0 the electric field, $F(t)$ the pulse shape, M_I the effective mass, u_R is the Raman mode, and A is the anharmonicity constant. Because the force driving the u_R phonon oscillation is proportional to

$$u_I^2 \propto \sin^2(\omega_I t) \propto (1 - \cos(2\omega_I t)) \approx 1/2 \tag{4.9}$$

the Raman mode will experience a constant force over a timescale of $1/\omega_R \gg 1/\omega_I$. This will cause a finite displacement of the lattice to some new equilibrium position. But because this equilibrium is contingent upon a large enough population of coherent infrared phonons to destabilize the Raman mode's equilibrium, it is an intrinsically non-perturbative, out of thermodynamic equilibrium effect (as shown by Subedi et al. [271]). This means that the new ground state can display properties not found in thermodynamic ground states such as the hidden states of Ichikawa et al. [274] (shown in Fig. 4-1), and so the effect is termed

a photoinduced phase transition. It is also a coherent perturbation and so not same as photoinduced heating producing a thermal phase transition, a much more conventional effect. Not only does that pathway lead to only thermodynamic ground states, but the time-scale involved in that transition is much longer than in the photoinduced transition [272, 273]. Much of the interest in photoinduced phase transitions has been on how this effects the electronic ground states (reviewed in Gamalyn and Rode [272] and Yonemitsu and Nasu [273]), but lattice effects are also interesting. For example, these transitions can change the symmetry of the lattice and thereby change the band structure (as demonstrated by Wall et al. [275, 276]). In addition, while the phase transition is initially athermal, thermal effects are not entirely absent as the system equilibrates. Garl et al. [277] observed a photoinduced thermal expansion of bismuth, which in turn induced a photon fluence dependent red-shift of some of the phonon modes. This deviated from the standard form as the phonons were out of thermal equilibrium with the electrons. The effect was limited, however, by their system melting, as this sort of phonon softening is an expected signature of materials near a structural, thermal phase transition [278]. Indeed, the system's temperature was above the melting point, and it was only in probing the sample on ultrafast time scales (i.e. faster than it can melt and reach equilibrium) that this effect could be isolated. It is also similar to the earlier work of Gump et al. [279] on chalcogenide glasses, where the photosoftening was associated again with the approach of a glass-liquid melting transition.

While ionic Raman is a lattice effect (arising from phonon modes), a similar effect exists in molecules. There are a class of polymers known as photoisomers where the application of optical driving can induce a new ground state. Generally, this is irrelevant to phonon dynamics, but when photoisomers are allowed to crystallize this can yield another avenue to photoinduced phase transitions. This was done with Petr et al. [280] and Verploegen et al. [281] for a crystal composed of liquid crystal elastomers with photoisomer additions. When light was applied, the photoisomers would bend into a new configuration, changing the shape of the elastomer elements and thereby changing the lattice symmetry. This was used to switch the acoustic properties between those of the completely photoexcited and completely relaxed states.

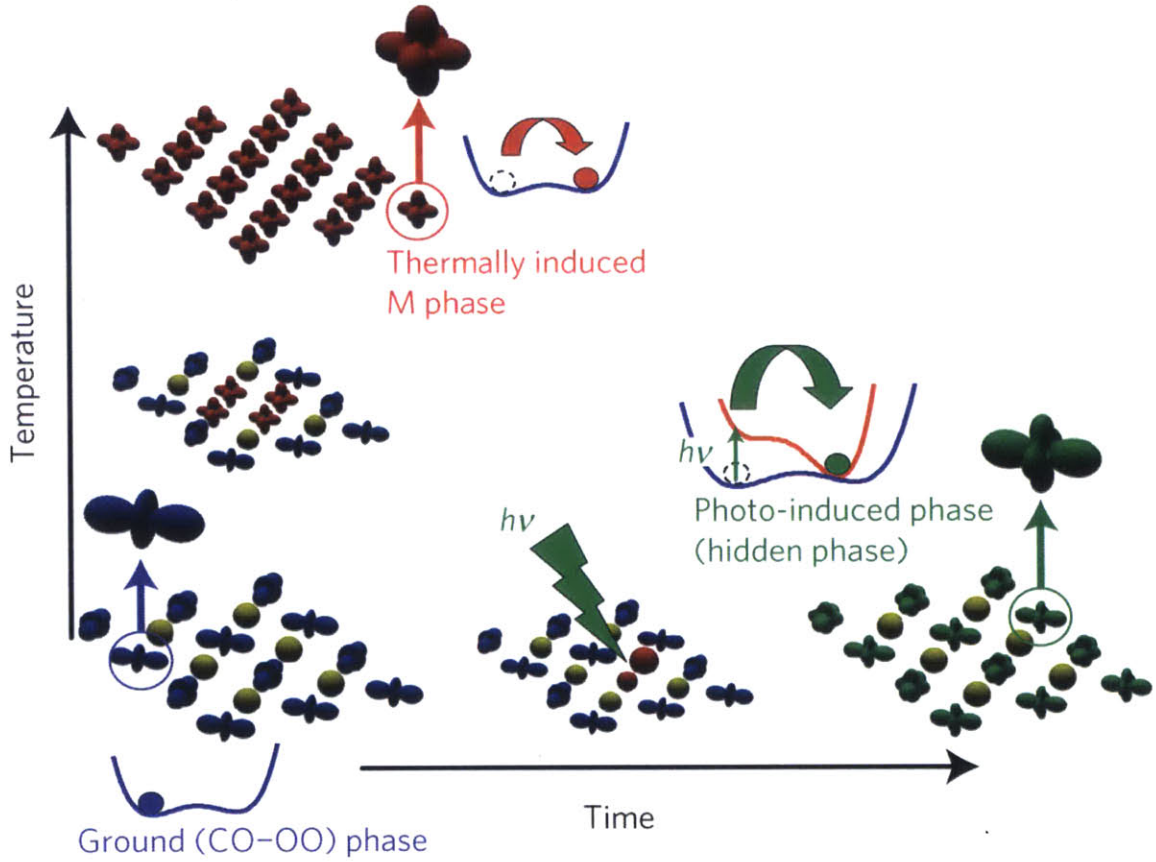

Figure 4-1: Schematic of electronic order of $Nd_{0.5}Sr_{0.5}MnO_3$ for various phases. In the lower left corner is the ground state structure, and above it is the thermodynamic equilibrium phase achieved with raising temperature. To the right is the hidden, non-equilibrium phase achieved with photoexcitation. Intermediate between each of these are unstable intermediate states. Schematic energy diagrams illustrate the nature of these reactions. Note the difference in structure between the equilibrium and non-equilibrium states. Reprinted by permission from Macmillan Publishers Ltd: Nature Materials. H. Ichikawa, S. Nozawa, T. Sato, A. Tomita, K. Ichiyanagi, M. Chollet, L. Guerin, N. Dean, A Cavalleri, S.-I. Adachi, T.-H. Arima, H. Sawa, Y. Ogimoto, M. Nakamura, R. Tamaki, K Miyano, and S.-Y. Koshihara, *Nature. Mater.* **10**, 101-105 (2011). Copyright 2011 [274].

4.2.2 Optomechanics

Even when not in resonance, photons can still couple to phonon modes by means of radiation pressure. Specifically, when photons impinge upon an object, they can scatter and impart momentum to it. This force is the radiation pressure. In elastic scattering the momentum transfer is greatest when photons reverse direction, so the radiation pressure is maximized for a mirror, or more typically a pair of mirrors facing each other. As the mirrors gain momentum they will vibrate (that is, excite phonons) and thereby causing the optical standing wave pattern to change, which feeds back into the radiation pressure experienced by the mirrors. This setup is an optomechanical cavity, one of the most common schematics for optomechanics [1]. The radiation pressure imparts an average force [282]

$$\langle F \rangle = 2\hbar \frac{\omega_{cav}}{L} \langle \hat{a}^\dagger \hat{a} \rangle \tag{4.10}$$

in the formalism of optomechanics ω_{cav} is the cavity optical resonance ($\omega_{cav,m} \approx m\pi c/L$ integer m), L length, and $\hat{a}$ the photon destruction operator. In terms of the Hamiltonian [282, 283]

$$H = \hbar\omega_{cav}\hat{a}^\dagger\hat{a} + \hbar\Omega_m\hat{b}^\dagger\hat{b} \tag{4.11}$$

(where Ω is the phonon mode's frequency and $\hat{b}$ is the phonon destruction operator), the principle effect of radiation pressure is to perturb the length of the cavity and thereby change the optical cavity resonance ω_{cav}. Taylor expanding ω_{cav} in terms of the deviation gives the optomechanical coupling

$$H_{int} = \hbar g_0 \hat{a}^\dagger \hat{a}(\hat{b} + \hat{b}^\dagger). \tag{4.12}$$

This is the fundamental form of the optomechanical interaction, although other forms of this equation have been used (see Aspelmeyer et al. [282] for a review). For photons of much higher frequency than the phonon frequency, the position of the mirror is effectively constant. Changes in the mirror's position will result in effectively instantaneous changes to the optical field, thereby applying a restoring force that can trap the mechanical resonator. While this requires an isolated mechanical resonator as it is analogous to atomic trapping, it can create an effective spring constant that modifies the vibrational frequency for the

[1] In practice the arrangement can be more complicated, but it is typically reducible to an optical cavity with movable mirrors

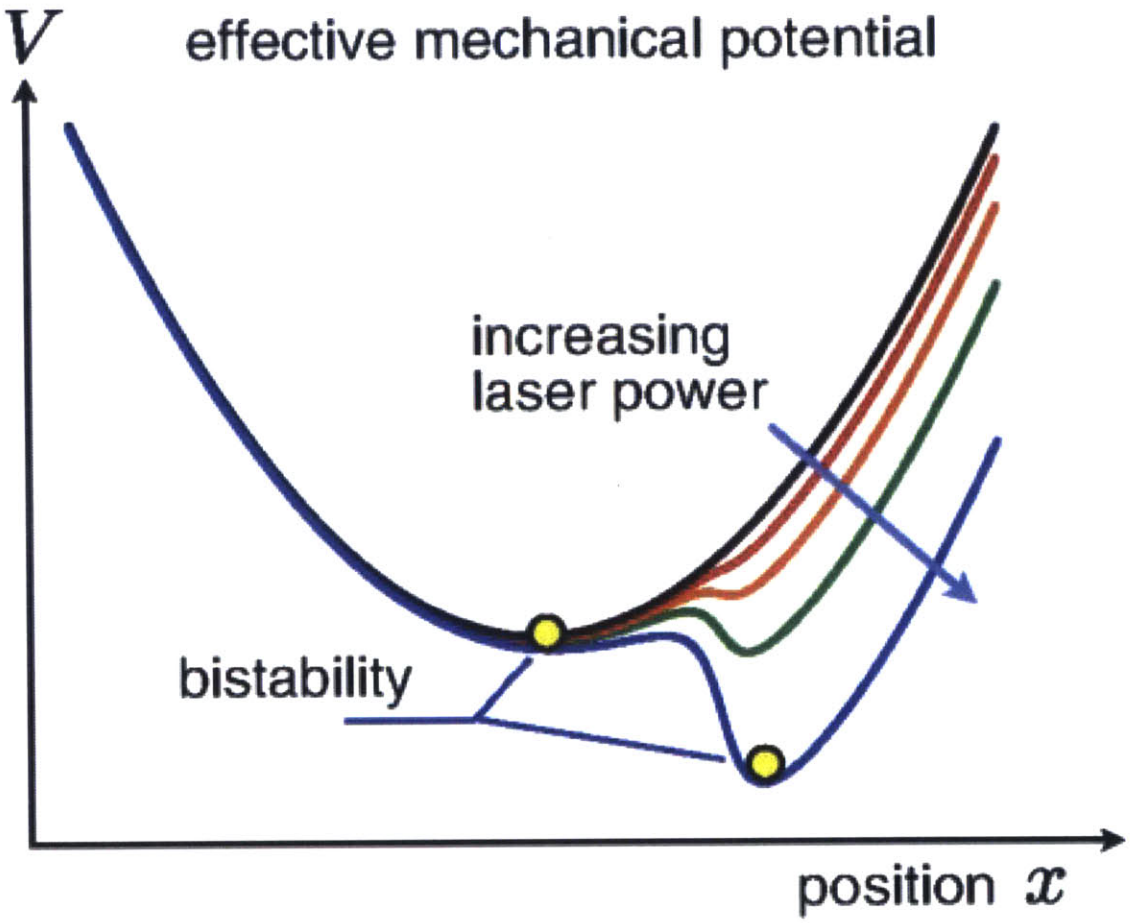

Figure 4-2: Bistability of the optomechanically induced effective mechanical potential. Reprinted figure with permission from M. Aspelmeyer, T. J. Kippenberg, and F. Marquardt, *Rev. Mod. Phys.* **86**, 1391 (2014). Copyright 2014 by the American Physical Society [282].

isolated oscillator [282, 284, 285, 286, 287, 288]. This effect can additionally introduce multiple stable states, leading to bistability or multistability of the isolated oscillator (see Fig. 4-2). More generally, the optical field will introduce a self-energy correction to the band structure.

In addition to this arbitrary frequency effect, additional effects arise when the cavity is driven by frequencies slightly off of cavity, i.e. when $|\omega_L - \omega_{cav}| = |\Delta| = O(\Omega_m)$ (Δ is the detuning). In this regime, Raman scattering will enhance the coupling of different modes and induce normal mode splitting when $\Delta \approx -\Omega_m$ (analogous to the polariton effects explored in Ch. 3.1). When $\Delta \approx 0$, the effect of Raman scattering on phonon self-energy is to shift the frequencies of the discrete mechanical modes (phonons) by a factor approximately linear with

Δ [2]. This is the dynamical form of the optical spring effect. Since it depends upon the laser intensity (i.e. photon density in the cavity) as well as its frequency, tuning the intensity gives rise to additional effects. In particular, parametric oscillations in the intensity can be used to create squeezed phonon modes and test the quantum nature of phonons [282]. Additionally, when multiple distinct phonon modes (i.e. modes of different oscillators or different modes of the same oscillator) are coupled to the same optical field will be indirectly coupled. This effective interaction can be used to entangle phonons [290, 291, 292].

These quantum interactions of phonons led to consideration of phonons in quantum computing architectures. The initial approach was primarily concerned with photonic qubits and only used phononic elements as a form of memory (such as were discussed in Ch. 3.2). Zhu et al. [293] introduced this approach, where they sought to the convert an optical pulse into an acoustic excitation. To do so they relied upon stimulated Brillouin scattering, which is a nonlinear electrostriction process (photon-phonon coupling) induced by an interaction with a second optical signal [3]. The information-bearing optical signal uses a higher frequency than the read/write command-bearing optical signal. The difference between these two frequencies is the excited phonon's frequency. If the information-bearing signal is composed of multiple frequencies, then they will in principle each be converted into phonons without dispersion. Thus a wide spectrum of information may be stored as phonons, although in experiments on optical fibers the highest frequency components of the optical wave packet are lost in the conversion (see Fig. 4-3). Moreover, this technique allows the phononic storage of multiple photonic wave packets within a single optical fiber. However, phonons themselves will also decay exponentially (albeit on a longer time scale than stored photons), and so wave packets could only be stored for intervals shorter than the phonon lifetime (i.e. nanoseconds for their system). In contrast, Safavi-Naeini and Painter [294] and Change et al. [295] developed a different approach. Specifically, they stored information within an optomechanical crystal (also called a phoxonic crystal, a material which is simultaneously a photonic crystal and a phononic crystal) rather than an optical fiber. An optical waveguide is located adjacent to the optomechanical crystal so that as photons traverse the waveguide

[2]The Raman coupling regime is also significant in other contexts and values of Δ because the detuned laser can induce radiative cooling of mechanical motion, which is outside the scope of this work but reviewed in Asplemeyer et al. [282].

[3]Brillouin scattering essentially arises from the same physical interactions as Raman scattering, albeit for a much lower frequency of phonons.

the become coupled to the optomechanical crystal, where their radiation pressure creates a phonon population that contains their information (and can be reversibly converted back into photons) (see Fig. 4-4). Fiore et al. [296] also used radiation pressure, although they relied upon a single optomechanical resonator. The advantage of this approach is that the phonon lifetimes are significantly longer than in Zhu et al. [293]. As in Zhu et al. [293] , the incident photons were detuned from the mechanical resonant frequencies but could be freely converted to or from the mechanical vibration via a second optical signal. Moreover, the frequency of the photons that reads out the stored information did not need to be the same as the frequency of phonons that wrote it. Thus, their storage technique also constituted a photonic frequency converter. The phononic memory achieved here should in principle have been a perfect record of both the amplitude and phase of the incident photons (i.e. their full quantum state), however in practice the thermal background destroyed this coherence in their experiments. This difficulty was resolved by Verhagen et al. [297] using a mechanical resonator that had been cooled to near its quantum ground state. As an example of photonic conversion, they also examined their system as an optical-to-microwave photon translator. Palomaki et al. [298] focused on treating this quantum coherent state transfer protocol in the microwave regime. They used an optical waveguide that was coupled to a superconducting circuit, which in turn was coupled to a mechanical oscillator. Such an indirect coupling scheme facilitated an increased tunability and control of the photon-phonon coupling. Another mixed photon-electron-phonon approach was developed by McGee et al. [299] using a bilayer membrane that was metal on one side and dielectric on the other. The bilayer allowed them to store electrical and optical signals in the phonon modes on different sides of the membrane and in addition to convert between them. Hill et al. [300] combined the optomechanical crystal and waveguide approaches by adding an array of pores to a waveguide. In doing so, they were able to store and convert visible frequency photons. The conversion between photons and phonons was analyzed by Wang and Clerk [301], where it was found classically [282] that the combination of photons at different frequencies will produce low-frequency beats suitable to resonantly excite mechanical vibrations. Finally, Galland et al. [302] provided a theoretical analysis of the feasibility of storing a single phonon in a mechanical resonator.

Stannigel et al. [303] took the photon-phonon interactions used in optomechanical stor-

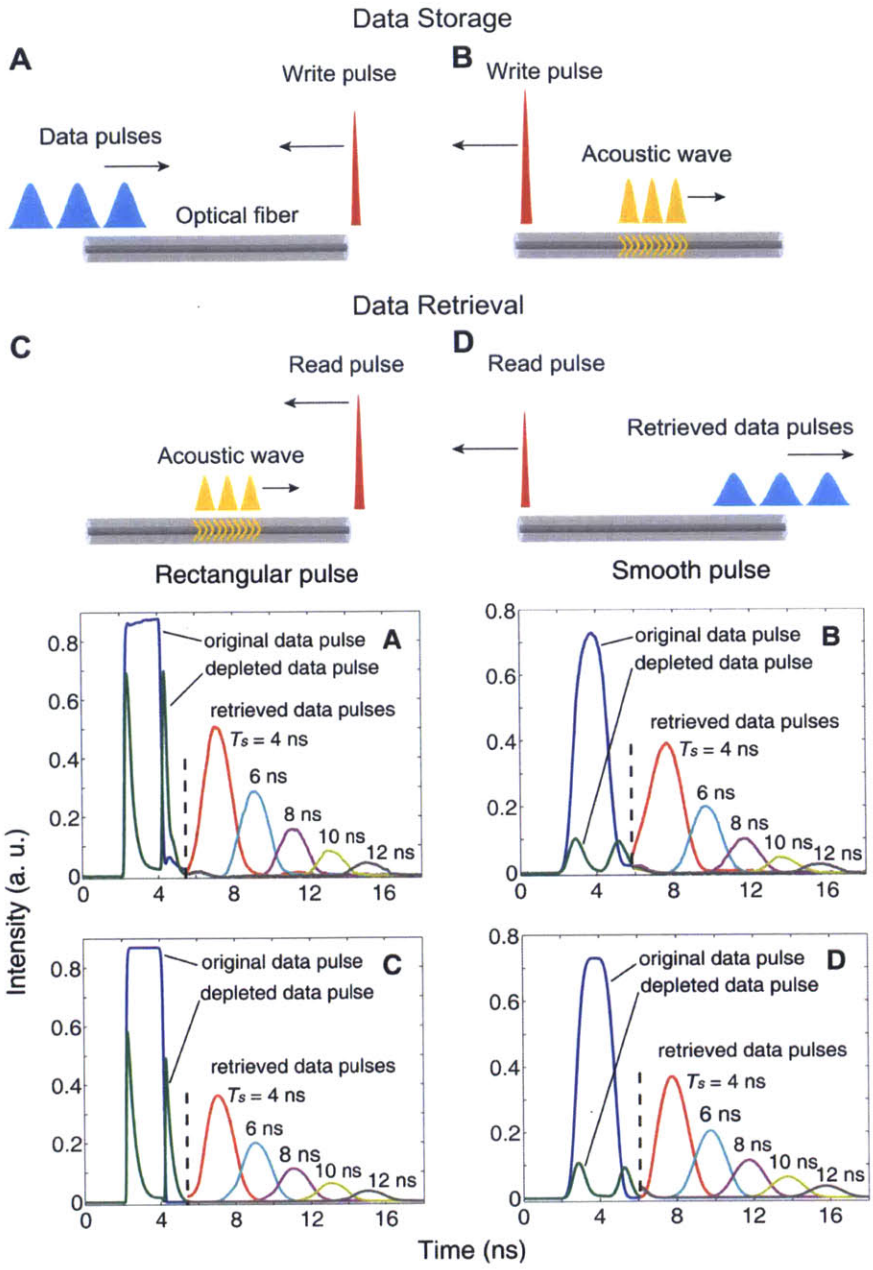

Figure 4-3: Photon storage as phonons via stimulated Brillouin scattering. (top) Schematic diagram of before (A) and after (B) writing and before (C) and after (D) reading. (bottom) Comparison of experiment (A)-(B) vs. theory (C)-(D) for storing and retrieving a rectangular ((A) and (C)) and a smooth ((B) and (D)) pulse. Figure from Z. M. Zhu, D. J. Gauthier, and R. W. Boyd, Science 318, 1748 (2007). Reprinted with permission from AAAS [293].

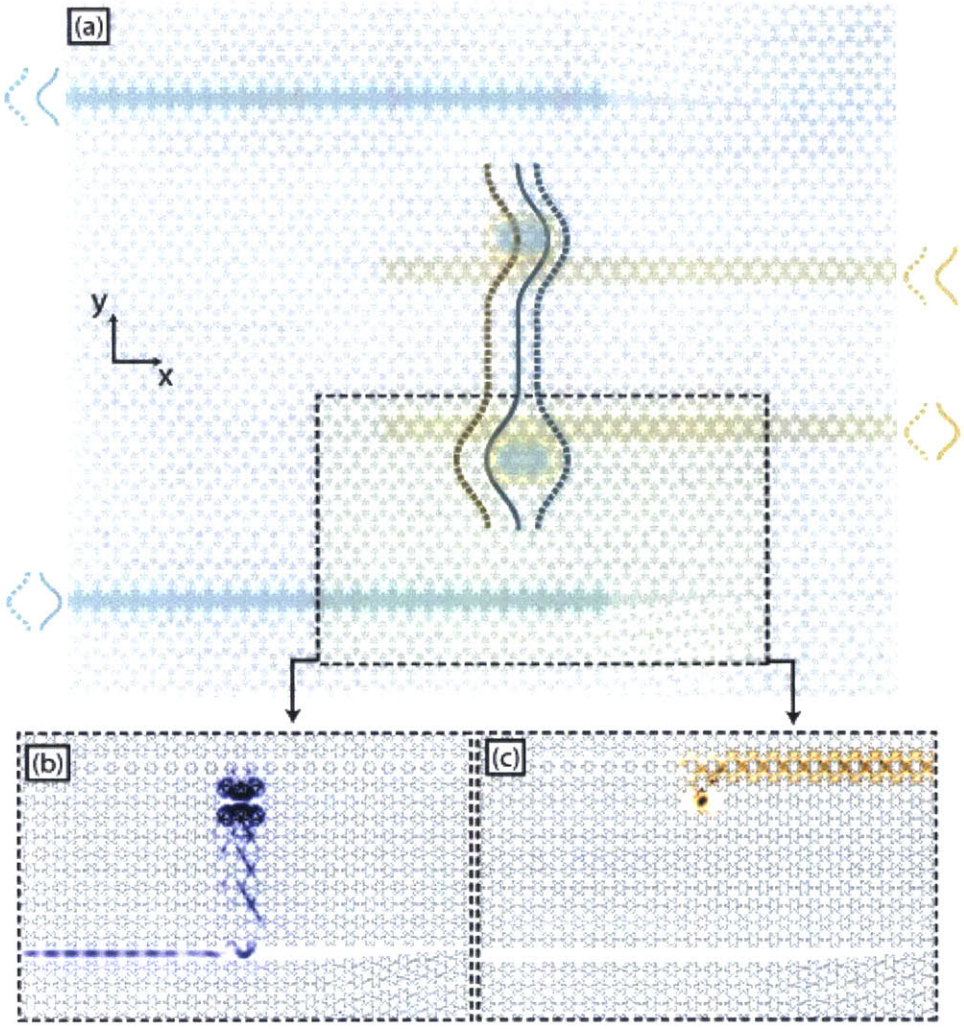

Figure 4-4: Photon storage as phonons within an optomechanical crystal using radiation pressure. (A) Schematic of the phoxonic crystal with photonic waveguides (blue) coupled two phononic waveguides (brown) via simultaneous localization to defect modes. (B) Photonic energy density (Poynting vector). (C) Phononic energy density. Figure from A. H. Safavi-Naeini and O. Painter, "Proposal for an optomechanical traveling wave phonon-photon translator." *New J. Phys.* **13**, 013017 (2011). Available under a Creative Commons Attribution 3.0 license [294].

age and extended them to phononic quantum computing. They used a pair of multimode optomechanical waveguides where low frequency phonons were used for linearly translating between photonic and phononic encodings and high frequency phonons were used to perform nonlinear gate operations on photons. Additionally, they also constructed a photon transistor where the effective photon-photon interaction was mediated via optomechanical coupling to the phonon. More relevant to our focus on phonons, they also studied gate operations between pairs of phonons induced by their mutual coupling to a shared optical mode. Through tuning the photon density (classical amplitude) of the shared optical mode, they were able to tune the nonlinearity of the effective phonon-phonon coupling. Schmidt et al. [304] focused on this last case of phononic storage of information and photon-mediated effective couplings between phonons. They modeled their system as an optomechanical crystal, confining the phonons to cavities composed of localized defects within the crystal. The phonons in these cavities can each be individually addressed by a laser, which constitutes their shared optical coupling. The interaction of the photon and phonon modes yields an effective coupling between phonons addressed by the same laser, where the strength of the interaction can be tuned by (again) controlling the classical amplitude. By varying the combinations of frequencies composing the laser pulse, the effective interaction can have various effects. When the photon frequency equals half the difference of the phonon frequencies

$$H(2\omega = \Omega_1 - \Omega_2) = \hbar J(\hat{b}_2^\dagger \hat{b}_1 + \hat{b}_1^\dagger \hat{b}_2) \tag{4.13}$$

($2\omega = \Omega_i - \Omega_j$ where ω is the optical frequency, Ω_i the phonon frequency of mode i, J the effective phonon-phonon coupling strength, and b the phonon destruction operator), this interaction swaps the phonon populations of two modes. Alternatively, the photon field can entangle pairs of phonons when the optical driving frequency is the average of two phonon modes $2\omega = \Omega_i + \Omega_j$. The resultant Hamiltonian is

$$H(2\omega = \Omega_1 + \Omega_2) = \hbar J(\hat{b}_1 \hat{b}_2 + \hat{b}_1^\dagger \hat{b}_2^\dagger). \tag{4.14}$$

Lastly, when photons and phonons are in resonance ($\omega = \Omega_i$), the optical field will drive the phonons into a squeezed mode via

$$H(\omega = \Omega_j) = \hbar(J/2)(\hat{b}_j^2 + \hat{b}_j^{\dagger 2}). \tag{4.15}$$

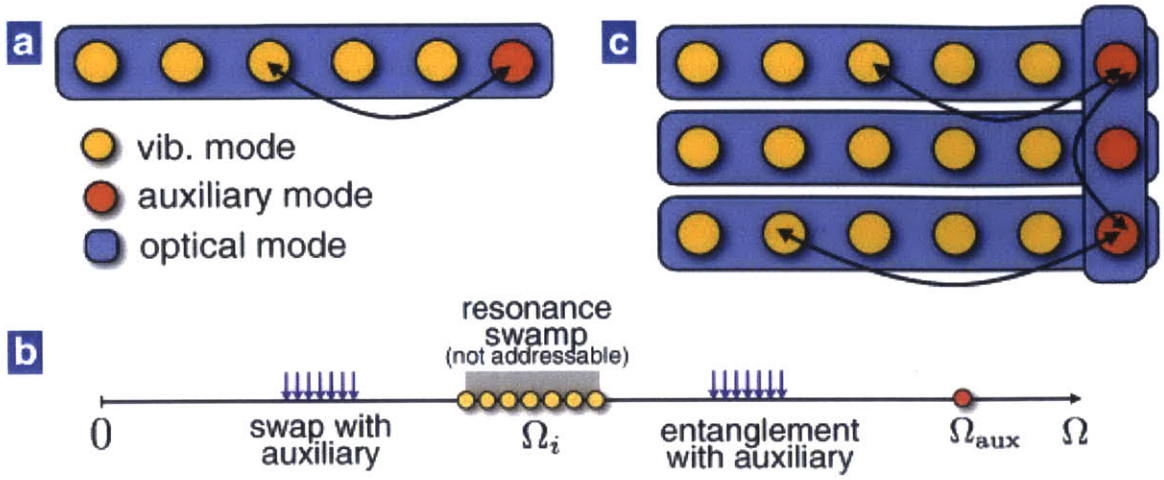

Figure 4-5: Schematic of an optomechanical phononic quantum computing algorithm. (A) Single photonic cavity (blue) with a single directly addressable auxiliary phonon mode (orange) and multiple indirectly accessible phonon modes (yellow). (B) Frequency diagram. Low frequency photons swap populations of between some specific phonon mode and the auxiliary mode, whereas high frequency modes entangle some specific phonon mode with the auxiliary. (C) Protocol to entangle a pair of phonons in different optomechanical cavities. Figure from M. Schmidt, M. Ludwig, and F. Marquardt, "Optomechanical circuits for nanomechanical continuous variable quantum state processing." *New J. Phys.* **14**, 125005 (2012). Available under a Creative Commons Attribution 3.0 license [304].

Because of the flexibility of the possible interactions, the strength of effective photon-phonon coupling has to be sufficiently low as to avoid unwanted operations but also sufficiently his as to prevent the thermalization/decay of the phonons. Although their model is theoretical, they seek to make it easy to experimentally realize (and scale to useful numbers of qubits) by confining the phonon modes intended for memory to a series of well-separated frequency bands and then introducing a set of high frequency auxiliary modes for accessing that memory. To perform an operation like, for example, entangling two storage modes is done by swapping them into the auxiliaries (a low frequency operation), entangling these auxiliaries (a high frequency operation), and then swapping them back to their original modes (see Fig. 4-5).

Rips and Hartmann [305] consider a similar array-based approach to phononic quantum computing. Instead of a phoxonic crystal, though, they use an array of nanobeams resonantly coupled to one photon mode of an optical cavity. Each beam can be also individually electronically controlled through an array of electrodes. They use this array tune the nonlinearity of the beams so as to allow only a single phonon transition to be feasibly induced

by the photon-phonon coupling. As such, each beam can be treated as a two level system and hence can be considered a binary qubit. An arbitrary quantum logic gate can be decomposed into one non-trivial two qubit gate and the basis set of one qubit gates (for example, the Pauli spin basis of $\sigma_x, \sigma_y, \sigma_z$). As such, they construct Pauli spin gates using AC electric fields generated by the electrodes, with V_z generating a σ_z rotation and $V_{x,y}$ generating linear combinations of σ_x, σ_y (decoupled for purely horizontal or vertical fields). For two qubit gates, they use the interaction with the shared photon mode. First, the two specified qubits must be detuned to have a single transition frequency that is distinct from the transition frequencies of the other qubits. As in Schmidt et al. [304], the effective phonon-phonon coupling is mediated via the photon field. The photon field induces hopping between sites, from which they construct a non-trivial two qubit entangling gate – the ISWAP gate. Specifically, the optical coupling generates $\sqrt{\pm\text{ISWAP}}$. To create the ISWAP gate, then, they must apply $\sqrt{\text{ISWAP}}$ between the pair of qubits, then a π rotation about z on the first qubit, $\sqrt{-\text{ISWAP}}$ (i.e. the inverse of the first operation), and finally a $-\pi$ rotation about z on the same qubit. This will entangle the selected pair of phonons but not affect the others.

4.3 Methods: Piecewise-deterministic Markov Processes

Consider an equation of the form

$$L[y(t); t, \tau] = 0 \tag{4.16}$$

where L is a (not necessarily linear) differential operator, $y(t)$ are a set of unknown functions, t is a continuous time variable, and τ is the mean waiting time of some stochastic (i.e. random) process. Crucially, L does not depend upon the history of $y(t)$, just on its current state and so the stochastic process is a Markov process. Given that the random process only occurs at discrete times, we can always define intervals (T_i, T_{i+1}) that obey the relation

$$\langle T_{i+1} - T_i \rangle = \tau. \tag{4.17}$$

For times in these domains (i.e. $t \in (T_i, T_{i+1})$, our equation for $y(t)$ becomes

$$L_D[y(t); t] = 0 \tag{4.18}$$

where L_D is a deterministic functional. This is significant because there are many analytic and computational methods to solve deterministic differential equations. There are also computational algorithms for generating intervals obeying eq. 4.17. Thus, we can solve for $y(t)$ through the simple algorithm of repeatedly finding the time till the next random event, deterministically integrating $y(t)$ to that time, performing the random process, and updating τ. In Ch. 4.4 we will use this algorithm for the specific case of τ characterizing a set of Poisson-distributed processes which depend upon a set of auxiliary functions $z(t)$ (as outlined in Sklan and Grossman [306]). These auxiliary functions are characterized by a mapping $w[y(t; z(t))]$ which transforms the continuous functions $y(t)$ and the discrete auxiliaries $z(t)$ into a a set of discrete states. As such, our entire system can be characterized as moving stochastically and without memory between discrete states, i.e. as a Markov chain. The algorithm for handling a stochastic process of this form is the Gillespie algorithm [307], which we modify slightly to account for the piecewise-deterministic nature of our equation of motion.

For concreteness, let's say that there are N auxiliary variables $z_i(t)$ which can collectively be

used to map N of the $y(t)$ functions to two states (let's call them 0 and 1) via $w[y_i(t; z(t))]$ [4] [5]. There are rate constants r_+ for randomly converting $w[y_i]$ from 0 to 1 and r_- for the reverse. The total rate of conversion from 0 to 1 for the entire system will be

$$R_+ = r_+ N_0/N \tag{4.19}$$

where N_0 is the population of $y_i(t)$ in the 0 state (R_- can be defined similarly). The total rate of stochastic events is therefore

$$R = R_+ + R_- = r_+ \frac{N_0}{N} + r_- \frac{N_1}{N} = (r_+ - r_-)\frac{N_0}{N} + r_- \tag{4.20}$$

since $N_0 + N_1 \equiv N$. With this quantity defined we can now outline the Gillespie algorithm:

1. Initialize the system at $T_i, y(T_i), z(T_i)$ with $i = 0$. Calculate $N_0(T_i), N_1(T_i)$.

2. Calculate $R(T_i)$ using eq. 4.20.

3. Generate a random waiting time from a Poisson distribution by taking a random number from the interval $\eta \in [0, 1]$ and using

$$T_{i+1} = -\ln \eta / R(T_i). \tag{4.21}$$

4. Using the deterministic equation of motion $L_D[y, t; z(T_i)]$, integrate y to T_{i+1} (or to the end of the simulation interval if $T_{end} < T_{i+1}$), update $i = i + 1$.

5. Perform the stochastic step:

   (a) Determine if the stochastic event was to increase or decrease N_0 by generating a

[4] This mapping assumes of each element y depends upon the state of all z. Assuming locality, however, we use the simplified form $w[y_i(t; z_i(t))]$, i.e. that each element of z_i is associated with an element of y.

[5] Note that there can be more than i elements in y, but there is often some particular subset of i elements that is relevant for w. The notation used assumes that this is y is ordered such that these elements come first in the list of y functions. In the event that the list is not ordered in this way, it can be reordered using a linear operator.

new random number $\eta \in [0,1]$

$$\begin{cases} 0 \to 1 & \text{if } \eta < R_+/R \\ 1 \to 0 & \text{if } \eta \geq R_+/R \end{cases} \tag{4.22}$$

(b) Select which element from N_a (a =0 for $0 \to 1$ or 1 for $1 \to 0$) is to be flipped by selecting a random integer $\eta \in (0, N_a]$. Go to that element of the ordered set of auxiliary variables z and switch it to a new state.

6. Update $N_0(T_i), N_1(T_i)$.

7. Go to step 2 if $t < T_{end}$.

This is based upon the standard form of the Gillespie algorithm, which uses $R = R_+ + R_-$ to generate a single waiting time and then determines the identity of the stochastic event. An alternative formulation would be to generate multiple waiting times for each class of stochastic event (i.e. to generate $T^{\pm}_{i+1} = -\ln \eta_{\pm}/R_{\pm}$) and then use whichever is smaller. For stationary equations for $R_{\pm}$, such as we considered above, these approaches are equivalent. When this is not the case (particularly when the two rate constants vary with different time scales), the alternative formulation is preferable.

4.4 Phonon Transport in Photoswitchable Lattices

Photon-phonon interactions, as we have seen, can have a variety of effects and applications. In general, however, the focus in developing photon-phonon coupling techniques has not been to tune phonon transport. For example, ionic Raman scattering has been used control electronic properties more than phononic [272, 308, 309]. For purely coupling photons and phonons, the focus in optomechanics has principally been the conversion phonons to photons and vice versa [310, 311], as have the related phenomena of Raman scattering [312, 313], vibronic scattering [314], and black-body radiation [313]. This can be thought of as changing occupancies of different modes but not changing the properties of those modes. On the other hand, when the possibility of using photon-phonon interactions in non-resonant tuning has been studied, the focus was the use of phonons to change the index of refraction (as in acousto-optics [315, 316, 317]). Those times that the photonic tuning of phonons has been considered, it has been limited to phonon polariton resonances (discussed in Ch. 3.1.1), modification of localized phonons' spring constant [282, 284, 285, 286, 287, 288], phonon state preparation (discussed in Ch. 4.2.2), the onset of melting transitions [277, 279], or switching between two discrete states (fully illuminated or no illumination) [280, 281, 318]. The most basic forms of tuning, the modification of the speed of sound or phonon transmission as functions of optical driving, have not been considered for traveling waves [306]. This is an important aspect of tuning, as a continuous response to a changing variable is more flexible than the discrete responses of Refs. [280, 281, 318]. In particular, just as the use of Brillouin scattering [315, 316, 317] allowed for the creation of acousto-optic filters and modulators, demonstrating this sort of tunability would constitute an inverse acousto-optic effect. This sort of opto-phononic tuning would therefore be outside of the existing framework of light-matter interactions (i.e. not just a change of population levels or a tuning of photonic transport), as summarized in Table 4.1

In this section we examine one approach to this form of tuning. We specifically seek to control the speed of sound c_s via optical intensity. To accomplish this, we shall consider a toy model[6] of an array of generic photoswitches and use it to modulate the phonon band structure,

[6]That is, a simplified model which focuses more upon understanding an effect than modeling a specific system. However, to the extent that this model can be applied to a variety of systems, this simplicity gives it added generality.

	Create/Destroy	Harden/Soften
Photon→Phonon	Optomechanics, Raman	???
Phonon→Photon	Vibronic, Fluorescence	Acousto-Optics

Table 4.1: The quadrants of light-matter interaction. First row is photons used to control phonons, second is phonons used to control photons. First column is changing populations, second is tuning dispersion. Reprinted table with permission from S. R. Sklan and J. C. Grossman, *Phys. Rev. B*, **92**, 165107 (2015). Copyright 2015 by the American Physical Society [306].

thereby tuning c_s. In addition, we shall show numerically that additional effects arise at high frequencies, particularly phonon confinement which may be useful for vibrational energy storage or phononic transistors (see Ch. 3.2).

To begin, let us consider a solid under illumination – there should be three distinct photon-phonon coupling mechanisms. If material is composed of polar atoms of molecules, then localized vibrations will induce fluctuations in the polarization that will in turn create a coupling to the electromagnetic field (this is direct Raman, the inverse process of varying electromagnetic fields inducing localized vibrations is also possible). Alternatively, if the material has an infrared-active phonon mode, then photons can excite that mode directly and thereby anharmonically drive other modes (this is ionic Raman, see Ch. 4.2.1). If neither of these coupling mechanisms is present, photon-phonon couplings can still exist as light can also excite electrons, which then excite phonons via electron-phonon coupling (this is indirect or stimulated Raman). Subsequent to the initial excitation of a single phonon mode, nonlinearities (typically electron-phonon coupling or phonon anharmonicity) will eventually disperse this energy into a thermal phonon population. For some materials, the excitation of a coherent phonon population can also induce a structural change (as in Ch. 4.2.1), particularly by inducing oscillations about some new equilibrium position in ionic Raman or softening some phonon mode in stimulated Raman. These structural changes must necessarily change the phonon band structure, although these changes are not necessarily large. To distinguish the creation of thermalized phonons and the tuning of the band structure (effects which are clearly distinct for sufficiently weak phonon anharmonicity, [7]), we

[7]Thermalization and velocity modulation are distinct effects given a lattice of no more than weak nonlinearity. To illustrate this, consider a phonon current of the form $J = \Sigma n_i v_i$, Thermalization changes occupancy and hence perturbs phonons n_i, whereas structural changes will tune the velocity v_i. It is only if anharmonicity is so strong that the band structure is intensity dependent that this distinction breaks down. And even in this highly anharmonic regime, the use of sufficiently low amplitude acoustic excitations or low temperatures makes this negligible.

concentrate on the non-photoactive modes and neglect thermalization except for its effect in structural transitions. For consistency, this entails neglecting phonon-phonon couplings and so we must restrict our attention to harmonic phonons. Ergo we can henceforward confine our attention to a one-dimensional chain of simple harmonic oscillators (SHOs) without any further loss of generality.

Given this assumption, we model our system as n masses ($m \equiv 1$) joined to $N = n + 1$ photoswitcheable SHOs (with a ground state spring constant of K_D, and an excited state spring constant of K_U) subject to a mechanical driving force $F = F_0 \cos(\omega_0 t)$ at frequency ω_0 applied to the first site along the photoswitchable chain. The mechanical driving is equivalent to pumping a constant supply of energy into the system, so to prevent unrealistically large excitations it is helpful to use a modified form of the standard clamped boundary conditions ($u_0 = 0 = u_n$, where u is displacement) by sandwiching this system between impedance matched systems of n damped (damping rate $\gamma_u \equiv 1$) SHOs ($K = K_D$) and then clamping these ends (shown in Fig. 4-6). For generality, we consider the photoexcitation of any spring to be a localized event that does not induce switching elsewhere (i.e. there are no cascades). This is a plausible assumption for sufficiently separated photoisomers as well as for composite or multilayered structures where only some portion is photosensitive (see the bottom of Fig. 4-6). However, if there are no cascades to drive collective dynamics, then the order and timing of the excitations and de-excitations can have non-trivial impact upon the phonon dynamics. To avoid a biased pattern of excitations, we assume that the switching is randomized with Poisson statistics (an excitation rate of $R_D = B_{DU}H$ and a de-excitation rate of $R_U = A_{spont} + B_{UD}H$, where H is the photon fluence at a point and A and B are the Einstein coefficients [313]). Such an assumption is most rigorous under conditions of sufficiently low intensity photoexcitation where the photon's shot noise dominates (i.e. individual photon trajectories are relevant and we are not dealing with an ensemble of photons) but this assumption is also a technique for ensuring the robustness of the response to deviations in the switching order. The dynamics of an individual photoswitching event is typically complicated, but because the photoexcitation is much faster than any structural rearrangement, these complexities can be neglected (to lowest order) by integrating out the shorter time-scales to give the approximation

$$\dot{K}(t) = -\gamma_K(K(t) - K_{SS}(w)) \tag{4.23}$$

where γ_K determines the rate of the structural reaction (typically $O(\omega_0)$) and K_{SS} is the new steady state, w denotes the stochastic variable describing switching [8]. In principle the equilibrium position of the lattice sites could also change. However, because our system models a photoswitch embedded inside of a matrix and does not address the (realization-specific) dynamics of phonons with wavelengths shorter than one supercell, these shifts are negligible. Hence, the displacement obeys

$$\ddot{u}_i(t) = K_i(t)\left[u_{i-1}(t) - u_i(t)\right] + K_{i+1}(t)\left[u_{i+1}(t) - u_i(t)\right] \tag{4.24}$$

where i indexes the site (note the similarity to eq. 1.1 except that now $K(t)$ is a parametric function, as discussed in Ch. 4.1).

In the steady state the probability distribution of this system's eigenmodes is exactly solvable using Random Matrix Theory [319]. However, we are interested in the dynamics of this system and RMT does not describe the effects of changing composition (i.e. traversing the RMT's solution space [9]). Moreover, the eigenfunctions for a single index in eq. 4.24 can be solved exactly – exponential wave functions when no switching is occurring and modified Bessel functions of imaginary order[10] when switching is occurring – but the inconsistency of this basis set impedes an analytic solution for any non-trivial realization. As such, we focus on integrating the solutions numerically. The switching times and locations

[8] This switching model neglects some of the details found in real photoswitchable materials, but it is close enough to capture the nature of the perturbation upon the phonon dynamics

[9] Changing compositions is also equivalent to traversing different realizations of a glassy or disordered medium or to taking an ensemble average over disorder.

[10] Inserting the solution for $K(t)$ into the differential equation of an isolated harmonic oscillator gives

$$\ddot{u} = -\left[K_{ss} + (K_0 - K_{ss})e^{-\gamma_K t}\right] u \tag{4.25}$$

where K_{ss} is the steady state value of $K(t)$, K_0 its initial value, and γ_K its rate of switching. Making a change of variable $\xi = 2e^{-\gamma_K t/2}\sqrt{|K_0 - K_{ss}|}/\gamma_K$ and $\psi(\xi) = u(t)$ gives

$$\xi^2\psi'' + \xi\psi' + \left(\pm\xi^2 - (i\alpha)^2\right)\psi = 0 \tag{4.26}$$

where $\alpha = 2\sqrt{K_{ss}}/\gamma_K$ and the sign of $\pm$ is given by the sign of $(K_0 - K_{ss})$. This is the Bessel equation (or modified Bessel equation for the negative root). We can solve for the different cases of possible signs of $\pm$ and whether or not α is an integer to get the basis functions

$$\psi = \begin{cases} J_{i\alpha}(\xi), Y_{i\alpha}(\xi) & +, \alpha \in \mathbb{N} \\ J_{i\alpha}(\xi), J_{-i\alpha}(\xi) & +, \alpha \notin \mathbb{N} \\ I_{i\alpha}(\xi), K_{i\alpha}(\xi) & -, \alpha \in \mathbb{N} \\ I_{i\alpha}(\xi), I_{-i\alpha}(\xi) & -, \alpha \notin \mathbb{N} \end{cases}. \tag{4.27}$$

A similar change of variables is used for each i in eq. 4.24

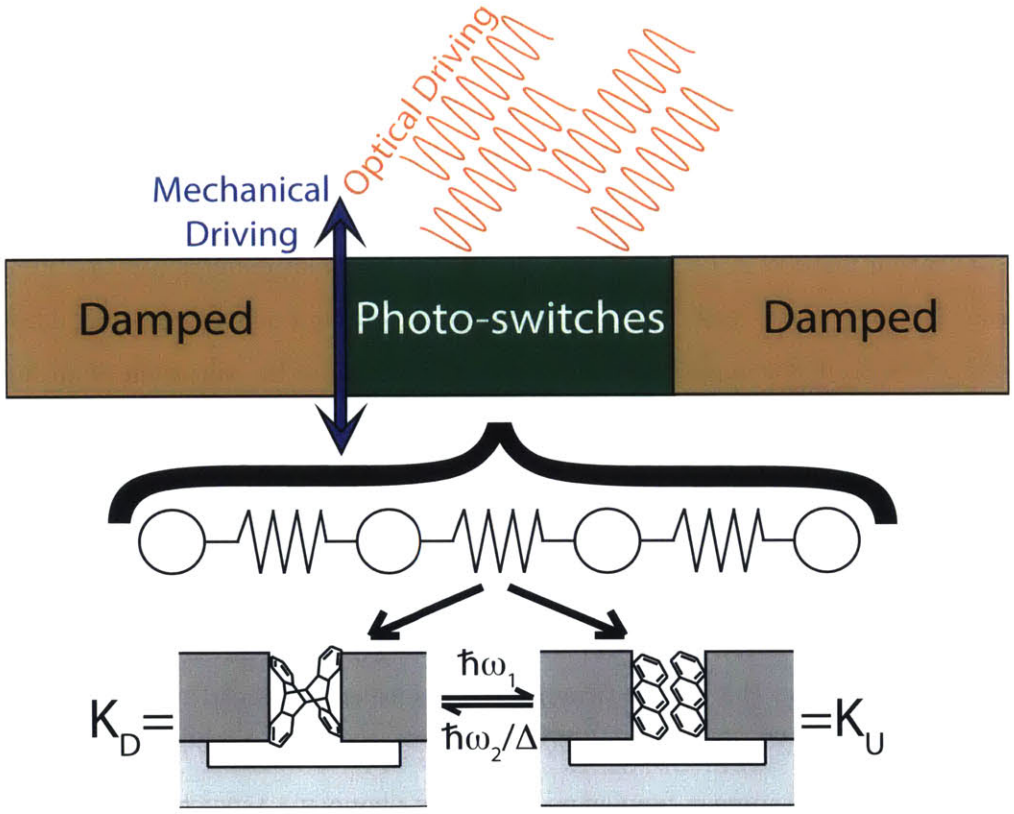

Figure 4-6: Schematic of photoswitchable tuning setup. Photoswitches (green) are sandwiched between two damped regions (brown) that are clamped at the far ends. Photons (orange curves) drive the photoswitches, which are also driven mechanically (blue arrow) from one side to produce phonons. Photoswitches are modeled as a series of one-dimensional SHOs composed of a photosensitive material (e.g. anthracene, see bottom) embedded in a matrix, creating a bistable system with two spring constants. Reprinted figure with permission from S. R. Sklan and J. C. Grossman, *Phys. Rev. B*, **92**, 165107 (2015). Copyright 2015 by the American Physical Society [306].

are stochastic variables and so are computed using the Gillespie algorithm [307], with the system deterministically evolving between these switchings (see Ch. 4.3). The initial conditions are $u(x,0) = 0 = \dot{u}(x,0)$, $K_i(0) = K_D$. We use the following natural units: a the equilibrium site separation is the natural length scale and $t_\gamma = 1/\gamma_u$ for is our time scale. Using $K_D = 1/t_\gamma^2, K_U = 2/t_\gamma^2, R_U = 1.5/t_\gamma, R_D = 2/t_\gamma, F_0 = 1a/t_\gamma^2$, a sample of size n =29 ($N = 30$) is calculated for interval $T = 100t_\gamma$ giving $u(x,t)$ and $k(x,t)$ at various ω_0.

Because the dynamics of $u(x,t)$ is greatly influenced by the evolution of $K(x,t)$, plotting them simultaneously is integral to understanding $u(x,t)$. To make this pair of three-dimensional functions intelligible through a single two-dimensional plot, we turn to an unusual visualization method in Figs. 4-7, 4-8, and 4-9. The x-axis denotes position along the chain (from 0 to N), the y-axis denotes time, colored contours denote constant amplitude isoval lines of the oscillator amplitude u, and rectangles denote the variation of spring constants K (grey = ground state, white = excited [11]). As this plotting technique is rather rarified, Fig. 4-7 includes a supplement of two subplots [12]. The bottom subplot displays the evolution of a site, i.e. $u(i,t)$ and $K(i \pm 1, t)$ for fixed position i. The side subplot displays a single snapshot, i.e. $u(x,t_0)$ and $K(x,t_0)$ for fixed time t_0. As this is snapshot is sufficiently early in our simulation, the mechanical driving from $x = 0$ has not yet had time to propagated along the lattice (leaving the displacement ahead of the wavefront in its initial condition). Given that at low frequencies (as in Fig. 4-7) we expect wavelengths $\lambda \gg a$, the material will appear homogeneous to the phonons. As such, we see switching merely serves as a weak perturbation which distorts then envelope of u. For shorter wavelengths (Fig. 4-8) on the order of $\lambda \gtrsim a$, on the other hand, the solutions become quite sensitive to the composition of K and may be scattered by changes of K (reflecting incident phonons from the boundary between lattice compositions). Given our stochastic driving, the composition of K fluctuates, resulting in intervals of strong transmission or reflection. To the extent that these intervals are controllable, this represents an alternative method of ultrafast optical control of thermal conductivity for phonons in this frequency rage. For even higher frequencies (Fig. 4-9) in this wavelength range, the driving signal lies above the band edge of one state but not the other (i.e. above $\omega_{\min}(K_{\max}) \equiv \omega_g = 2/t_\gamma$). Phonons in

[11] Gradiations and shadings between the grey and white blocks is indicative of a transition state

[12] The supplementary materials of Sklan and Grossman [306] contains movies of lattice dynamics of Figs. 4-7, 4-8, and 4-9 as an alternative visualization scheme.

this regime exponentially decay (i.e. tunnel) when propagating along springs in one state but propagate without loss in the other. For this frequency regime, changing composition of K allows phonons to be confined as standing waves and so could potentially store or dynamically steer vibrations. This trapping has the potential to construct phononic memory or phononic switch (an indirect phononic transistor in the parlance of Ch. 3.2). Lastly, for frequencies in the band gap of both configurations ($\omega > 2\sqrt{2}/t_\gamma$, not shown), no propagation as phonons decay regardless of lattice composition.

From Figs. 4-7, 4-8, and 4-9, we can see that that photoswitching has a large impact upon the transmission and dynamics of $u(x,t;\omega_0)$. To understand the effect of photoswitching upon c_s, however, we must examine the dispersion $\omega(q)$. This can be done by Fourier transforming $u(x,t)$ to get $u(q,\omega)$, where the maxima of $u(q,\omega)$ occurs at $\omega(q)$ (the dominant mode excited by driving at ω_0). (To approximate the smooth dispersion of an infinite lattice using the calculated discrete normal modes of a finite lattice, n =124 is used.) For each ω_0, the calculation of $\omega(q)$ is repeated for N_{rep} =10 times over an interval of $T = 200t_\gamma$ to ensure ergodicity, and ω and q are averaged [13]. However, this method also introduces artifacts that need to be corrected for. Because high frequency driving produces phonons that are often narrowly confined, there will be artificial Fourier components introduced near the Γ point (i.e. $q \approx 0 \approx \omega$). Since these components are not a property of the phonons themselves, but rather of their confinement, we exclude these terms from the average even when they become the dominant peak. By repeating the calculation of the average $\langle\omega(q;\omega_0)\rangle$ phonon excitation for multiple driving frequencies ω_0, we can create the full dispersion relation, the calculation of which is then repeated for various combinations of R_U/R_D in Fig. 4-10 (which illustrates the dependence of the dispersion upon optical driving). Note that, when confinement effects are particularly strong (i.e. for weak driving), the dispersion relation will display a pronounced drop in q as ω rises above ω_g (i.e. enters the confinement regime). This is an artifact of the exponentially decaying tails that border the standing wave domains, as these lower the effective wavelength. Thus, this jump in q is an implication of limited applicability of a defined wavelength in a highly heterogeneous system. Ergo, in fitting the dispersion $\omega(q;R_U/R_D)$ to a sine curve $c_{s,eff}\sin(a_{eff}q)/a_{eff}$ (the dispersion for a homogeneous 1D chain, $c_{s,eff}$ and a_{eff} are fitting parameters) we see that excluding this

[13]Increasing N_{rep} is the same as increasing T for an ergodic system. This combination was selected to aid visualization and to keep computation times manageable.

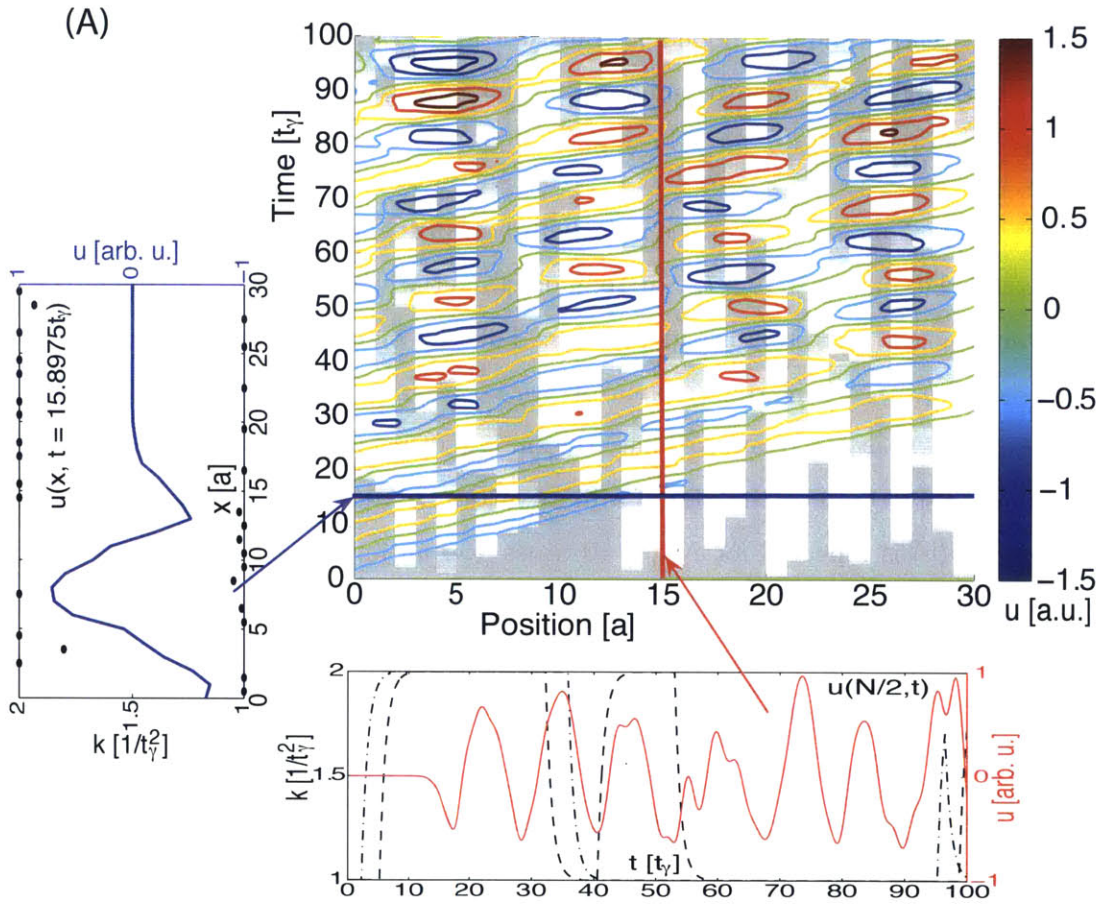

Figure 4-7: Simulation of phonon and spring constant dynamics under photoswitching. The $x-$axis indicates the distance along the one-dimensional chain while the $y-$axis indicates time. Colored contour lines are isoval curves of constant phonon amplitude $u_i(t)$ (magnitude indicated in the sidebar). The grey segments denote the ground state (no illumination, $K = K_D$), white segments denote the excited state (illuminated, $K = K_U$), and the gradients denote the transition states. (a) Low frequency phonon driving ($\omega = 0.5/t_\gamma$). The bottom inset (red, vertical slice) shows $u(N/2, t)$ (red, solid curve) and $K(N/2, t), K(N/2+1, t)$ (black, dashed curves) as functions of time. The side inset (blue, horizontal slice) shows a snapshot $u(x, t_0)$ (blue, solid curve) and $K(x, t_0)$ (black dots) as functions of position. Reprinted figure with permission from S. R. Sklan and J. C. Grossman, *Phys. Rev. B*, **92**, 165107 (2015). Copyright 2015 by the American Physical Society [306].

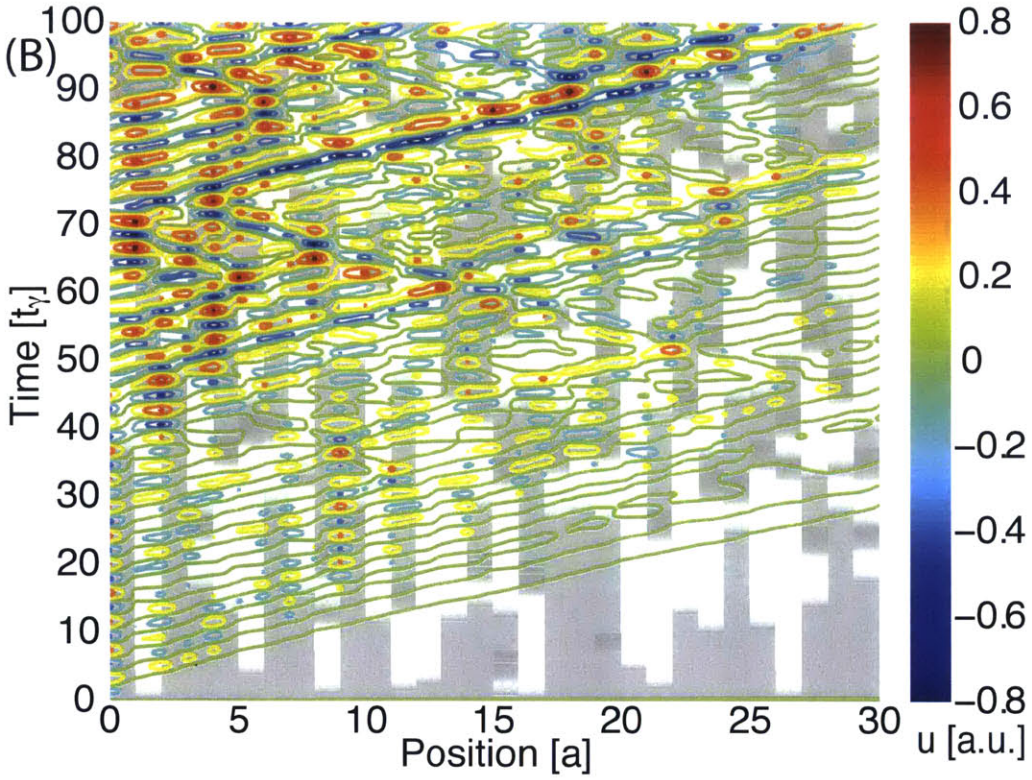

Figure 4-8: Simulation of phonon and spring constant dynamics under photoswitching. Conventions same as Fig. 4-7 (b) Mid frequency phonon driving ($\omega = 1.5/t_\gamma$). Reprinted figure with permission from S. R. Sklan and J. C. Grossman, *Phys. Rev. B*, **92**, 165107 (2015). Copyright 2015 by the American Physical Society [306].

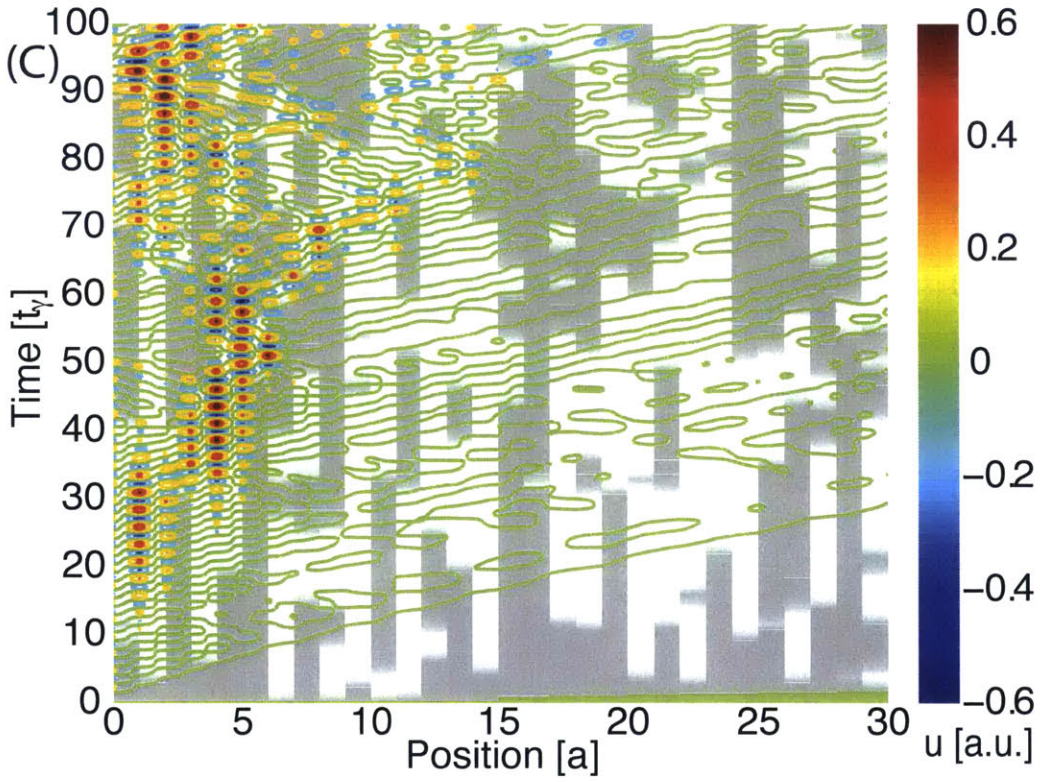

Figure 4-9: Simulation of phonon and spring constant dynamics under photoswitching. Conventions same as Fig. 4-7 (c) High frequency phonon driving ($\omega = 2.5/t_\gamma$). Reprinted figure with permission from S. R. Sklan and J. C. Grossman, *Phys. Rev. B*, **92**, 165107 (2015). Copyright 2015 by the American Physical Society [306].

points produces a more physical dispersion.

These fitted dispersions allow us to extract the effective speed of sound as a function of composition $c_{s,eff}(N_U/N)$ by Taylor expanding the dispersion for small q to get (in units of a/t_γ)

$$c_{s,eff} = 0.997 + 0.177 N_U/N + 0.227\,(N_U/N)^2 \tag{4.28}$$

(where N_U is the excited state's population, and for reference the ground state has a speed of sound $c_{s,D} = 1a/t_\gamma$ while the excited state has speed of sound $c_{s,U} = \sqrt{2}a/t_\gamma$ (see Fig. 4-10 inset)). Using the master equation

$$\dot{N}_D = -R_D N_D + R_U N_U \tag{4.29a}$$

$$\dot{N}_U = +R_D N_D - R_U N_U \tag{4.29b}$$

and setting $\dot{N}_U = 0 = \dot{N}_D$ gives the steady state composition

$$\frac{N_U}{N} = \frac{R_D}{R_D + R_U} = \frac{(g_U/g_D)H}{S(\omega_\nu) + (1 + g_U/g_U)H} \tag{4.30}$$

where $g_{U,D}$ are the degeneracies of the two states, $S = 2\hbar\omega_\nu^3/\pi c^3$, and ω_ν is the photon frequency (last relation comes from detailed balance of the Einstein coefficients [313]). Varying R_U/R_D controls N_U/N_D, so increasing the optical intensity increases the equilibrium population in the excited state (up to some limiting fraction given by the mode degeneracies, although fluctuations about the equilibrium value can result in transient states with even higher populations in the excited state). Hence, tuning the intensity of the illumination gives direct control of c_s, as desired for an inverse acousto-optic effect.

To understand the nature of this control, consider a simple kinetic model of phonon propagation, where c_s in the ground (excited) state is $c_{s,D}$ ($c_{s,U}$). For kinetic transport in an inhomogeneous system, the average speed would simply be the weighted average $c_{s,D}N_D/N + c_{s,U}N_U/N$ or

$$c_s^{(kin)} = c_{s,D} + (c_{s,U} - c_{s,D})N_U/N \tag{4.31}$$

i.e. linear with composition. This model differs from the relation we observed in eq. 4.28, which falls below this kinetic limit except for the homogeneous cases of $N_U/N = 0$ or 1 where both models recapitulate the analytic result of a homogeneous lattice to within 99%

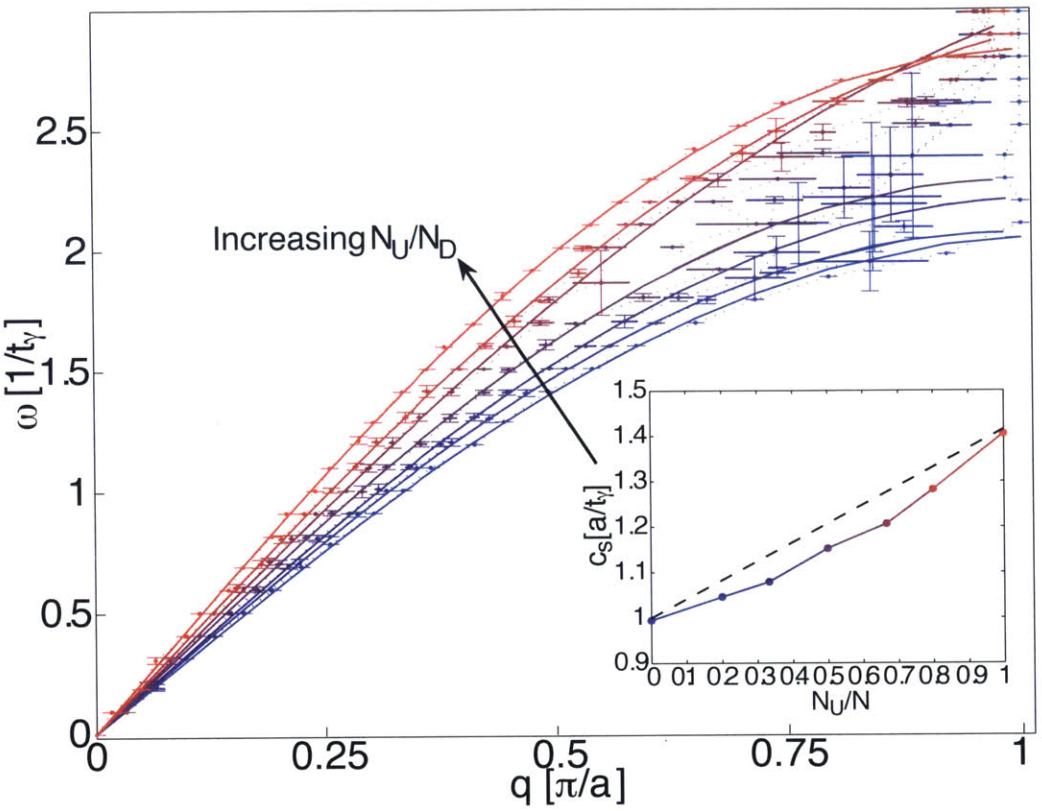

Figure 4-10: The dispersion relation $\omega(q)$ for a one-dimensional photoswitchable chain. Color indicates the illumination intensity rising from blue (a state of no illumination and all springs in their ground state) through red (a state full illumination and all springs in their excited state). The dots with error bars denote raw numerical results (dotted lines between them are a guide for the eye). Conversely, solid lines indicate the numerical fitted sinusoid dispersion relation. (inset) The speed of sound as a function of fraction of the chain in the photoexcited configuration. Colored, solid line denotes results derived from the numerically fitted dispersions (color corresponds to dispersion relation's color) while the black, dashed line denotes the analytic result predicted by a simple kinetic model. Reprinted figure with permission from S. R. Sklan and J. C. Grossman, *Phys. Rev. B*, **92**, 165107 (2015). Copyright 2015 by the American Physical Society [306].

accuracy (see Fig. 4-10 inset). This deviation is expected, though, as scattering at the interfaces will delay a pulse and thereby decrease its effective velocity.

Finally, let us return our attention to the confined regime. For the homogeneous cases the transmittivity of a sufficiently thick sample should be nearly 1 (i.e. no loss, driving frequency is below the band edge) or 0 (i.e. perfect damping, driving frequency is above the band edge). Switching between these homogeneous compositions (which possible when $g_U \gg g_D$ and photon intensity is large, or stochastically plausible for $R_D > R_U$ and $N \approx g_U/g_D$) results in photoillumination controlled switching between discrete states of transmission and reflection. Dynamically changing R_D/R_U therefore results in switchable controlled phonon transmission. This tuning mechanism constitutes a phonon switch and is therefore a potential phononic transistor using the optical analog indirect control scheme presented in [256] (i.e. a light source instead replaces the electromagnet). This form of indirect transistor is more easily tuned than the direct designs, which as discussed in Ch. 3.2 rely upon phonon-phonon couplings [186] that are difficult to control. To demonstrate this proposal's feasibility, we repeat our simulations of the lattice dynamics, this time using a pulsed illumination ($R_D^{(on)} = 4/t_\gamma, R_D^{(off)} = 0$). As mentioned in Ch. 4.3, this requires a slightly different form of the Gillespie algorithm [307], as the rates in the illuminated and dark intervals are not comparable [14]. We select pulse widths such that a homogeneous composition is likely to be achieved for each illumination state. Since complete, monotonic switching of a sample has the expectation value

$$R_{U,D}\tau_{U,D}^{(N)} = N\sum_{1}^{N}\frac{1}{v} = NH_N \approx N\ln N \tag{4.32}$$

where H_N is the harmonic function, we use a sample size of n =9 for these simulations (illumination period $200t_\gamma$, dark period $200t_\gamma$, total run time $2000t_\gamma$, $R_D = 4/t_\gamma = 8R_U$). In Fig. 4-11 we illustrate the switching dynamics by plotting the amplitude at the far end of the sample (normalizing it to the maximum amplitude at the far end that is achieved without damping $\max[u_0(L,t)]$) for a driving frequency of $\omega = 2.1/\tau_\gamma$. The horizontal lines

[14] In particular, the case of the calculated time to the next photoexcitation being longer than the remainder of the illuminated interval requires special attention. Given the ergodicity of photoexcitations, we chose to translate this waiting time ahead by the T_{dark}, but other methods are possible for this literal edge case. Similar concerns also exist near the start of the illuminated interval, although that can be accounted for by recalculating the rates at the times of changing illumination.

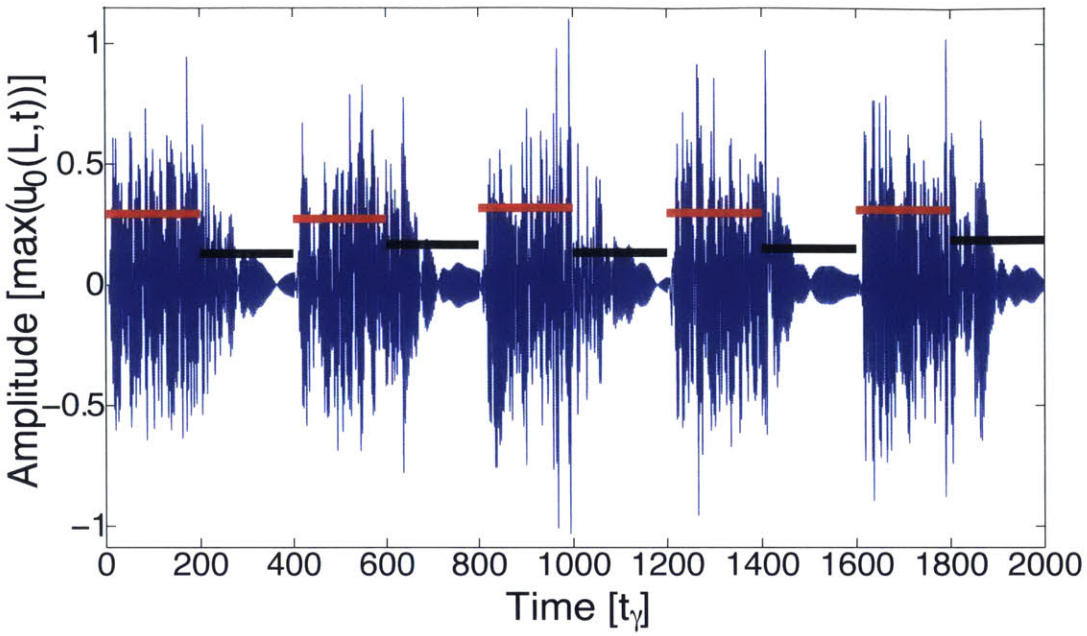

Figure 4-11: Transmitted phonon current as a function of normalized amplitude vs. time for a lattice of photoswitches driven by a pulsed laser in a switch/transistor regime. The blue curve denotes the calculated response, the black lines are the rms averaged amplitude over the dark intervals, and the red lines are the rms averaged amplitude over illuminated intervals. The separation between the black and red curves is the switch's figure of merit. Reprinted figure with permission from S. R. Sklan and J. C. Grossman, *Phys. Rev. B*, **92**, 165107 (2015). Copyright 2015 by the American Physical Society [306].

denote the rms averaged amplitude for each period of darkness or illumination (these also include the intermediate intervals, therein underestimating the difference between the dark and illuminated states). For frequencies below ω_g there is transmission regardless of the presence of light so the ratio of these averages is nearly 1 (not shown). For frequencies just above ω_g, on the other hand, there exists a considerable difference between the states and so a large separation is observed (Fig. 4-11). As frequency increases above ω_g, transmission in the illuminated state drops and the ratio again approaches 1 (not shown). In comparing these results with Fig. 4-9 it is clear that there exists a cross-over from confinement to transmission with increasing photon intensity. Ergo, for confinement to be effective there should be narrow domains of propagating configuration, something that is best achieved using weak driving.

4.5 Photoswitchable Transport Conclusions

The case of high frequency tuning is in many respects the inverse of low frequency tuning. Here, the tuning signal can adapt to changes in the phonon distribution much faster than the distribution can change. This can be used to create artificial effective couplings between phonon modes (as in [303, 304, 305]). It can also used to change the dynamical properties of phonon transport on very short timescales, as we demonstrated with the inverse acousto-optic effect and the opto-phononic switch. Moreover, the operation of dynamical phonon confinement/steering illustrated in Fig. 4-9 is indicative of these fast changes. The ability to quickly open and close domains of allowed phonon propagation is integral to the operation of such a device.

On the other hand, from the perspective of the phonon field high frequency tuning is distinct from low frequency tuning. Because the phonons can constantly adapt to the changing conditions in low frequency tuning, the operation is approximately adiabatic and perturbations to the phonon field are negligible. Whereas for high frequency tuning the effects are strongly perturbative and can introduce phonon scattering terms. This scattering will depend upon the spatial distribution of the tuning, as illustrated by contrasting the long wavelength/low frequency phonon response of Fig. 4-7 with the comparable wavelength/mid frequency phonon response of Fig. 4-8. In the latter, the presence of multiple reflections is clearly indicative of scattering induced by the stochastic parametric driving. While the situation illustrated in Fig. 4-8 couples modes of wave vector k to those of $-k$, this is an artifact of assuming a one-dimensional, harmonic system. Relaxing these constraints would likely increase the scattering and induce a perturbative coupling of these phonons to other phonon modes. All of these effects are, notably, not captured by the band structure picture of phonon transport (which assumes perfectly decoupled modes of infinite lifetime). Just as we saw that the band structure is insufficient to determine the eigenmode's spatial symmetries, this is another case where controlling transport requires going beyond the band structure picture. This is not to say that the band structure has no bearing on the scattering of anharmonic phonons, as it is often a good guide to what modes can be excited. In particular, when looking at the spectral intensity distribution of phonons in nonlinear media, the band structure persists and produces clear signatures [192, 320]. Studying the

tunability of these distributions for various initial phonon populations, in addition to the band structure, is crucial for understanding the transport of phonons in the anharmonic, high-frequency tuning regime.

Chapter 5

Outlook

Tunable materials, we have seen, are a powerful tool for controlling transport under changing conditions. By applying control signals at different frequencies, it is possible to modulate the phonon band structure, induce resonant mode mixing between multiple degrees of freedom, and scatter phonons into new states. These shifts can create or transform band gaps (blocking transmission), shift the speed of sound, and introduce phase differences between signals. In many situations, the phonon density of states is approximately continuous with frequency or spans many discrete frequencies. In this case, a single harmonic tuning signal will influence these various modes differently depending upon their relative frequencies. As such, it is entirely possible to have all of these different responses existing within a single material.

The effect of tuning goes beyond just shifting the band structure, however. As we have seen, there are many situations where a simple band structure picture is insufficient to understand the effect of tuning. Transport dynamics, especially in the diffusive limit, do not always intuitively map to band structure. And even then, the effect of non-stationary materials on transport can non-trivially affect their dynamics. Failure to account for non-stationary driving or changing boundary conditions can impact the operation of many devices. Furthermore, band structures do not contain information about the spatial properties of the eigenmodes. The ability to tune eigenmodes, especially their symmetry properties, is generally important (particularly for spatially inhomogeneous systems). Annotating band diagrams

to denote their eigenmode's symmetry properties would go some ways to elucidating the effects of tuning upon this aspect of transport [1]. Lastly, the assumption of harmonicity needs to be understood as merely an approximation in many cases. Incorporating finite lifetimes, and the resultant complex wave vectors or population redistribution, would illuminate this under-examined aspect of transport. The context of tunable materials is a particularly fruitful one for this extension, as the ability to tune mode lifetimes or control decay dynamics would open up new avenues for controlling transport.

While the analysis presented here divided the effects of tuning upon dynamics by time scale (i.e. by $\omega\tau$, as in Tabl.e 1.1), this is not the only way to think about tuning. The ability to focus upon individual modes and draw analogies with simple harmonic oscillators makes it an important tool for clarifying dynamical regimes, but the spatial extent of tuning is also important. It is somewhat complicated by the existence of multiple length scales (sample size, mean free path, coherence length, and wavelength), not all of which are significant when just considering time scales. The topic has been considered in the context of static tuning [13], but in many cases one is interested in using spatio-temporal modulation of transport through tuning signals. Spatio-temporal modulation is already an important tool in generating phonon wave packets with desired amplitudes, but an extension of this technique to tuning would potentially open up new classes of phononic devices.

It is also worth bearing in mind that the control of energy transport has different constraints than control of information transport. Energy tends to be transported over broad ranges of frequencies, entailing the control of multiple branches. It also tends to be less sensitive to things like spatial symmetries or coherence, and so does not require as fine a degree of control. Lifetimes are still important, particularly to the extent that modes in the controlled frequency range are decaying into modes outside of one's control. Information, on the other hand, is generally carried by much narrower frequency packets. Phase and coherence matter more here, so it is often necessary to account for non-band structure effects like spatial symmetries and lifetimes. While there are some aspects of tuning where the requirements for energy and information overlap (i.e. decay routes) and the transport of either energy or information entails the transport of the other, in many applications they have quite different requirements.

[1] Computationally, Wannier wave functions are an important tool for this problem.

This contrast between the requirements of energy and information reveals that, when seeking to create new means of controlling phonon transport, it is important to recognize not only what the technique can do but also what context it is intended for. For example, an obvious extension of phonon computing would be to create a quantum phonon computer. However, this is challenging due to the need to eliminate every form of amplitude or phase decay to preserve qubit states. On the other hand, the elimination of every decay pathway would make the qubit impossible to read or write (and therefore useless for a computing architecture), and so some form of interaction must remain. This is particularly true for hybrid quantum computing designs (see Ch. 4.2.2 and Refs. [293, 294, 295, 296, 297, 298, 299, 300, 301, 302]), where phonons are used as an interface between different computing architectures [2]. Contrast this with trying to improve thermal cloaking (primarily an issue of energy transport), discussed in Ch. 2.3. There, decay is utterly unimportant except as a constraint upon thermodynamic equilibrium. Instead, the greatest challenge is materials design, specifically the engineering of specific heat. This is equivalent to a concern with the number of degrees of freedom that are thermally accessible, rather than how those degrees of freedom relate to each other (i.e. decay). In further contrast, the phonon transport considered in photoswitchable materials (see Ch. 4.4) was purely ballistic and no decay needed to be considered. If we were to extrapolate this work by incorporating decay, the phenomena that we observed would still exist but the entire picture would become more complicated. Thermal phonon populations induced by photoexcitation would not change the band structure and so the inverse acousto-optic effect should be robust. Scattering and the stochastic transmission/reflection of phonons at intermediate frequencies (an energy transport problem) as well as high frequency phonon confinement (an information transport problem) would, however, be in competition with thermal equilibration in this case. In both scattering and confinement the control of decay becomes crucial – for the entire middle frequency phonon spectrum in the case of scattering and for specific high frequency modes in the case of confinement.

This interplay between the transport of information and sound and the competition between decay and coupling is one which tuning is particularly adept at addressing. While this aspect of tuning has gone under-examined, it is especially promising and not without precedent.

[2] Phononic computing using mediated interactions, as Refs. [303, 304, 305] consider, do not circumvent this challenge as the existence of an interaction pathway implies the existence of a decay pathway.

It was once believed [3] that in the far North lay the island of Nova Zembla, which grew so cold in the winter that words would freeze in mid-air and could not be heard until they thawed in the summer. This is thermally tunable transport applied to acoustic lifetimes and velocity. By tuning materials, we can get beyond the need for a perfect device that has ideal characteristics in all circumstances and turn instead to making devices that can adapt to differing requirements. The flexibility of tunable materials is perhaps the most promising tool for guiding phonons with specificity and turning their tendency to couple almost every other information or energy carrier from a detriment to an advantage.

[3]Plutarch, for example, confidently proclaimed this fact.

Bibliography

[1] N. Li, J. Ren, L. Wang, G. Zhang, P. Hänggi, and B. Li, *Rev. Mod. Phys.* **84**, 1045 (2012).

[2] S. R. Sklan, *AIP Advances* **5**, 053302 (2015).

[3] K. Vahala, M. Herrmann, S. Knünz, V. Batteiger, G. Saathoff, T. W. Hänsch, and Th. Udem, *Nat. Phys.* **5**, 682 (2009).

[4] Ivan S. Grudinin, Hansuek Lee, O. Painter, and Kerry J. Vahala, *Phys. Rev. Lett.* **104**, 083901 (2010).

[5] S. M. Rytov, *Akust. Zh. Akust. Zh. (USSR)* **2**, 71 (1956).

[6] S. M. Rytov, *Sov. Phys. Acoust.* **2**, 67 (1956).

[7] P. A. Deymier (Ed.), *Acoustic Metamaterials and Phononic Crystals* (Springer, New York, NY, 2013).

[8] C. Colvard, T. A. Gant, M. V. Klein, R. Merlin, R. Fisher, H. Morkoc, and A. C. Gossard, *Phys. Rev. B* **31**, 2080 (1985).

[9] A. A. Balandin and K. L. Wang, *Phys. Rev. B* **58**, 1544 (1998).

[10] J. Zou and A. Balandin, *J. Appl. Phys.* **89**, 2932 (2001).

[11] E. P. Pokatilov, D. L. Nika, and A. A. Balandin, *Phys. Rev. B* **72**, 113311 (2005).

[12] E. P. Pokatilov, D. L. Nika, and A. A. Balandin, *Superlatt. Microstruct.* **33**, 155 (2003).

[13] A. A. Blandin, E. P. Pokatilov, and D. L. Nika, *J. Nanoelectron. Optoe.* **2**, 140 (2007).

[14] P. M. Norris, N. Q. Le, and C. H. Baker, *J. Heat Transf.* **135**, 061604 (2013).

[15] C. Goffaux and J. P. Vigneron, *Phys. Rev. B* **64**, 075118 (2001).

[16] W. M. Kuang, Z. L. Hou, and Y. Y. Liu, *Phys. Lett. A* **332**, 481 (2004).

[17] S.-C. S. Lin and T. J. Huang, *Phys. Rev. B* **83**, 174303 (2011).

[18] Z. L. Hou, X. J. Fu, and Y. Y. Liu, *Phys. Lett. A* **317**, 127 (2003).

[19] Y.W. Yao, Z. L. Hou, and Y. Y. Liu, *Phys. Lett. A* **362**, 494 (2007).

[20] N. A. Roberts and D. G. Walker, *Int. J. Therm. Sci.* **50**, 648 (2011).

[21] W.-P. Hsieh, A. S. Lyons, E. Pop, P. Keblinski, and D. G. Cahill, *Phys. Rev B* **84**, 184107 (2011).

[22] K. Bertoldi and M.C. Boyce, *Phys. Rev. B* **77**, 052105 (2008).

[23] K. Bertoldi and M.C. Boyce, *Phys. Rev. B* **78**, 184107 (2008).

[24] J.-H. Jang, C.Y. Koh, K. Bertoldi, M.C. Boyce, and E.L. Thomas, *Nano Lett.* **9**, 5 (2009).

[25] F. Göncü, S. Luding, and K. Bertoldi, *J. Acoust. Soc. Am.* **131**, 6 (2012).

[26] A. Cicek, O. A. Kaya, and B. Ulug, *Appl. Acoust.* **73**, 1 (2012).

[27] P. Wang, F. Casadei, S. Shan, J. C. Weaver, and K. Bertoldi, *Phys. Rev. Lett.* **113**, 014301 (2014).

[28] S. Shan, S. H. Kang, P. Wang, C. Qu, S. Shian, E. R. Chen, and K. Bertoldi, *Adv. Funct. Mater.* **24**, 31 (2014).

[29] A. Bayat and F. Gordaninejad, *Smart Mater. Struct.* **24**, 075009 (2015).

[30] L. Wang and K. Bertoldi, *Int. J. Solids Struct.* **49**, 2881 (2012).

[31] S. Babaee, P. Wang, and K. Bertoldi, *J. Appl. Phys.* **117**, 244903 (2015).

[32] P. Wang, J. Shim, and K. Bertoldi, *Phys. Rev. B* **88**, 014304 (2013).

[33] J. Shim, P. Wang, and K. Bertoldi, *Int. J. Solids Struct.* **58**, 52 (2015).

[34] E. B. Herbold, J. Kim, V. F. Nesterenko, S. Y. Wang, and C. Daraio, *Acta Mech.* **205**, 1 (2009).

[35] N. Boechler, J. Yang, G. Theocharis, P. G. Kevrekidis, and C. Daraio, *J. Appl. Phys.* **109**, 074906 (2011).

[36] F. Li, D. Ngo, J. Yang, and C. Daraio, *Appl. Phys. Lett.* **101**, 171903 (2012).

[37] A. Evgrafov, C. J. Rupp, M. L. Dunn, and K. Maute, *Comput. Methods Appl. Mech. Eng.* **198**, 292 (2008).

[38] M. Gei, A. B. Movchan, D. Bigoni. *J. Appl. Phys.* **105**, 063507 (2009).

[39] C. Daraio, V. F. Nesterenko, E. B. Herbold, and S. Jin, *Phys. Rev. E* **73**, 026610 (2006).

[40] A. Spadonia and C. Daraio, *P. Natl. Acad. Sci. USA* **107**, 16 (2010).

[41] C. M. Donahue, P. W. J. Anzel, L. Bonanomi, T. A. Keller, and C. Daraio, *Appl. Phys. Lett.* **104**, 014103 (2014).

[42] N. Boechler, G. Theocharis, and C. Daraio, *Nat. Mater.* **10**, 665 (2011).

[43] Z.-G. Huang and T.-T. Wu, *IEEE Trans. Ultrason. Ferroelectr. Freq. Control* **52**, 3 (2005).

[44] L.-Y. Wu, W.-P. Yang, and L.-W. Chen, *Phys. Lett. A* **372**, 2701 (2008).

[45] K. L. Jim, C. W. Leung, S. T. Lau, S. H. Choy, and H. L. W. Chan, *Appl. Phys. Lett.* **94**, 193501 (2009).

[46] C. Xu, F. Cai, S. Xie, F. Li, R. Sun, X. Fu, R. Xiong, Y. Zhang, H. Zheng, and J. Li, *Phys. Rev. Applied* **4**, 034009 (2015).

[47] Y. Cheng, X. J. Liu, and D. J. Wu, *J. Acoust. Soc. Am.* **129**, 3 (2011).

[48] Y. Yao, F. Wu, X. Zhang, and Z. Hou, *J. Appl. Phys.* **110**, 123503 (2011).

[49] Z. Bian, W. Peng, and J. Song, *J. Appl. Mech* **81**, 041008 (2013).

[50] A. Sato, Y. Pennec, N. Shingne, T. Thurn-Albrecht, W. Knoll, M. Steinhart, B. Djafari-Rouhani, and G. Fytas, *ACS Nano* **4**, 6 (2010).

[51] R.T. Zheng, J. Gao, J. Wang, and G. Chen, *Nat. Commun.* **2**, 289 (2011).

[52] Z. Y. Wang, H. Wang, X. B. Li, D. Z. Wang, Q. Y. Zhang, G. Chen, and Z. F. Ren, *Appl. Therm. Eng.* **89**, 204 (2015).

[53] V. S. Vikhnin, S. Lysenko, A. Rua, F. Fernandez, and H. Liu, *Phys. Lett. A* **343**, 6 (2005).

[54] E. Arcangeletti, L. Baldassarre, D. Di Castro, S. Lupi, L. Malavasi, C. Marini, A. Perucchi, and P. Postorino, *Phys. Rev. Lett.* **98**, 196406 (2007).

[55] H. T. Kim, B. G. Chae, D. H. Youn, S. L. Maeng, G. Kim, K. Y. Kang, and Y.-S. Lim, *New J. Phys.* **6**, 52 (2004).

[56] A. Cavalleri, Cs. Tóth, H. C. W. Siders, J. A. Squier, F. Raksi, P. Forget, and J. C. Kieffer, *Phys. Rev. Lett.* **87**, 237401 (2001).

[57] S. Lysenko, V. Vikhnin, F. Fernández, A. Rua, and H. Liu, *Phys. Rev. B* **75**, 075109 (2007).

[58] S. Lysenko, A. Rúa, V. Vikhnin, F. Fernández, and H. Liu, *Phys. Rev. B* **76**, 035104 (2007).

[59] N. Sepúlveda, A. Rúa, R. Cabrera, and F. Fernández, *Appl. Phys. Lett.* **92**, 191913 (2008).

[60] Z. Chen, *J. Appl. Phys.* **117**, 124902 (2015).

[61] E. Walker, D. Reyes, M. M. Rojas, A. Krokhin, Z. Wang, and A. Neogi, *Appl. Phys. Lett.* **105**, 143503 (2014).

[62] M. Ruzzene and A. Baz, *J. Vib. Acoust.* **122**, 151 (2000).

[63] M. Ruzzene and A. Baz, *Smart Mater. Struct.* **9**, 805 (2000).

[64] Z. Hou, F. Wu, and Y. Liu, *Solid State Commun.* **130**, 11 (2004).

[65] Y.-Z. Wang, F.-M. Li, Y.-S. Wang, K. Kishimoto, and W.-H. Huang, *Acta Mech. Sin.* **25**, 65 (2009).

[66] X.-Y. Zou, Q. Chen, B. Liang, and J.-C. Cheng, *Smart Mater. Struct.* **17**, 015008 (2008).

[67] C. J. Rupp, M. L. Dunn, K. Maute, *Appl. Phys. Lett.* **96**, 111902 (2010).

[68] J. H. Oh, I. K. Lee, P. S. Ma, and Y. Y. Kim, *Appl. Phys. Lett.* **99**, 083505 (2011).

[69] P. Celli and S. Gonella, *J. Appl. Phys.* **115**, 103502 (2014).

[70] P. Celli and S. Gonella, *Appl. Phys. Lett.* **106**, 091905 (2015).

[71] A. A. Kusenko, A. L. Shuvalov, O. Poncelet, and A. N. Darinskii, *J. Acoust. Soc. Am.* **137**, 2 (2015).

[72] J.-C. Hsu, *Jpn. J. Appl. Phys., Part 1* **51**, 07GA04 (2012).

[73] S.-B. Chen, J.-H. Wen, D. L. Yu, G. Wand, and X.-S. Wen, *Chin. Phys. B* **20**, 014301 (2011).

[74] S. Degraeve, C. Granger, B. Dubus, J. O. Vasseur, M. Pham Thi, and A.-C. Hladky-Hennion, *J. Appl. Phys.* **115**, 194508 (2014).

[75] W.-P. Yang, and L.-W. Chen, *Smart Mater. Struct.* **17**, 015011 (2008).

[76] W.-P. Yang, L.-Y. Wu, and L.-W. Chen, *J. Phys. D Appl. Phys.* **41**, 135408 (2008).

[77] L.-Y. Wu, M.-L. Wu, and L.-W. Chen, *Smart Mater. Struct.* **18**, 015011 (2009).

[78] J. F. Ihlefeld, B. M. Foley, D. A. Scrymgeour, J. R. Michael, B. B. McKenzie, D. L. Medlin, M. Wallace, S. Trolier-McKinstry, and P. E. Hopkins, *Nano Lett.* **15**, 1795 (2015).

[79] H. Tang, C. Luo, and X. Zhao, *J. Phys. D Appl. Phys.* **37**, 2331 (2004).

[80] H. Tang, C. Luo, and X. Zhao, *J. Appl. Phys.* **98**, 016103 (2005).

[81] J.-Y. Yeh, *Physica B* **400**, 137 (2007).

[82] J.-F. Robillard, O. Bou Matar, J. O. Vasseur, P. A. Deymier, M. Stippinger, A.-C. Hladky-Hennion, Y. Pennec, and B. Djafari-Rouhani, *Appl. Phys. Lett.* **95**, 124104 (2009).

[83] O. Bou Matar, J. F. Robillard, J. Vasseur, A.-C. Hladky-Hennion, P. A. Deymier, P. Pernod, V. Preobrazhensky, *J. Appl. Phys.* **111**, 054901 (2012).

[84] J. O. Vasseur, O. Bou Matar, J. F. Robillard, A.-C. Hladky-Hennion, and P. A. Deymier, *AIP Advances* **1**, 041904 (2011).

[85] A. Yang, P. Li, Y. Wen, C. Lu, X. Peng, J. Zhang, W. He, D. Wang, and C. Yang, *Appl. Phys. Lett.* **105**, 011904 (2014).

[86] A. Yang, P. Li, Y. Wen, C. Yang, D. Wang, F. Zhang, and J. Zhang, *Appl. Phys. Express* **8**, 9 (2015).

[87] M. Schaeffer and M. Ruzzene, *Int. J. Solids Struct.* **56**, 78 (2015).

[88] J. Baumgartl, M. Zvyagolskaya, and C. Bechinger, *Phys. Rev. Lett.* **99**, 205503 (2007).

[89] B. Wu, R. Wei, C. He, and H. Zhao, *IEEE Int. Ultrason. Symp. Proc.*, 1484 (2008).

[90] S. M. Hasheminejad and M. Shabanimotlagh, *Smart Mater. Struct.* **19**, 3 (2009).

[91] Z. Xu, F. Wu, Z. Guo, *Solid State Commun* **154**, 43 (2013).

[92] Y.-Z. Wang, F.-M. Li, W.-H. Huang, X. Jiang, Y.-S. Wang, and K. Kishimoto, *Int. J. Solids Struct.* **45**, 14 (2008).

[93] Y. Huang, C. L. Zhang, and W. Q. Che, *J. Appl. Mech* **81**, 9 (2014).

[94] P. N. Kambali, G. Swain, A. K. Pandey, E. Buks, and O. Gottlieb, *Appl. Phys. Lett.* **107**, 063104 (2015).

[95] J.-H. Jang, C. Y. Koh, K. Bertoldi, M. C. Boyce, and E. L. Thomas, *Nano Lett.* **9**, 5 (2009).

[96] S. Zhang, Y. Shi, and Y. Gao, *J. Appl. Phys.* **118**, 034101 (2015).

[97] R. Ding, X. Su, J. Zhang, and Y. Gao, *J. Appl. Phys.* **115**, 074104 (2014).

[98] A. Bayat and F. Gordaninejad, *Smart Mater. Struct.* **24**, 065027 (2015).

[99] A. Bayat and F. Gordaninejad, *J. Vib. Acoust* **137**, 1 (2015).

[100] J. B. Pendry, D. Schurig, and D. R. Smith, *Science* **312**, 5781 (2006).

[101] U. Leonhardt, *Science* **312**, 1777 (2006).

[102] U. Leonhardt and T. G. Philbin, *New J. Phys.* **8**, 247 (2006).

[103] H. Y. Chen and C. T. Chan, *Appl. Phys. Lett.* **91**, 183518 (2007).

[104] H. Y. Chen and C. T. Chan, *J. Phys. D Appl. Phys.* **43**, 113001 (2010).

[105] S. Sklan, *Phys. Rev. E* **81**, 016606 (2010).

[106] A. Greenleaf, Y. Kurylev, M. Lassas, and G. Uhlmann, *Commun. Math. Phys.* **275**, 749 (2007).

[107] J. Li and J. B. Pendry, *Phys. Rev. Lett.* **101**, 203901 (2008).

[108] J. C. Halimeh, T. Ergin, J. Mueller, N. Stenger, and M. Wegener, *Opt. Express* **17**, 19328 (2009).

[109] B. Zhang, T. Chan, and B.-I. Wu, *Phys. Rev. Lett.* **104**, 233903 (2010).

[110] Y. Lai, H. Y. Chen, Z. Q. Zhang, and C. T. Chan, *Phys. Rev. Lett.* **102**, 093901 (2009).

[111] J. B. Pendry and S. A. Ramakrishna, *J. Phys. Condens. Matter* **15**, 6345 (2003).

[112] B. Liu and J. P. Huang *Eur. Phys. J. Appl. Phys.* **48**, 1 (2009).

[113] U. Leonhardt and T. Tyc, *Science* **323**, 110 (2009).

[114] F. Zolla, G. Guenneau, A. Nicolet, and J. B. Pendry, *Opt. Lett.* **32** 1069 (2007).

[115] H. Chen, B.-I. Wu, B. Zhang, and J. A. Kong, *Phys. Rev. Lett.* **99**, 063903 (2007).

[116] A. Greenleaf, M. Lassas, and G. Uhlmann, *Physiolog. Meas.* **24**, 413 (2003).

[117] A. Greenleaf, M. Lassas, and G. Uhlmann, *Math. Res. Lett.* **10**, 685 (2003).

[118] Z. Ruan, M. Yan, C. W. Neff, and M. Qiu, *Phys. Rev. Lett.* **99**, 113903 (2007).

[119] G. Isić, R. Gajić, B. Novaković, Z. V. Popović, and K. Hingerl, *Opt. Express* **16**, 3 1413 (2008).

[120] B. Zhang, H. Chen, B.-I. Wu, Y. Luo, L. Ran, and J. A. Kong, *Phys. Rev. B* **76**, 121101(R) (2007).

[121] M. Rahm, D. Schurig, D. A. Roberts, S. A. Cummer, D. R. Smith, and J. B. Pendry, *Photonics Nanostruct. Fundam. Appl.* **6**, 87 (2008).

[122] W. X. Jiang, C. Y. Luo, H. F. Ma, Z. L. Mei, and T. J. Cui, *Sci. Rep.* **2**, 956 (2012).

[123] H. Chen and C. T. Chan, *Appl. Phys. Lett.* **90**, 241105 (2007).

[124] H. Chen and C. T. Chan, *Phys. Rev. B* **78**, 054204 (2008).

[125] H. Chen, B. Hou, S. Chen, X. Ao, W. Wen, and C. T. Chan, *Phys. Rev. Lett.* **102**, 183903 (2009).

[126] Y. Lai, J. Ng, H. Chen, D. Han, J. Xiao, Z. Zhang, and C. T. Chan, *Phys. Rev. Lett.* **102**, 253902 (2009).

[127] C. Li, X. Meng, X. Liu, F. Li, G. Fang, H. Chen, and C. T. Chan, *Phys. Rev. Lett.* **105**, 233906 (2010).

[128] W. X. Jiang and T. J. Cui, *Phys. Rev. E* **83**, 026601 (2011).

[129] W. X. Jiang, T. J. Cui, X. M. Yang, H. F. Ma, and Q. Cheng, *Appl. Phys. Lett.* **98**, 204101 (2011).

[130] W. X. Jiang, C.-W. Qiu, T. C. Han, S. Zhang, and T. J. Cui, *Adv. Funct. Mater.* **23**, 32 (2013).

[131] M. Liu, Z. L. Mei, X. Ma, and T. J. Cui, *Appl. Phys. Lett.* **101** 101, 051905 (2012).

[132] W. Kan, B. Liang, X. Zhu, R. Li, X. Zou, H. Wu, J. Yang, and J. Cheng, *Sci. Rep.* **3**, 1427 (2013).

[133] M. W. McCall, A. Favaro, P. Kinsler, and A. Boardman, *J. Opt.* **13**, 024003 (2011).

[134] G. W. Milton, M. Briane, and J. R. Willis, *New J. Phys.* **8**, 248 (2006).

[135] S. A. Cummer and D. Schurig, *New J. Phys.* **9**, 45 (2007).

[136] S. A. Cummer, B.-I. Popa, D. Schurig, D. R. Smith, J. Pendry, M. Rahm, and A. Starr, *Phys. Rev. Lett.* **100**, 024301 (2008).

[137] M. Farhat, S. Enoch, S. Guenneau, and A. B. Movchan, *Phys. Rev. Lett.* **101**, 134501 (2008).

[138] H. Chen, J. Yanh, J. Zi, and C. T. Chan, *EPL* **85**, 24004 (2009).

[139] S. Zhang, D. A. Genov, C. Sun, and X. Zhang, *Phys. Rev. Lett.* **100**, 123002 (2008).

[140] A. Greenleaf, Y. Kurylev, M. Lassas, and G. Uhlmann, *New J. Phys.* **10** 115024 (2008).

[141] R. Fleury and A. Alù, *Phys. Rev. B* **87**, 045423 (2013).

[142] M. Kadic, T. Bückmann, R. Schittny, and M. Wegener, *Rep. Prog. Phys.* **76**, 126501 (2013).

[143] S. Guenneau and T. M. Puvirajesinghe, *J. R. Soc. Interface* **10**, 20130106 (2013).

[144] L. Zeng and R. Song, *Sci. Rep.* **3**, 3359 (2013).

[145] R. Schittny, M. Kadic, T. Bückmann, and M. Wegener, *Science* **325**, 6195, (2014).

[146] C. Z. Fan, Y. Gao, and J. Huang, *Appl. Phys. Lett.* **92**, 251907 (2008).

[147] S. Guenneau, C. Amra, and D. Veynante, *Opt. Express* **20**, 8207 (2012).

[148] R. Schittny, M. Kadic, S. Guenneau, and M. Wegener, *Phys. Rev. Lett.* **110**, 195901 (2013).

[149] S. Narayana, S. Savo, and Y. Sato, *Appl. Phys. Lett.* **102**, 201904 (2013).

[150] Y. Ma, L. Lan, W. Jiang, F. Sun, and S. He, *NPG Asia Mater.* **5**, e73 (2013).

[151] S. Narayana and Y. Sato, *Phys. Rev. Lett.* **108**, 214303 (2012).

[152] H. Xu, X. Shi, F. Gao, H. Sun, and B. Zhang*Phys. Rev. Lett.* **112**, 054301 (2014).

[153] J. Y. Li, Y. Gao, and J. P. Huang, *J. Appl. Phys.* **108**, 074504 (2010).

[154] S. Guenneau and C. Amra, *Opt. Express* **21** 6578 (2013).

[155] X. He and L. Wu, *Appl. Phys. Lett.* **105**, 221904 (2014).

[156] S. Sklan, X. Bai, B. Li, and X. Zhang, *New J. Phys.* (under review).

[157] COMSOL AB, *COMSOL Multiphysics User's Guide, Version 4.3b* (Burlington, 2013).

[158] M. Abramowitz, and I. A. Stegun, *Handbook of Mathematical Functions* (National Bureau of Standards, Washington, D.C., 1972).

[159] T. Han, X. Bai, D. Gao, J. T.L. Thong, B. Li, and C.-W. Qiu, *Phys. Rev. Lett.* **112**, 054302 (2014).

[160] K.B. Tolpygo, *Zh. Eks. Teor. Fiz.* **20**, 6 (1950), in Russian. English translation: *Ukr. J. Phys.* **53**, special issue (2008).

[161] U. Fano, *Phys. Rev.* **103**, 5 (1956).

[162] A. M. Weiner, D. E. Leaird, G. P. Wiederrecht, and K. A. Nelson, *Science* **247**, 4948 (1990).

[163] A. Bartels, T. Dekorsy, H. Kurz, and K. Köhler, *Appl. Phys. Lett.* **72**, 2844 (1998).

[164] J.-C. Beugnot and V. Laude, *Phys. Rev. B* **86**, 224304 (2012).

[165] V. Laude and J.-C. Beugnot, *AIP Advances* **3**, 042109 (2013).

[166] F. Enderli and T. Feurer, *Appl. Phys. Lett.* **103**, 061903 (2013).

[167] T. Feurer, J. C. Vaughan, and K. A. Nelson, *Science* **299**, 5605 (2003).

[168] K. Katayama, H. Inoue, H. Sugiya, Q. Shen, T. Toyoda, and K. A. Nelson, *Appl. Phys. Lett.* **92**, 031906 (2008).

[169] R. H. Poolman, E. A. Muljarov, and A. L. Ivanov, *Phys. Rev. B* **81**, 245208 (2010).

[170] V. W. Brar, M. S. Jang, M. Sherrott, J. J. Lopez, and H. A. Atwater, *Nano Lett.* **13**, 6 (2013).

[171] A. Kumar, T. Low, K. H. Fung, Ph. Avouris, and N. X. Fang, *Nano Lett.* **15**, 5 (2015).

[172] S. Dai, Q. Ma, M. K. Liu, T. Andersen, Z. Fei, M. D. Goldflam, M. Wagner, K. Watanabe, T. Taniguchi, M. Thiemens, F. Keilmann, G. C. A. M. Janssen, S-E. Zhu, P. Jarillo-Herrero, M. M. Fogler, D. N. Basov, *Nat. Nanotechnol.* **10**, 682 (2015).

[173] Y. Sun, Z. Zheng, J. Cheng, and J. Liu, arXiV:1412.8519 (2014).

[174] J.-S. Wu, D. N. Basov, and M. M. Fogler, arXiv:1509.02642 (2015).

[175] G. Wang, S.-B. Chen, and J.-H. Wen, *Smart Mater. Struct.* **20**, 015026 (2011).

[176] S.-B. Chen, J.-H. Wen, G. Wang, D. L. Yu, and X.-S. Wen, *J. Intell. Mater. Syst. Struct.* **23**, 1613 (2012).

[177] F. Casadei, T. Delpero, A. Bergamini, P. Ermanni, and M. Ruzzene, *J. Appl. Phys.* **112**, 064902 (2012).

[178] A. Bergamini, T. Delpero, L. De Simoni, L. Di Lillo, M. Ruzzene, and P. Ermanni, *Adv. Mater.* **26**, 1343 (2013).

[179] Z. Hou and B. M. Assouar, *Appl. Phys. Lett.* **106**, 251901 (2015).

[180] X. Zhou and C. Chen, *Physica B* **431**, 23 (2013).

[181] B. Liu and M. T. Shaw, *J. Rheol.* **45**, 641 (2001).

[182] Y. Y. Chen and G. L. Huang, *Acta Mech. Sin.* **31**, 3 (2015).

[183] B.-J. Kwon, J.-Y. Jung, D. Lee, K.-C. Park, and I.-K. Oh, *Smart Mater. Struct.* **24**, 105018 (2015).

[184] Y. Chen, J. Hui, and G. Huang, *J. Intell. Mater. Syst. Struct.*, (in press) doi:10.1177/1045389X15590273 (2015).

[185] S. Krylov, S. Lulinsky, B. R. Ilic, and I. Schneider, *Appl. Phys. Lett.* **105**, 071909 (2014).

[186] D. Hatanaka, I. Mahboob, K. Onomitsu, and H. Yamaguchi, *Appl. Phys. Lett.* **102**, 213102 (2013).

[187] D. Hatanaka, I. Mahboob, K. Onomitsu, and H. Yamaguchi, *Nat. Nanotechnol.* **9**, 520 (2014).

[188] C. Vanhille and C. Campos-Pozuelo, *Ultrason. Sonochem.* **21**, 50 (2014).

[189] B. Liang, W.-W. Kan, X.-Y. Zou, L.-L. Yin, and J.-C. Cheng, *Appl. Phys. Lett.* **105**, 083510 (2014).

[190] F. Li, P. Anzel, J. Yang, P. G. Kevrekidis, and C. Daraio, *Nat. Commun.* **5**, 5311 (2014).

[191] F. Li, C. Chong, J. Yang, P. G. Kevrekidis, and C. Daraio, *Phys. Rev. E* **90**, 053201 (2014).

[192] R. Ganesh and S. Gonella, *Phys. Rev. Lett.* **114**, 054302 (2015).

[193] T. Ando, *Physica E* **43**, 645 (2011).

[194] P. Leszczynski, Z. Han, A. A. L. Nicolet, B. A. Piot, P. Kossacki, M. Orlita, V. Bouchiat, D. M. Basko, M. Potemski, and C. Faugeras, *Nano Lett.* **14**, 3 (2014).

[195] C. Kittel, *Phys. Rev.* **110**, 836 (1958).

[196] K. B. Vlasov, *Phys. Met. Metallogr. (USSR)* **7**, 3 (1959).

[197] H. Matthews and R. C LeCraw, *Phys. Rev. Lett.* **8**, 397 (1962).

[198] M. Boiteux, P. Doussineau, B. Ferry, J. Joffrin, and A Levelut, *Phys. Rev. B* **4**, 3077 (1971)

[199] E. A. Turov, *Phys. Met. Metallogr. (USSR)* **23**, 1 (1991).

[200] B. I. Kochelaev, *Sov. Phys. Sol. State* **4**, 1145 (1962).

[201] J. W. Tucker, *Phys. Lett. A* **43**, 5 (1973).

[202] I. D. Tokman, V. I. Pozdnjakova, and A. I. Beludanova, *Phys. Rev. B* **83**, 014405 (2011).

[203] A. Sytcheva, U. Löw, S. Yasin, J. Wosnitza, S. Zherlitsyn, P. Thalmeier, T. Goto, P. Wyder, and B. Lüthi, *Phys. Rev. B* **81**, 214415 (2010).

[204] P. Thalmeier, *Phys. Rev. B* **80**, 214421 (2010).

[205] T. Ando, *J. Phys. Soc. Jpn.* **76**, 2 (2007).

[206] J. Mertsching, *Phys. Status Solidi* **37**, 465 (1970).

[207] R. W. Morse and J. D. Gavenda, *Phys. Rev. Lett.* **2**, 250 (1959).

[208] V. T. Petrashov, *Rep. Prog. Phys.* **47**, 47 (1984)

[209] C. C. Grimes and S. J. Buchsbaum, *Phys. Rev. Lett.* **12**, 357 (1964).

[210] E. I. Kaner and V. G. Skobov, *Phys. Lett.* **25A**, 105 (1967).

[211] L. T. Tsymbal and T. F. Butenko, *Solid State Commun.* **13**, 357 (1964).

[212] V. V. Gudkov, *Ultrasonics* **44**, e1405 (2006).

[213] J. D. Gavenda and V. V. Gudkov, *Magnetoacoustic Polarization Phenomena in Solids* (Springer, New York, NY, 2000).

[214] M. V. Wilkes, *J. ACM* **15**, 1 (1968).

[215] J. M. Owens and G. F. Sallee, *Proc. IEEE* **159**, 308 (1971).

[216] A. A. Maznev, A. G. Every, and O. B. Wright, *Wave Motion* **50**, 776 (2013).

[217] R. Krishnan, S. Shirota, Y. Tanaka, and N. Nishiguchi, *Solid State Commun.* **144**, 194 (2007).

[218] S. Danworaphong, T. A. Kelf, O. Matsuda, M. Tomoda, Y. Tanaka, N. Nishiguchi, O. B. Wright, Y. Nishijima, K. Ueno, S. Juodkazis, and H. Misawa, *Appl. Phys. Lett.* **99**, 201910 (2011).

[219] S. Alagoz, *Appl. Acoust.* **76** 402 (2014).

[220] H.-X. Sun, S.-Y. Zhang, and X.-J. Shui, *Appl. Phys. Lett.* **100**, 103507 (2012).

[221] H. Jia, M. Ke, C. Li, C. Qiu, and Z. Liu, *Appl. Phys. Lett.* **102**, 153508 (2013).

[222] H.-X. Sun and S.-Y. Zhang, *Appl. Phys. Lett.* **102**, 113511 (2013).

[223] X. Zhu, X. Zou, B. Liang, and J. Cheng, *J. Appl. Phys.* **108**, 124909 (2010).

[224] M. Maldovan, *Nature* **503**, 209 (2013).

[225] R.-Q. Li, B. Liang, Y. Li, W.-W. Kan, X.-Y. Zou, and J.-C. Cheng, *Appl. Phys. Lett.* **101**, 263502 (2012).

[226] J.-J. Chen, X. Han, and G.-Y. Li, *J. Appl. Phys.* **113**, 184506 (2013).

[227] J. Lu, C. Qiu, M. Ke, and Z. Liu arXiv:1411.1851 (2014).

[228] B. Yuan, B. Liang, J.-C. Tao, X.-Y. Zou, and J.-C. Cheng, *Appl. Phys. Lett.* **101**, 043503 (2012).

[229] A. Cicek, O. A. Kaya, and B. Ulug, *Appl. Phys. Lett.* **100**, 111905 (2012).

[230] B. Liang, B. Yuan, and J.-C. Cheng, *Phys. Rev. Lett.* **103**, 104301 (2009).

[231] B. Liang, X.-Y. Zou, B. Yuan, and J.-C. Cheng, *Appl. Phys. Lett.* **96**, 233511 (2010).

[232] B. Liang, X. S. Guo, J. Tu, D. Zhang, and J. C. Cheng, *Nat. Mater.* **9**, 989 (2010).

[233] X. Guo, Z. Lin, J. Tu, B. Liang, J. Cheng, and D. Zhang, *J. Acoust. Soc. Am.* **133**, 2 (2013).

[234] C. Ma, R. G. Parker, B. B. Yellen, *J. Sound Vib.* **332**, 4876 (2013).

[235] A. Merkel, V. Tournat, and V. Gusev, *Phys. Rev. E* **90**, 023206 (2014).

[236] R. Fleury, D. L. Sounas, C. F. Sieck, M. R. Haberman, A. Alù, *Science* **343**, 516 (2014).

[237] M. B. Zanjani, A. R. Davoyan, A. M. Mahmoud, N. Engheta, and J. R. Lukes, *Appl. Phys. Lett.* **104**, 081905 (2014).

[238] B.-I. Popa and S. A. Cummer, *Nat. Commun.* **5**, 3398 (2014).

[239] S. C. Masmanidis, R. B. Karabalin, I. De Vlaminck, G. Borghs, M. R. Freeman, M. L. Roukes, *Science* **317**, 780 (2007).

[240] S. Bringuier, N. Swinteck, J. O. Vasseur, J.-F. Robillard, K. Runge, K. Muralidharan, and P. A. Deymier, *J. Acoust. Soc. Am.* **130**, 4 (2011).

[241] I. Mahboob, E. Flurin, K. Nishiguchi, A. Fujiwara and H. Yamaguchi, *Nat. Commun.* **2**, 198 (2011).

[242] T. Rueckes, K. Kim, E. Joselevich, G. Y. Tseng, C.-L. Cheung, and C. M. Lieber, *Science* **289**, 94 (2000).

[243] A. N. Cleland and M. R. Geller, *Phys. Rev. Lett.* **93**, 070501 (2004).

[244] P. Rabl, S. J. Kolkowitz, F. H. L. Koppens, J. G. E. Harris, P. Zoller and M. D. Lukin, *Nat. Phys.* **6**, 602 (2010).

[245] R. L. Badzey, G. Zolfagharkhani, A. Gaidarzhy, and P. Mohanty, *Appl. Phys. Lett.* **85**, 3587 (2004).

[246] W. J. Venstra, H. J. R. Westra, and H. S. J. van der Zant, *Appl. Phys. Lett.* **97**, 193107 (2010).

[247] N. A. Khovanova and J. Windelen, *Appl. Phys. Lett.* **101**, 024104 (2012).

[248] I. Mahboob and H. Yamaguchi, *Nat. Nanotechnol.* **3**, 275 (2008).

[249] I. Mahboob, M. Mounaix, K. Nishiguchi, A. Fujiwara, and H. Yamaguchi, *Sci. Reports* **4**, 4448 (2014).

[250] P. Mohanty, D. A. Harrington, K. L. Ekinci, Y. T. Yang, M. J. Murphy, and M. L. Roukes, *Phys. Rev. B* **66**, 085416 (2002).

[251] X. Sun, X. Zhang, and H. X. Tang, *Appl. Phys. Lett.* **100**, 173116 (2012).

[252] M. Goryachev, D. L. Creedon, E. N. Ivanov, S. Galliou, R. Bourquin, and M. E. Tobar, *Appl. Phys. Lett.* **100**, 243504 (2012).

[253] S. Chakram, Y. S. Patil, L. Chang, and M. Vengalattore, *Phys. Rev. Lett.* **112**, 127201 (2014).

[254] M. Goryachev, M. E. Tobar and S. Galliou, *IEEE Joint UFFC, EFTF and PFM Symposium* (2013).

[255] W. I. Dobrov, *Phys. Rev.* **134**, A734 (1964).

[256] S. R. Sklan and J. C. Grossman, *New J. Phys.* **16**, 053029 (2014).

[257] L. Wang and B. Li, *Phys. Rev. Lett.* **99**, 177208 (2007).

[258] B. Li, L. Wang, and G. Casati, *Phys. Rev. Lett.* **93**, 184301 (2004).

[259] B. Li, L. Wang, and G. Casati, *Appl. Phys. Lett.* **88** 143501 (2006).

[260] W. C. Lo, L. Wang, and B. Li, *J. Phys. Soc. Japan* **77**, 054402 (2008).

[261] L. Wang and B. Li, *Phys. Rev. Lett.* **101**, 267203 (2008).

[262] C. Chang, D. Okawa, A. Majumdar, and A. Zettl, *Science* **314**, 1121 (2006).

[263] R.-G. Xie, C-T. Bui, B. Varghese, M.-G. Xia, Q.-X. Zhang, C.-H. Sow, B. Li, and J. T. L. Thong, *Adv. Funct. Mater.* **21**, 1602 (2011).

[264] M. Terraneo, M. Peyrard, and G. Casati, *Phys. Rev. Lett.* **88**, 094302 (2002).

[265] L. J. Aplet and J. W. Carson, *Appl. Optics* **3**, 4 (1964).

[266] R. Guermeur, J. Joffrin, A. Levelut, and J. Penne, *Solid State Commun.* **5**, 369 (1967).

[267] V. I. Nekorkin *Introduction to Nonlinear Oscillations* (Wiley-VCH Verlag GmbH & Co., Wenheim, Germany, 2015).

[268] R. F. Wallis and A. A. Maradudin, *Phys. Rev. B* **3**, 2063 (1971).

[269] T. P. Martin and L. Genzel, *Phys. Status Solide B* **61**, 493 (1974).

[270] M. Först, C. Manzoni, S. Kaiser, Y. Tomioka, Y. Tokura, R. Merlin, and A. Cavalleri, *Nat. Phys.* **7**, 854 (2011).

[271] A. Subedi, A. Cavalleri, and A. Georges, *Phys. Rev. B* **89**, 220301(R) (2014).

[272] E. G. Gamalyn and A. V. Rode, *Prog. Quant. Electron.* **37**, 215 (2013).

[273] K. Yonemitsu and K. Nasu, *Phys. Rep.* **465**,1 (2008).

[274] H. Ichikawa, S. Nozawa, T. Sato, A. Tomita, K. Ichiyanagi, M. Chollet, L. Guerin, N. Dean, A Cavalleri, S.-I. Adachi, T.-H. Arima, H. Sawa, Y. Ogimoto, M. Nakamura, R. Tamaki, K Miyano, and S.-Y. Koshihara, *Nature. Mater.* **10**, 101 (2011).

[275] S. Wall, D. Wegkamp, L. Foglia, K. Appavoo, J. Nag, R. F. Haglund Jr, J. Stähler, and M. Wolf, *Nat. Commun.* **3**, 721 (2012).

[276] S. Wall, L. Foglia, D. Wegkamp, K. Appavoo, J. Nag, R. F. Haglund, Jr., J. Stähler, and M. Wolf, *Phys. Rev. B* **87**, 115126 (2013).

[277] T. Garl, E. G. Gamaly, D. Boschetto, A. V. Rode, B. Luther-Davies, and A. Rousse, *Phys. Rev. B* **78**, 134302 (2008).

[278] C. Kittel, *Introduction to Solid State Physics (8th ed.)* (Wiley, New York, 2004).

[279] J. Gump, I. Finkler, H. Xia, R. Sooryakumar, W. J. Bresser and P. Boolchand, *Phys. Rev. Lett.* **92**, 245501 (2004).

[280] M. Petr, M. E. Helgeson, J. Soulages, G. H. McKinley, and P. T. Hammond, *Polymer. Comm.* **54**, 12 (2013)

[281] E. Verploegen, J. Soulages, M. Kozberg, T. Zhang, G. H. McKinley, and P. T. Hammond, *Angew. Chemie.* **48**, 19 (2009).

[282] M. Aspelmeyer, T. J. Kippenberg, and F. Marquardt, *Rev. Mod. Phys.* **86**, 1391 (2014).

[283] C. K. Law, *Phys. Rev. A* **51**, 2537 (1995).

[284] V. Braginsky and A. Manukin, *Sov. Phys. JETP (USSR)* **25**, 653 (1967).

[285] M. Vogel, C. Mooser, K. Karrai, and R. J. Warburton, *Appl. Phys. Lett.* **83**, 1337 (2003).

[286] C. Höhberger-Metzger and K. Karrai, *Nature* **432**, 1002 (2004).

[287] O. Arcizet, P. F. Cohadon, T. Briant, M. Pinard, and A. Heidmann, *Nature* **444**, 71 (2006).

[288] T. Corbitt, Y. Chen, E. Innerhofer, H. Müller-Ebhardt, D. Ottaway, H. Rehbein, D. Sigg, S. Whitcomb, C. Wipf, and N. Mavalvala, *Phys. Rev. Lett.* **98**, 150802 (2007).

[289] N. D. Lanzillotti-Kimura, A. Fainstein, A. Lemaitre, B. Jusserand, and B. Perrin, *Phys. Rev. B* **84**, 115453 (2011).

[290] M. Pinard, A. Dantan, D. Vitali, O. Arcizet, T. Briant, and A. Heidmann, *Europhys. Lett.* **72**, 747 (2005).

[291] M. J. Hartmann and M. B. Plenio, *Phys. Rev. Lett.* **101**, 200503 (2008).

[292] H. Müller-Ebhardt, H. Rehbein, R. Schnabel, K. Danzmann, and Y. Chen, *Phys. Rev. Lett.* **100**, 013601 (2008).

[293] Z. M. Zhu, D. J. Gauthier, and R.W. Boyd, *Science* **318**, 1748 (2007).

[294] A. H. Safavi-Naeini and O. Painter, *New J. Phys.* **13**, 013017 (2011).

[295] D. E. Chang, A. H. Safavi-Naeini, M. Hafezi, and O. Painter, *New J. Phys.* **13**, 023003 (2011).

[296] V. Fiore, Y. Yang, M. C. Kuzyk, R. Barbour, L. Tian, and H. Wang, *Phys. Rev. Lett.* **107**, 133601 (2011).

[297] E. Verhagen, S. Deleglise, S. Weiss, A. Schliesser, and T. J. Kippenberg, *Nature* **482**, 63 (2012).

[298] T. A. Palomaki, J. W. Harlow, J. D. Teufel, R. W. Simmonds, and K. W. Lehnert, *Nature* **495**, 210 (2013).

[299] S. A. McGee, D. Meiser, C. A. Regal, K.W. Lehnert, and M. J. Holland, *Phys. Rev. A* **87**, 053818 (2013).

[300] J. T. Hill, A. H. Safavi-Naeini, J. Chan, and O. Painter, *Nat. Commun.* **3**, 1196 (2012).

[301] Y.-D. Wang and A. A. Clerk, *Phys. Rev. Lett.* **108**, 153603 (2012).

[302] C. Galland, N. Sangouard, N. Piro, N. Gisin, and T. J. Kippenberg, *Phys. Rev. Lett.* **112**, 143602 (2014).

[303] K. Stannigel, P. Komar, S. J. M. Habraken, S. D. Bennett, M. D. Lukin, P. Zoller, and P. Rabl, *Phys. Rev. Lett.* **109**, 013603 (2012).

[304] M. Schmidt, M. Ludwig, and F. Marquardt, *New J. Phys.* **14**, 125005 (2012).

[305] S. Rips and M. J. Hartmann, *Phys. Rev. Lett.* **110**, 120503 (2013).

[306] S. R. Sklan and J. C. Grossman, *Phys. Rev. B* **92**, 165107 (2015).

[307] D. T. Gillespie, *J. Phys. Chem.* **81**, 25 (1977).

[308] C. A. D. Roeser, M. Kandyla, A. Mendioroz, and E. Mazur, *Phys. Rev. B* **70**, 212302 (2004).

[309] O. Synnergrena, T. N. Hansen, S. Canton, H. Enquist, P. Sondhauss, A. Srivastava, and J. Larsson, *App. Phys. Lett.* **90**, 171929 (2007).

[310] P. F. Cohadon, A. Heidmann, and M. Pinard, *Phys. Rev. Lett.* **83**, 3174 (1999).

[311] C. Höhberger-Metzger and K. Karrai, *Nature* **432**, 1002 (2004).

[312] C. V. Raman, *Indian J. Phys.* **2**, 387 (1928).

[313] R. Loudon, *The Quantum Theory of Light, (3rd ed.)* (Oxford University Press, New York, 2001).

[314] P. W. Atkins, J. de Paula, *Physical Chemistry (8th ed.)* (Oxford University Press, New York, 2006).

[315] L. Brillouin, *Ann. Phys-Paris* **17**, 88 (1922).

[316] P. Debye, F.W. Sears, *PNAS* **18**, 6 (1932).

[317] R. Lucas, P. Biquard, *J. Phys-Paris* **71**, 464 (1932).

[318] N. Swinteck, P. Lucas, and P. A. Deymier, *AIP Advances* **4**, 124603 (2014).

[319] F. J. Dyson, *Phys. Rev.* **92**, 6 (1953).

[320] R. Ganesh and S. Gonella, *Wave Motion* **50**, 4 (2013).